Peter Franzen

Weiterführung der Entwicklung der HF-getriebenen Ionenquelle (Ergebnisse 2010)
Abschlussbericht des Vertrages F4E-2008-GRT-07 (RFSDE)

Continuation of the Development for the RF ion source (Results 2010)
Final Report of Contract F4E-2008-GRT-07 (RFSDE)

1

F4E-2008-GRT-07 (RFSDE)

Final Report

Continuation of the Development
for the RF ion source
(Results 2010)

P. Franzen

with contributions of

Werner Kraus, Dirk Wünderlich, Loic Schiesko, Ursel Fantz,
Wolfgang Böhm, Christian Wimmer

IPP Garching, Technology Department
Neutral Beam Group

Contents:

1   Executive Summary

1.1   BATMAN

The experiments at BATMAN concentrated on the optimization of the magnetic filter field both in hydrogen and deuterium operation in order to identify the main parameters for optimum performance and on the influence of the source body temperature on the performance of the source. The latter is important as an operation at 35 °C would minimize the number of heating circuits at HV potential for the HNB. Furthermore, experiments with different magnetic field configurations in the driver have been carried out with the goal of low pressure operation and increased RF efficiency, accompanied by basic experiments regarding helicon discharges at the University of Augsburg.

For ion extraction and plasma symmetry, the magnetic field strength in front of the plasma grid is the important parameter; a field of some mT in front of the plasma grid for sufficient negative ion extraction is needed. The maximum ion current density in hydrogen was achieved with a field of 2-3 mT. The plasma symmetry in front of the plasma grid, however, improves with decreasing field. These experiments have been done in close collaboration with IPR India with joint experiments in December 2009. In contrast, the amount of co-extracted electrons is determined by the integral BdL, the minimum co-extracted electron/ion ratio was achieved for about 1250 Gcm. Unfortunately, the present setup does not allow fulfilling both requirements for ion extraction and electron suppression simultaneously up to now. All results are independent on the direction of the filter field, i.e. the plasma drift direction.

Shifting the field at the driver exit was not only worse for the source performance, but a sustainment of the plasma after the gas puff for a pressure below 0.5 Pa was not possible. This issue is still open, as the reason for that behavior is not clear up to now.

Experiments in deuterium have been started only at the end of the present contract due to technical problems with (water and air) leaks in fall 2010; first results show similar trends as in hydrogen: some field at the plasma grid is required for sufficient ion extraction; the required integral BdL for sufficient electron suppression, however, is much larger than in hydrogen. Nevertheless, the ITER requirements could be fulfilled.

Reducing the source body temperature to 35 °C also during conditioning had no influence of the source performance and the speed of conditioning. This is much more influenced by the impurity level of the source.

Experiments in hydrogen and argon as well as in mixtures of both gases have been carried out at the University of Augsburg at a new flexible experiment designed for basic investigations of the possibility to use a Helicon discharge in the NBI driver.

In argon, indications of a Helicon discharge have been found. Ionization is high (few percents) and a considerable jump in electron density occurs by raising the input power.

When hydrogen is added into the argon plasma, the input power needed to induce the jump in electron density strongly increases with the relative hydrogen density. For more than 20 % hydrogen (or deute-

rium) in argon more then 600 W would be needed and it was not possible to induce the jump using the existing power supply. In mixtures of hydrogen and argon the jump in the electron density is accompanied with a significant decrease in the dissociation of the H_2 molecule as well as the gas temperature.

In hydrogen, ionization is much lower than in argon and no jumps have been observed so far. Nevertheless, by adding a magnetic field, an increase in dissociation as well as a more stable low pressure operation has been demonstrated.

1.2   MANITU

MANITU went into operation again in October 2009 with some modifications: The MANITU source was upgraded for long pulse, high power, experiments by SF_6 insulation of the RF coil. The extraction area was reduced by about 30% by covering most of the apertures that are not within the driver projection. The polarity of the magnetic filter field was reversed; as previous experiments indicated, the negative ions are mainly produced at the part of the plasma grid that is opposite to the plasma drift direction. Now the plasma drifts to the lower part of the plasma grid, so that the negative hydrogen ions are produced at the upper part of the grid. As the Cs oven is placed although at the upper part of the MANITU source, it was expected that the negative ion current density increases due to the larger flux of Cs onto that part of the plasma grid. However, the experiments so far do not yet give a clear answer, whether this is the case. Furthermore, long pulses at low pressure (down to 0.2 Pa) are now possible by the installation of a flow controller.

The experiments in the past indicated strongly that copper deteriorates the work function of the Cs layer at the plasma grid by forming cesium-copper compounds together with the background oxygen. Hence, sputtering probes were introduced in the MANITU source in order to identify the copper sources. Apart from the Faraday screen — here copper is released via sputtering by plasma particles —, the other copper source is the sputtering of copper by back streaming ions from the rear part of the source. By increasing more and more the Mo covered source areas, starting from the Faraday screen in 2008, then the back plate, bias plate and plasma grid in 2008, and ending now with the driver exit, the copper impurity in the ion source could be reduced almost to zero. Measurements of the sputtering yield of inserts indicated that the amount of back streaming ions is of the order of a few percent of the extracted current density; this is in some agreement with simple models.

Although long pulses (several 100 seconds) with 80 kW power are now possible, the ITER requirements have not been met yet. The reason is still the increasing electron current — or, to be more precise, the current on the extraction grid, which consists also of negative ions due to the poor beam optics of the MANITU grid system — during is a long pulse. Hence, RF power and extraction voltage are limited in order to avoid damage of the extraction grid. This limitation is even more pronounced in deuterium operation due to the much larger ratio of co-extracted electrons. Nevertheless, stable deuterium pulses of some hundreds of seconds with an extracted ion current density of 10 - 15 mA/cm^2 and a co-extracted electron fraction of less than one have been achieved.

The increase of the electron current during a long pulse seems to be associated with the Cs dynamics in the source, which is not yet fully understood. An increase of the Cs influx during the pulse does not influ-

ence the source performance; there are also indications of a long term degradation of the quality of the Cs layer on the plasma grid.

In contrast to previously obtained results (see the intermediate report), more detailed experiments show now that the homogeneity of the beam — expressed by the beam divergence profile measured by Doppler-shift spectroscopy — does not seem to correlate with the homogeneity of the plasma in front of the plasma grid. Furthermore, the Doppler spectroscopy measurements indicate a much lower stripping fraction than expected from standard gas flow calculations.

The experiments in second half of the contract concentrated on investigations of the effect of the plasma density on the extracted currents by covering the bottom grid halve. Furthermore, the direction of the plasma drift was converted by changing the polarity of the magnets. The extracted currents of negative hydrogen ions as well as of the electrons, however, depend only weakly on the direction of the drift, i.e. on the plasma densities. The assumption that one grid halve would deliver a higher negative hydrogen current could not be confirmed by these experiments up to now. The results indicate that the source performance is determined to a greater degree by the plasma sheath close to the plasma grid which is not (yet?) accessible by diagnostics.

1.3   RADI

After a long period of rebuilding the experimental hall for ELISE, RADI went back into operation mid of March 2010. As the reason for the damage of the Faraday screens is still not identified, the setup of RADI was changed to 1 driver / 1 generator operation for a further assessment of the damages. A clear reason, however, was not found.

After some improvement of the RF system, plasma ignition is now possible also at good matching and high power. Stable operation was obtained.

Some important tests of ELISE/SPIDER design choices have been performed: apart from tests of the ELISE RF circuit, it was demonstrated that driver operation at low pressure (down to 0.2 Pa) is possible with the PG current return conductors running near the drivers.

1.4   Diagnostics

A simple diode laser absorption setup which can be easily attached to the ion sources by fiber optics has been built. It showed a better detection limit for cesium than the white light absorption. Both have been tested at a small lab experiment at the University of Augsburg.

Since the absorption spectrum can be integrated automatically, direct monitoring of the Cs-signal is possible. Calibration of the system was done with a cesium reference cell, in which the vapor pressure can be adjusted exactly by temperature variation of a cold spot. The system was adapted successfully to the BATMAN ion source, where the cesium density can be measured during both vacuum and plasma phase for the first time. The system is now working routinely and led to a better understanding of the evaporation and redistribution of cesium in the ion source.

Due to the problems with the Faraday screen operation, the Laser Detachment at RADI measurements could not be started up to now.

Basic investigations related to the development of a cesium monitor were performed. Such a cesium monitor can be used to optimize the source performance by adjusting the cesium flux delivered by the oven. It was shown that increasing the cesium signal measured by optical emission spectroscopy in a well conditioned source during a pulse – either intentionally by rising the temperature of the cesium oven or by heating up of source components – influences not significantly the extracted currents. Adjusting the cesium signal over a period of several pulses, on the other hand, changes the temporal dynamics of the extracted ion current during a pulse as well as the absolute value of the co-extracted electron current. Now, further measurements are planned to investigate the dependence of the currents on the cesium level during the cesium conditioning. Additionally, it will be investigated if and how the optimum possible performance is connected to this intermediate phase between cesium free and cesiated source.

1.5   Modeling

A new beam transport code BBC-NI was started to be developed and benchmarked against other codes. The final goal of this code is to calculate stripping, Doppler H_α emission and calorimetric profiles for realistic aperture geometries and electrical and magnetic fields. A first application was the calculation of the beam deflection at BATMAN with the different filter field configurations.

The Particle-in-cell code Bacon was applied to investigate the transport of electrons through the magnetic field and the cooling of the electrons correlated to this transport. For the plasma parameters of the IPP ion sources and a small computational domain the electron cooling can be reproduced by the code. For enabling further investigations on the underlying mechanisms, a flexible Monte Carlo collision module was developed and implemented to the code. Using the new Monte Carlo module it was possible to show that the collision processes being most relevant for the transport of electrons across the magnetic filter field are inelastic collisions. Calculations have been performed for magnetic fields with different shapes but identical field integral, resulting in comparable electron density close to the plasma grid surface. This result indicates that the functionality of the filter is determined mainly by the integral of the magnetic field strength.

The Monte Carlo code TrajAn calculates the extraction probability of negative ions as well as the extracted negative ion current profile over the extraction apertures. The latter can be used to investigate the correlation of the homogeneity of the ion production on the plasma grid to the negative ion beam homogeneity. The applicability of TrajAn for such problems is demonstrated by applying a simple surface model, based on the assumption that the negative hydrogen production is proportional to the cesium flux onto the surface: the extracted ion density over the complete extraction area was calculated for homogeneous production of the negative ions and a production profile based on the cesium flux calculated by the CsFlow3D code. For short pulses of the ion source the current profile in the latter case is clearly more inhomogeneous. This inhomogeneity is even stronger for long pulses since additional sources for cesium are created by heating of the bias plate. This result demonstrates that an actively cooled bias plate – as planned for ELISE – is indis-

pensable for a stable long pulse operation. As a next step it is necessary to improve the used simple surface model to enable a more realistic coupling of the codes.

Using the Monte Carlo cesium transport code CsFlow3D it can be shown that the cesium flux onto the plasma grid surface delivered by the oven attached to the top of the back plate is strongly inhomogeneous. Additionally, it is shown that the flux homogeneity could be improved significantly by an array of cesium dispensers mounted close to the plasma grid surface. Although such a solution may be difficult to realize due to technical restrictions, the present calculations demonstrate the principal capability of CsFlow3D to support the investigation of alternative cesium sources of oven positions. This capability is of particular interest in combination of the possible coupling of TrajAn to CsFlow3D.

Analysis of emissivities measured by optical emission spectroscopy heavily depends on the availability of appropriate population models. For the plasma of the IPP negative ion source test facilities, collisional radiative models for atomic and molecular hydrogen based on the solver Yacora are applied. Parts of the cold plasma close to the plasma grid surface may be recombining (or in between purely recombining and ionizing plasmas). Since the input (cross sections and rate coefficients) for recombining plasmas used by Yacora was based on relatively old literature (or taken from other collisonal radiative models), the used data for radiative recombination of H^+ and dissociative recombination of H_2^+ was critically checked against the most recent data available. A very good agreement was found. Recent results from optical emission spectroscopy indicate that the transition between ionizing and recombining plasmas also affect the ratios of cesium line emission. It was shown that introducing the mutual neutralization of Cs^+ and H^- into a simple Corona model for the cesium radiation yields much more realistic cesium densities than the original Corona model itself. For a complete treatment of the problem the development of a collisional radiative model for cesium is mandatory.

2   Schedule (WBS 1.0)

The detailed schedule of the experimental campaigns during the contract is shown in Appendix 9.1.

The schedule of the experimental campaigns was changed due to

- unforeseen difficulties in test bed operation during the course of the experiments:
  - o   Faraday screen operation at RADI
  - o   broken 10 kV/400 V transformer at BATMAN
  - o   several air leaks at BATMAN
  - o   water leak in the extraction grid at BATMAN
  - o   water leak in the back plate of MANITU
  - o   problems with the HV control at MANITU

- work on IPP infrastructure necessary for the test bed operation, which was known at the start of the contract, but delayed both in the starting date as also in the duration:
  - o   rebuild of the BATMAN HV module for ELISE
  - o   rebuild of the main water supply of the L6 building, also housing MANITU

The status of the experimental campaigns (see Appendix 9.1) is as following:

Test Facility	Experimental Campaign	Title	Status
BATMAN	1	Magnetic Field Studies in H	finished
	2	Magnetic Field Studies in H & D	finished, no measurements in D
	3	RF Operation only, Driver Extension	delayed due to broken 10kV/400 V transformer and due to delays of the rebuild of the HV module
	4	Magnetic Field Studies in H & D	starts 04/07/2010, hampered by technical problems with air and water leaks
	5	Influence of Source Temperature on Performance, Continuation of Magnetic Field Studies in D	Source temperature experiments finished, deuterium operation started
	6	RF Measurements	in collaboration with RFX, postponed to January 2011
MANITU	1	Long Pulse Operation in H	finished
	2	Long Pulse Operation in H & D	finished

Test Facility	Experimental Campaign	Title	Status
	3	Cryo Pump Measurements	finished, in collaboration with KIT
	4	Long Pulse Operation in H & D	started with different setup (masking of the lower grid halve, new flexible magnet frame), hampered by technical problems (HV control, water leaks in extraction grid and back plate), not finished yet
	5	Long Pulse Operation in H & D	not finished
RADI	Re-Commissioning		successful
	1	Faraday Shield Operation	still ongoing together with matching optimization and tests of ELISE and SPIDER components
	2	Homogeneity w/o Cs	finished
	3	Homogeneity with Cs	not finished
	4	RF Measurements	postponed to January 2011, in collaboration with RFX Padua

3   Experiments at BATMAN (WBS 2.1)

The experiments at BATMAN regarded the improvement of the RF ion source. Three topics have been addressed: (1) the optimization of the magnetic filter field both in hydrogen and deuterium (section 3.1), and (2) the improvement of the driver RF efficiency by exploring the possibility of using Helicon-like drivers (section 3.2). Both experiments have been supported (procurement of hardware) also by an ITER R&D contract[1]. Furthermore, (3) experiments regarding the influence of the source body temperature on the performance have been performed (section 3.3).

The experiments in the second halve of the contract were severely hampered by technical problems with a large water leak in the extraction grid and several large and small air leaks in the BATMAN test facility. These problems last from September to end of November 2011.

3.1   Magnetic Filter Field Studies at BATMAN

3.1.1   Background

The magnetic filter field in the RF driven negative ion source is by far not optimized. The present results have been obtained in small sources with fields created by permanent magnets. How these results can be transferred to the large ITER sources where the field is created by a current through the plasma grid with a different 3D field map is still an open issue.

The magnetic filter field influences the beam properties downstream in the accelerator. Calculations from M. Singh and B. de Esch showed for the DNB, that the beam quality requirements cannot be achieved with the present filter field concepts due to large deflection of the ions in the downstream filter field components [1].

Hence, the filter field must be optimized — not only for the DNB, but also for the HNB — with respect to the beam quality in the accelerator, but also ensuring that the filter field in the source itself is sufficient enough; but up to now, the optimizing parameters for the filter field with respect to negative hydrogen ion yield and electron suppression were not clear.

For that purpose, ELISE is an important step; ELISE will test for the first time an ITER-relevant RF source with extraction, so that the influence of ITER-relevant filter fields on the source performance can be directly addressed. ELISE has also enough flexibility to optimize the present concepts or even to explore new concepts. To the present knowledge, the filter field in the source — together with an adjusted potential distribution — has two functions: (1) to cool down of the electrons, for what the BdL or gradients might be the important parameter; (2) to ensure that the negative ions that are created at the plasma grid surface are bent

---

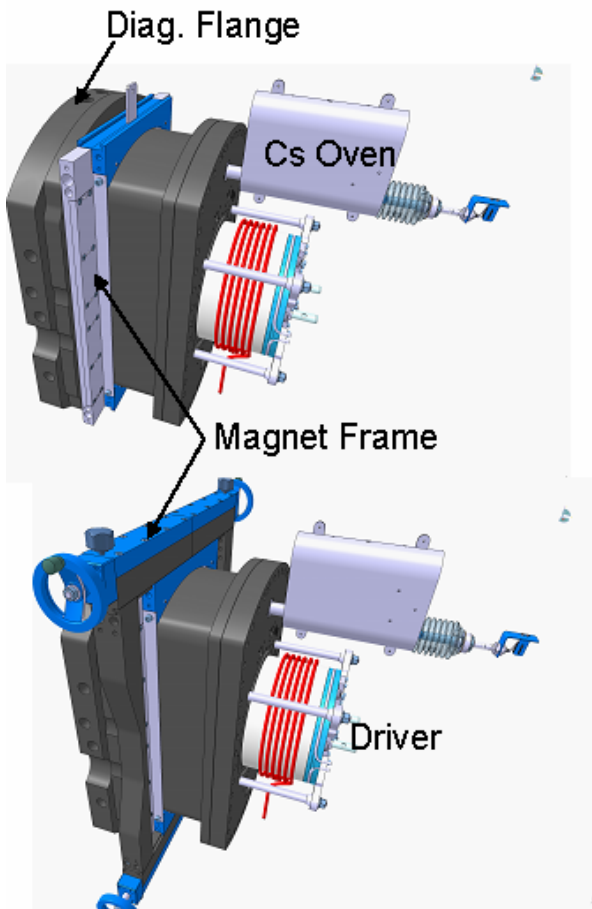[1] Contract number ITER/CT/09/4100000772

Figure 1: Top: Sketch of the IPP prototype source with the magnet frame w/o yoke; Bottom: with yoke in closed position.
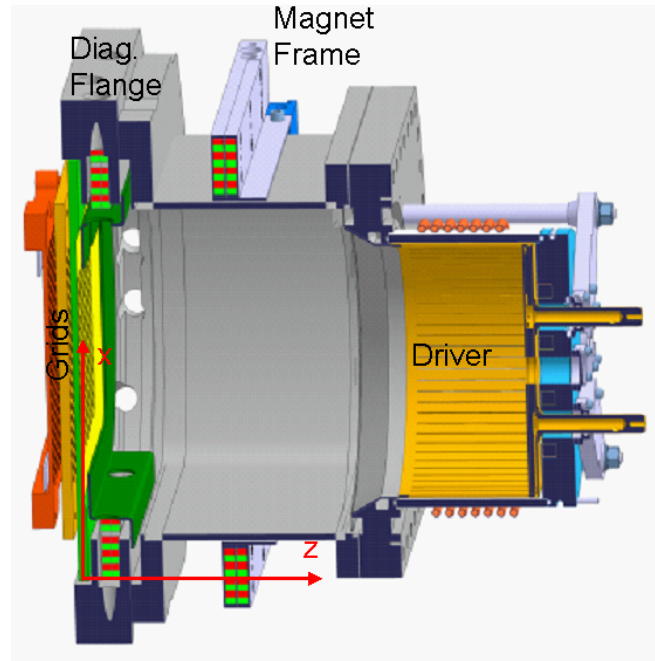
Figure 2: Top view into the ion source with magnets in the diagnostic flange and with the magnet frame.

back to the apertures, and survive on their path length; for that some magnetic field near the plasma grid is necessary.

For a good beam quality in the accelerator, an overall reduction of the field strength in the accelerator is required. This can be obtained by moving the filter field towards the drivers. But this reduces also the filter field strength in front of the plasma grid and reduces so the extraction probability. Another possibility is to screen the field; this can be done in ELISE rather simply e.g. by making the grounded grid itself or the grounded grid holder box out of soft iron. IPP calculations showed that in the latter case the PG field in the accelerator is reduced by ~70% whereas the field in the source is enhanced by ~30%. A similar solution might be possible for the DNB; that has to be checked with IPR India.

Meanwhile, until ELISE goes into operation, some basic experiments have been done at BATMAN. The goals were:

- to enhance the understanding of the interplay of magnetic fields and the source potentials for the source performance;

- to study filter fields that are as near as possible to the ITER fields at the grid apertures. BATMAN can only investigate the effect of the different fields on the source performance. It cannot address experimentally the effects of these fields on the beam quality; this has to be calculated.

Initially, also studies with a field generated by a current through the plasma grid were foreseen; first studies showed that this could be possible with moderate modifications of the extraction system. But due to problems with the schedule (late signature of the contract), this topic was abandoned in the frame of the present contract, as also simulations showed that similar field configurations can be achieved by a combination of external permanent magnets with soft iron yokes.

3.1.2 Experimental Setup

For the experiments, a new flexible magnet frame was built and installed at BATMAN. It is shown in

Figure 3: Magnet frame with the yoke opened. Dimensions are given in mm.

figure 1, figure 2 and figure 3. The design of the frame was to have optimum flexibility for changes of the magnetic filter field. The frame can be moved continuously along the source body from the diagnostic flange — the nearest position to the plasma grid — to the driver exit.

The frame consists mainly of three parts (see figure 3):

- the support structure surrounding the source body, made out of stainless steel;

- the magnet boxes, that can be attached to the support structure at the sides of the source body; the magnet boxes can be filled each with up to 2x4 magnets;

- the yoke structure, made out of soft iron for closing the magnetic field lines, consisting of two bars at the side of the source and 2x2 bars on top and on bottom; the latter can be moved continuously in horizontal direction for a closed or a more open configuration.

The goal of the design of this magnet frame was to have a magnetic field map as close as possible to the magnetic field structure of the standard filter field at BATMAN which was used up to now. It was generated by 2x4 magnets embedded in the diagnostic flange (see figure 2). All the magnets used both for the standard case and for the magnet frame boxes are commercially available CoSm magnets with dimension of 9x13x50 mm^3 with a maximum magnetic strength of 1 T. The magnets are magnetized in the "13 mm" direction.

However, due to the different position of the standard magnet boxes and the magnet frame — the center of the field in the standard case has a distance of 3 cm from the plasma grid, for the frame in the nearest position the distance is 9 cm — the standard filter field could not be matched perfectly. Instead, the magnet configuration of the frame was chosen so, that in one case the maximum field strength was matched
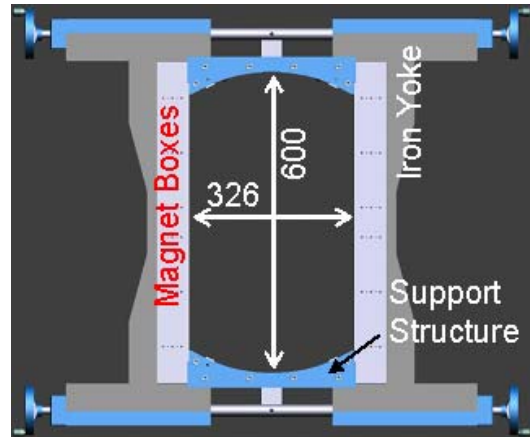
Name	Mag-nets	Used for	$\|B_x\|$ max	Pos. $\|B_x\|$ max	$\int\|B_x\|dz$ Source	$\int\|B_x\|dz$, Driver	$\|B_x\|$ at PG	$\|B_x\|$ at Driver Exit	$\|B_x\|$max Driver
			(mT)	(cm)	(Gcm)	(Gcm)	(mT)	(mT)	(mT)
Standard, z=3	2x4 R	H, D	7.4	3.0	846	189	7.0	0.8	1.1
BMAX, z=9	2x4 R	H, D	7.8	9.0	1298	148	4.1	0.9	1.2
BMAX, z=14	2x4 R	H, D	7.8	14.0	1331	182	1.4	3.4	2.8
BMAX, z=19	2x4 R	H, D	7.8	19.0	1107	371	0.2	6.4	5.9
BDL, z=9	2x3 R	H	5.4	9.0	919	102	3.0	0.8	0.9
BDL, z=14	2x3 R	H	5.4	14.0	943	132	1.1	2.5	2.1
BDL, z=19	2x3 R	H	5.4	19.0	782	275	0.1	4.6	4.2
BDL, z=9, Yoke closed	2x3 R	H, D	12.5	9.0	2479	436	9.5	5.1	4.6
BDL, z=9, Yoke 28 cm opened	2x3 R	D	10.4	8.0	1996	234	7.4	3.6	3.2
BDL, z=9, side bars only	2x3 R	D	8.8	8.0	1696	199	6.3	3.0	2.7

Table 1: Parameters of the different magnetic field configurations used in the hydrogen and deuterium experiments along the center axis of the ion source. The field parameters for the "BDL, z=9, side bars only" case were estimated from magnetic field measurements.

(the "BMAX" configuration) — although in a different distance from the plasma grid —, in the other case the integral *Bdz* was matched (the "BdL" configuration)[2].

Table 1 shows the various parameters for the magnet frame configurations that have been used in the hydrogen and deuterium experiments so far, in comparison with the standard configuration. The maximum magnetic field for the standard case is despite of the closer distance similar to the 2x4 case due to missing magnets for the ports for OES. The respective 2D field maps have been calculated by using the 2d code QuickField [2] and are shown (for the hydrogen cases only) in the Appendix.

The absolute value of the magnetic field strength in the center of the ion source as a function of the distance from the plasma grid is shown in figure 4 for the magnetic configurations used for the experiments. Almost all fields used for hydrogen show a field free region in the source or in the driver; this region is moved deep into the driver, when moving the filter field towards the driver exit.

Up to now, two different numbers of magnets (2x4, 2x3) at three different positions (z=9, i.e. close to the plasma grid, z=14, i.e. source center, and z=19, i.e. close to the driver) have been used. Additionally, the

---

[2] The axial integral — from the plasma grid to the driver plate of the source, i.e. the exit of the driver — of the horizontal magnetic field component in the center of the plasma source is denoted here by *Bdz*, if the value is given, but also by „BdL" as the latter is the common nomenclature in the NBI community.
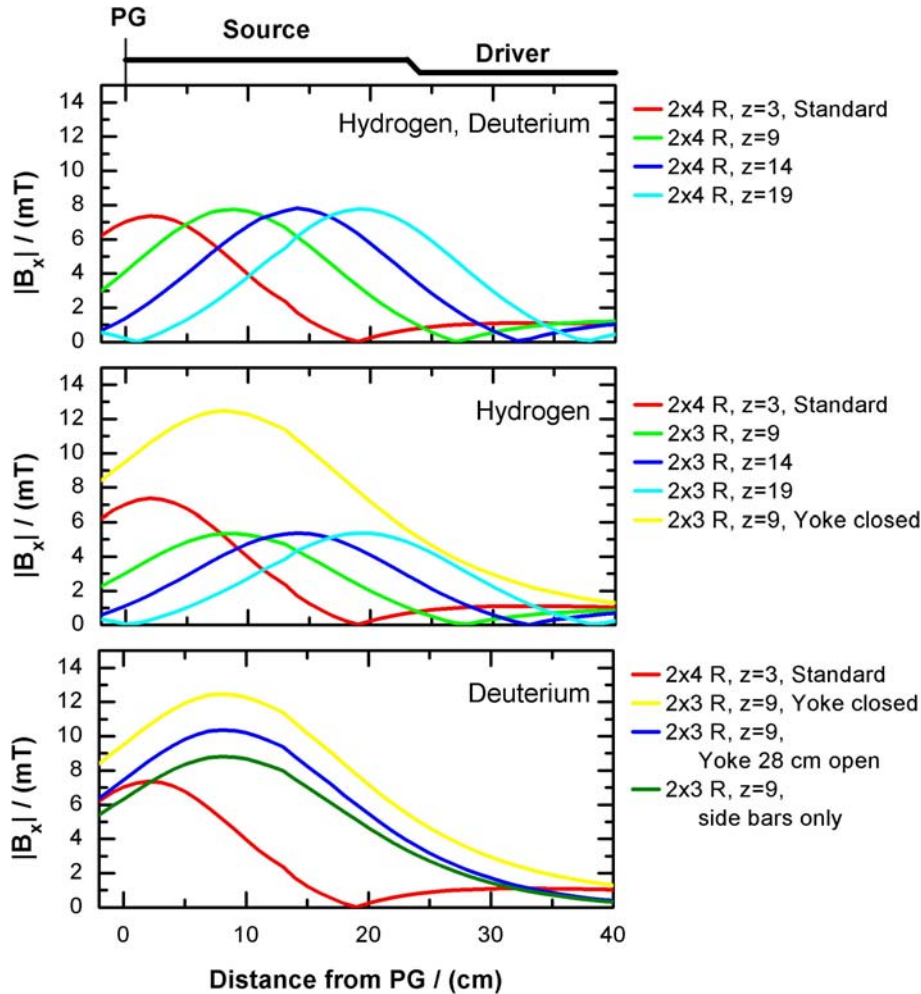
Figure 4: Horizontal ("x") magnetic field strength in the center of the ion source in dependence of the distance from the plasma grid ("z" direction) for the configurations used in the hydrogen and deuterium experiments. The source depth is 23 cm

magnet boxes have been exchanged so that the horizontal field direction changed by 180º in order to change the drift of the plasma and hence the top/down asymmetry. This might be important as the IPP prototype source has an intrinsic asymmetry due to the position of the Cs oven (top of the source, see figure 1). Also some few experiments have been performed in hydrogen without any field and with the yoke closed in the "BdL, z=9" configuration.

Due to the much larger amount of co-extracted electrons in deuterium operation, larger filter fields than for hydrogen are needed for sufficient electron suppression. Up to now, experiments with the 2x3 magnets including the yoke have been performed, including a case with just the side bars attached to the magnet frame. Furthermore, all deuterium experiments have been performed with a magnet polarity so that the plasma drift is downwards.

With the present setup, the various parameters of the magnetic field configuration are not completely independent from each other. This is shown in figure 5 for the hydrogen cases, where the correlation of the magnetic field at the driver exit and the integral *Bdz* value with the magnetic field at the plasma grid is

shown. These parameters are chosen as the performance of the source is correlated with them (see below). However, it can be seen, that the magnetic field at the plasma grid can be varied in a wide range without changing much the integral *Bdz* and that there is only some correlation of the field at the driver exit with the field at the plasma grid for low fields.

In contrast, the correlation of the various field parameters for the magnetic field configurations used for the deuterium experiments so far is much more pronounced. This is shown as an example in figure 6: the integral *Bdz* value depends almost linear on the magnetic filter field strength at the plasma grid. Hence, a clear separation of the effects of the various parameters is not possible up to now.

All the results shown in this report have been performed with the LAG extraction system — with an aperture diameter of 8 mm and an extraction area of 63.6 cm^2. Deuterium operation has been started at the end of the contract only due to the technical problems mentioned above. Due to the limited available time and principal problems with the large co-extracted electron current, systematic measurements regarding the influence of the magnetic field parameters could not be performed up to now.

3.1.3   Results in Hydrogen

3.1.3.1   *Source Performance*

Figure 7 shows the comparison of the overall performance of the ion source with respect to the maximum achieved extracted current density and the minimum amount of co-extracted electrons. Also the comparison with the record values for hydrogen obtained in 2005 is shown. This comparison, however, suffers from problems with the measurement of the RF power at BATMAN in 2005; after installing a new RF power measurement system (from Himmelwerk) in 2007 it turned out that the power levels measured before should be reduced by typically 30%. This was done in this report for the RF power values for the standard field, but there is still an uncertainty as the reduction factor is not fixed but varies in a certain range depending on the matching and other parameters.

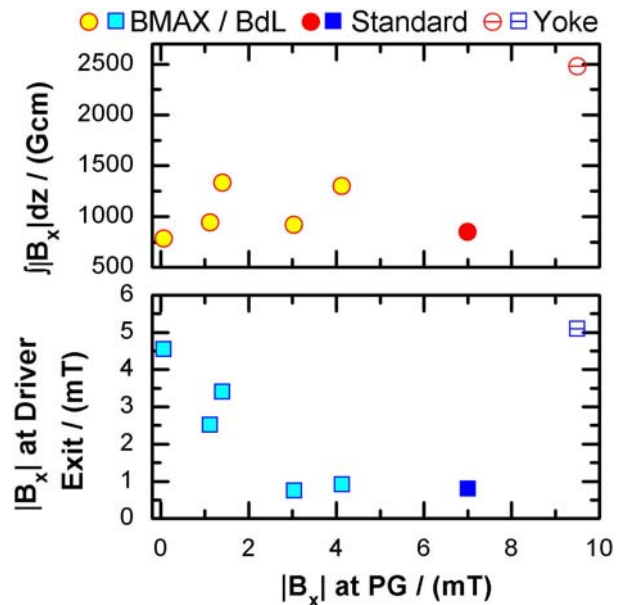*Figure 5: Correlation of the magnetic field strength at the exit of the driver and the integral Bdz value on the magnetic field strength at the plasma grid for the used magnetic field configurations for the hydrogen experiments (see table 1).*
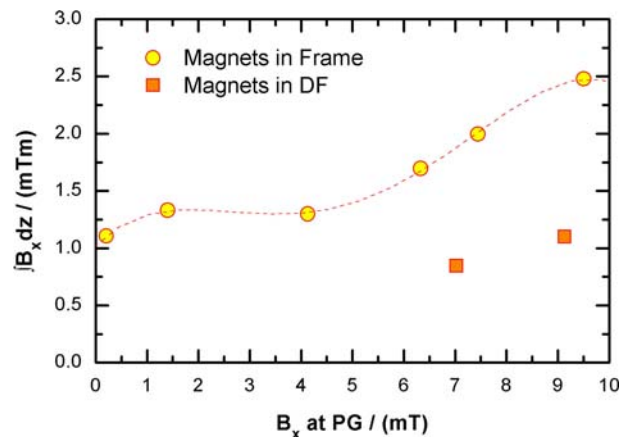

Figure 6: Correlation of the integral Bdz value on the magnetic field strength at the plasma grid for the used magnetic field configurations for the deuterium experiments (see table 1).
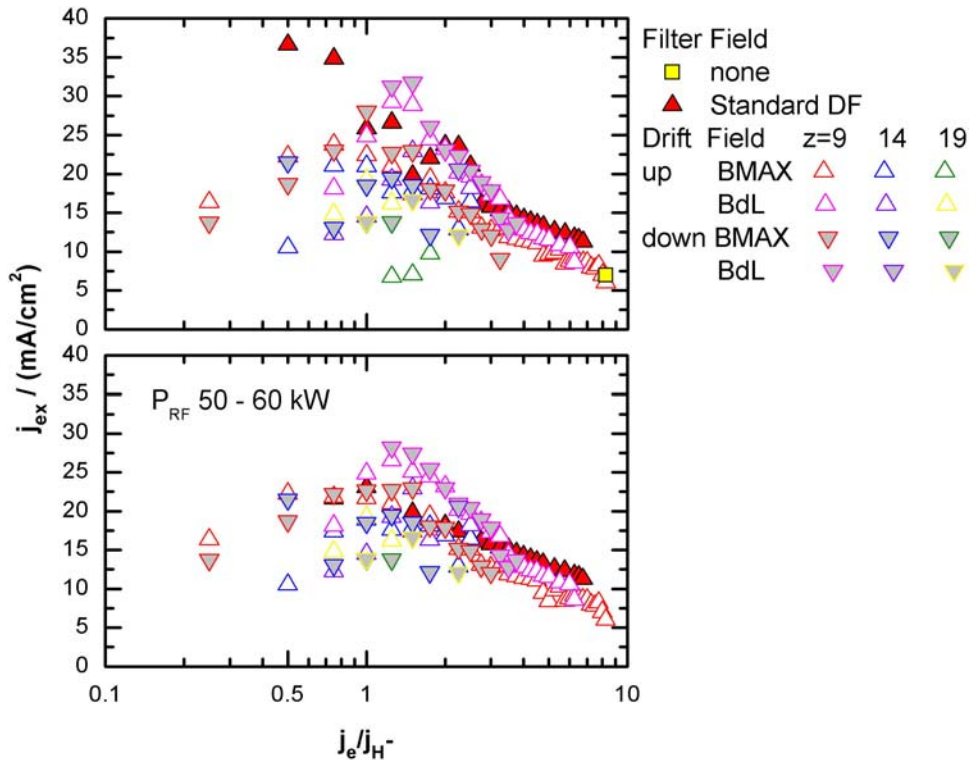
Figure 7: Performance of the IPP prototype source in dependence of the magnetic field configuration. Shown are the maximum achieved values of the extracted current density for intervals of 0.25 of the ratio of the co-extracted electron current to the negative ion current (the number refers to the upper bound). Top: complete data set; bottom: RF power between 50 and 60 kW.

Nevertheless, the data in figure 7 show that:

- the maximum current density is achieved with the "BdL" field configuration, although the electron ion ratio is still just above 1;

- there is not much difference in the source performance between the standard case and the "BMAX, z=9" configuration near the plasma grid, if same parameters, i.e. RF power, are compared;

- the performance does not depend much on the drift direction;

- the performance decreases when the field is shifted towards the driver.

The overall performance in the case of the standard field configuration, however, could not be achieved with the magnet frame configurations. Especially, the current density decreases with decreasing electron/ion ratio for values less than 1. Also there might be a principle restriction in source performance; this behavior might also be a consequence of the course of the experiments: The source was not 'forced' to optimum performance, i.e. increasing RF power, lengthy Cs conditioning, etc., for each of the magnetic configuration.

Most of the data have been achieved at a source filling pressure below 0.4 Pa. In this pressure range, however, it was difficult to sustain the plasma in the driver, when the filter field position was near the driver exit. In most cases, the plasma went out after the gas puff, when the pressure in the driver got too low. A
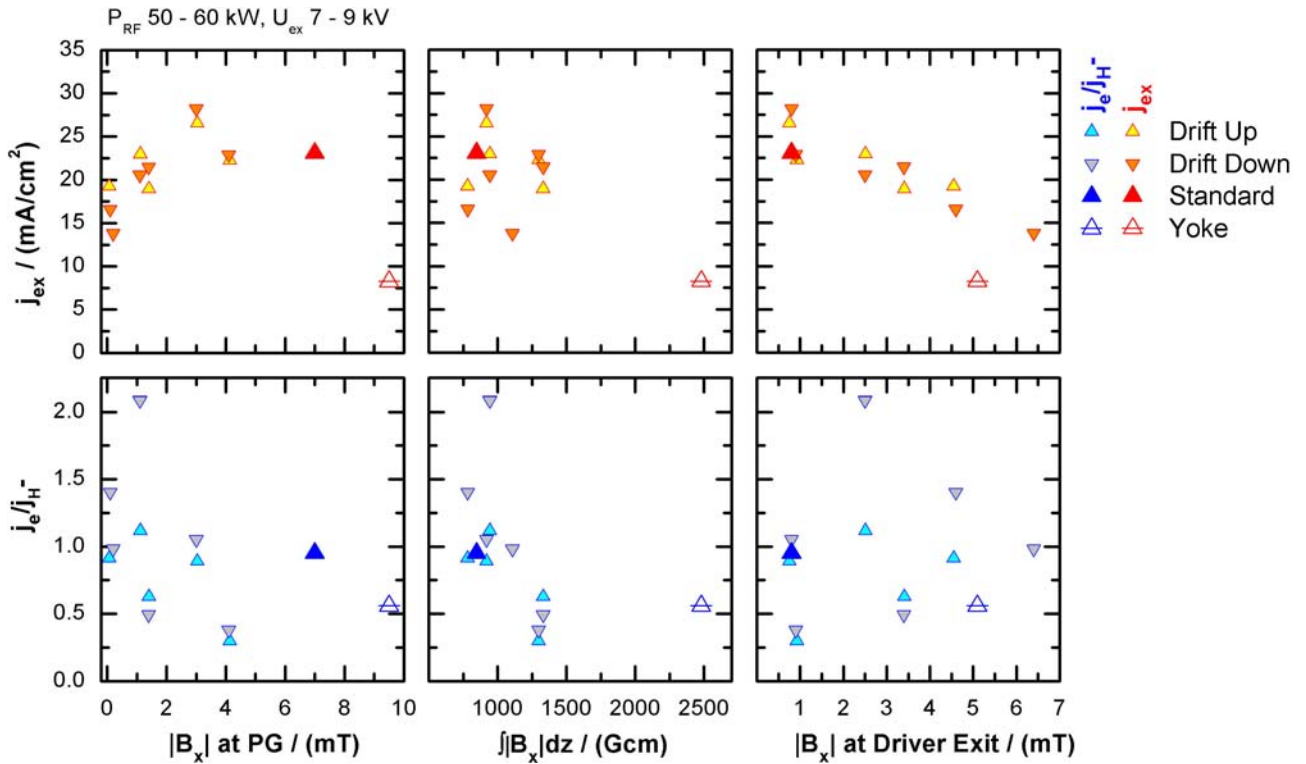
Figure 8: Performance of the IPP prototype source in dependence of the magnetic field parameters. Shown are the maximum achieved values of the extracted current density and the minimum achieved values of the ratio of the co-extracted electron current to the negative ion current. Left: in dependence on the magnetic field strength at the plasma grid. Center: in dependence of the integral Bdz value. Right: in dependence of the magnetic field strength at the driver exit. Data sets are chosen for a RF power between 50 and 60 kW and an extraction voltage of 7 to 9 kV.

possible explanation is the neutral depletion, i.e. the depletion of neutral gas, the latter being necessary to couple the RF power in the driver. If this is the case, the observed behavior indicates that the neutral depletion seems to be enhanced when there is a field in the driver. The latter, however, is also the case for the large RF sources where the filter field is generated by a current through the plasma grid. At that time, the sustainment of the driver plasma with magnetic field inside the driver at low source pressure was an open issue; but, in contradiction to the experience at BATMAN reported here, dedicated tests at RADI that had been performed due to this results showed no problems occurred with plasma sustainment at 0.2 Pa even when operated with maximum plasma grid current (5 kA). In this case, the field in the driver is comparable to the field at BATMAN when the filter field is positioned near the driver exit ("z=19"), but the filter field gradients are much smaller. For details see section 5.4.1. A possible explanation might be the larger source volume and hence less losses to the walls.

Figure 8 shows the maximum achieved extracted current density and the minimum achieved ratio of co-extracted electron to ion current in dependence on some parameters of the magnetic field configurations, i.e. on the magnetic field strength at the plasma grid and at the driver exit as well as on the integral BdL in the source. The data sets are independent, i.e. represent not necessarily the same discharge.
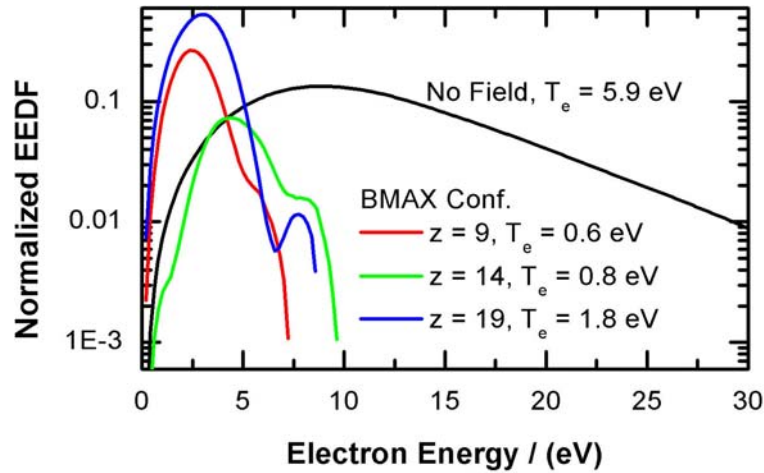
Figure 9: Electron energy distribution function near the plasma grid in the center of the source for the "BMAX" configuration with the different distance to the plasma grid and without magnetic filter field. The RF power was 40 kW, the extraction voltage 3 kV, 0.5 Pa, no Cs.

The figure shows clearly, that the extracted ion current density correlates with the magnetic field at the plasma grid and at the driver exit (both quantities have however some correlation, see figure 5), whereas the amount of co-extracted electrons correlates with the integral *Bdz* in the ion source. The maximum current density was achieved if the magnetic field strength at the plasma grid is around 3 mT and the magnetic field strength at the driver exit; the amount of co-extracted electrons is at lowest if the integral *Bdz* value is around 1250 Gcm. However, these magnetic field conditions could not be achieved simultaneously with the present possibilities. The data also show again, that there is not much difference of the source performance if the drift of the plasma is downwards or upwards.

The observed dependence of the extracted negative ion and electron currents on the magnetic field configuration cannot be explained by a simple model, but is due to the complex interplay between the different fluxes of positive ions and electrons from the driver to the plasma grid and the negative ion flux coming from the plasma grid and the different processes leading to negative ion extraction. For example, ion transport calculations [3] with the IPP Trajan Code showed that the extraction probability of negative ions increases with increasing filter field strength. But they fit into the picture: as the production and transport of the negative hydrogen ions occurs in the boundary layer near the plasma grid, the magnetic field near the grid plays an important role; the electrons, in contrast, are generated in the driver, so that their transport is determined by the magnetic field in the extraction region, represented by the integral *Bdz*.

Another example is the dependence of the electron temperature near the plasma grid in the center of the source on the position of the maximum of the magnetic field in the source. This is indicated in figure 9 for non-cesiated conditions, i.e. without a contribution of effects caused by surface generated negative hydrogen ions: The electron temperature increases by a factor of three when moving the field from the plasma grid ("z=9") to the driver exit ("z=19"), accompanied by a decrease of the electron density by a factor of ten (not shown here), although the *Bdz* value for the three "BMAX" cases is almost the same (see table 1). Hence, other effects (3D structure, gradients) play a role in electron cooling. Figure 9 shows also the main purpose

of the magnetic filter field: the cooling down of the electrons, i.e. reducing the electron temperature; the electron density however, is not reduced from the case without field compared to the "BMAX, z=9" case.

Another difference between the standard magnetic case and the magnet frame configurations is the much larger bias current needed for optimum electron suppression, 2 - 5 A in the standard magnetic field configurations, and 10 - 12 A for the magnet frame configurations having the maximum field strength more distant from the plasma grid. This is shown in figure 10. In all cases, the extracted ion current density depends only weakly on the bias current, the dependence on the magnetic field is much more pronounced. However, the amount of co-extracted electrons does also depend on the bias current, reaching some saturation value in the range of 10 - 12 A.

For comparison, also data for the standard configuration are shown, although some care should be taken in the comparison due to the problems of the RF power measurements discussed above, and due to the fact, that these data have not been obtained during a dedicated bias scan experiment as the data for the other magnetic configurations. The different behavior of the bias circuit can also be seen in the IV characteristics: the bias voltage for the "BMAX" and "BDL" configurations is much larger than for the standard case; this is also accompanied by an increase of the plasma potential, as measured by Langmuir probes. The reason for that difference is still open and part of the future experiments.

Figure 10: Performance of the IPP prototype source in dependence of the bias current for the different magnetic field configuration. The data for the "BMAX" and "BDL" configurations have been obtained in dedicated bias scans; the data for the standard configuration have been obtained during conditioning the source. All data are for 50 - 55 kW RF power and 9 kV extraction voltage.

3.1.3.2   Beam Optics

Figure 11 shows the dependence of the vertical beam width and the amount of ions hitting the calorimeter, i.e. the ratio of the extracted current to the accelerated current density, on the normalized perveance P/P_0. The latter is defined by
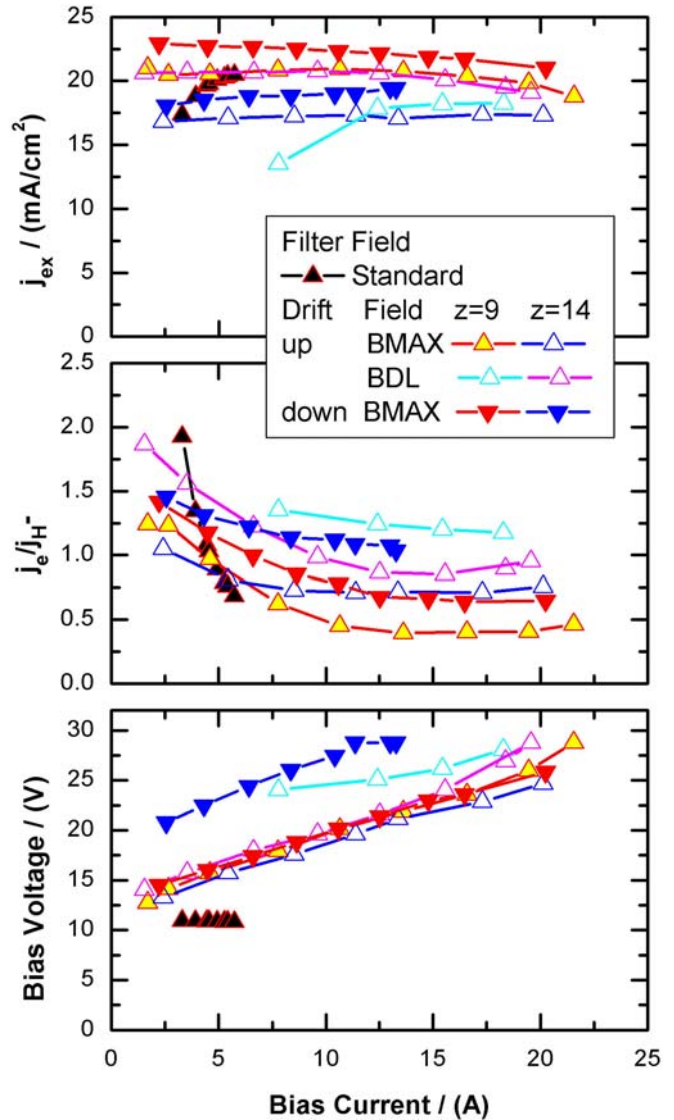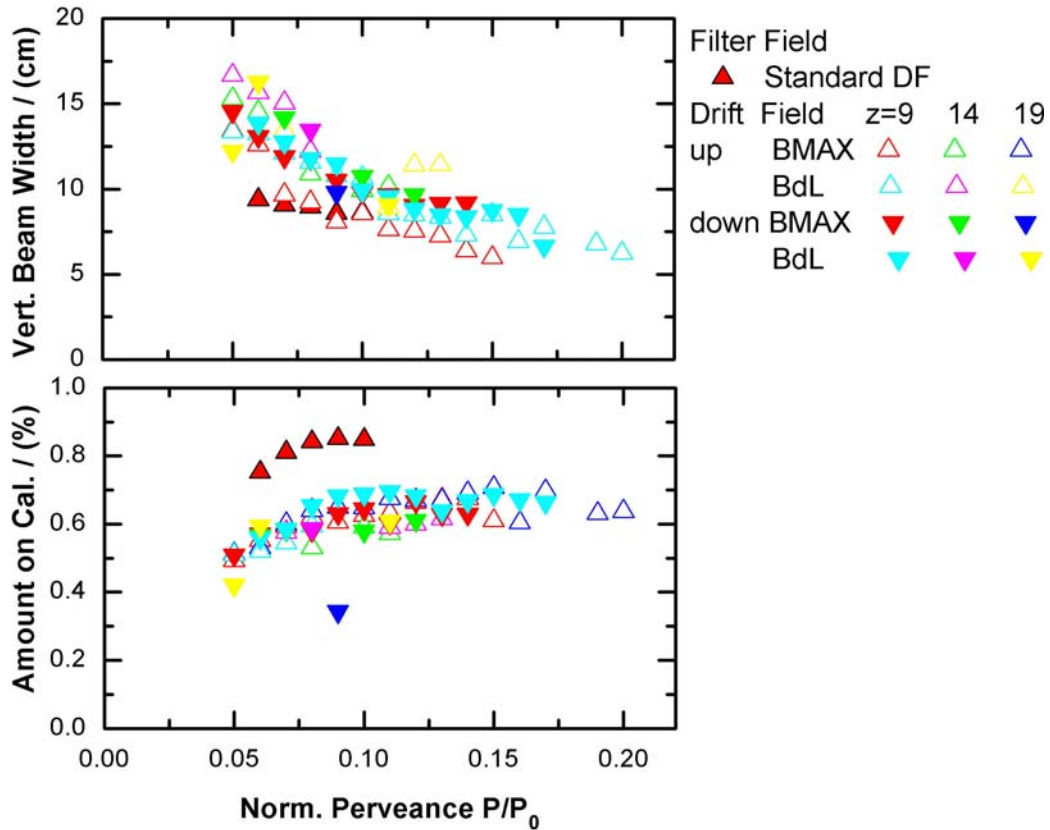
Figure 11: Performance of the IPP prototype source in dependence of the magnetic field configuration. Shown are the minimum achieved values of the vertical beam width and the maximum amount on beam current density at the calorimeter in dependence of the normalized perveance in intervals of 0.01. A vertical beam width of 5 cm corresponds to an average beamlet divergence of 26 mrad; 10 cm corresponds to 82 mrad.

$$\frac{P}{P_0} = \frac{j_{ex} / U_{ex}^{3/2}}{\frac{4\pi}{9} \varepsilon_0 \sqrt{\frac{2e}{m}} \left(\frac{r}{d}\right)^2} \; ;$$

j_{ex} being the extracted negative ion current density, U_{ex} the extraction voltage, r the aperture radius (4 mm for the LAG system) and d the distance of the extraction gap (3.5 mm for the LAG system). P_0 is the perveance of a planar diode.

It can be seen in figure 11, that the beam optics does depend on the magnetic field configuration. The best beam quality, i.e. the lowest values for the vertical beam width, have been obtained for the standard field as well as for the "BMAX" configuration with the drift in the upwards direction like in the standard configuration. This is somewhat surprising, as for these configurations the magnetic field in the accelerator is larger than in the other configurations (see figure 4). This indicates that other effects that changes with increasing perveance also influence the beam width. A candidate is the source symmetry that changes with changing current density and hence with changing perveance (see below) — which causes what is still not clear. Anyway, it seems that the differences are more pronounced for underperveant conditions, i.e. when the normalized perveance is below 10%; for optimum perveance — being for negative ion source in the

range of 10% to 15% — the vertical beam width depends only weakly on the magnetic field configuration. Unfortunately, the LAG system must be operated for high negative ion current density conditions in the underperveant range, as it was designed in the late 90's for an optimum perveance at 20 mA/cm^2 and 5.4 kV; all experiments (with the LAG system, the ITER like CEA system both for RF sources and arc driven sources) showed, however, that 20 mA/cm2 can only be achieved with an extraction voltage around 9 kV (see also Ref. [4]).

There is one remarkable difference between the standard field and all the other magnetic field configurations: with the standard field, the amount of ions hitting the calorimeter is significantly larger. It is not clear up to now whether this is an error of the ion current measurement due to the rebuild of the HV control system or whether this is caused by 'real' effects. The rebuild was done by replacing the unreliable voltage divider — being used for the data of the standard configuration shown here — by a second tetrode in 2008

In order to illustrate this, figure 12 shows the comparison of the vertical beam profiles for the standard and the "BMAX, z=9" configuration for the same perveance. Although the 'global' parameters (perveance and vertical beam width) are the same, some small differences at the beam edges might be seen, it looks like as the beam is somewhat shifted in vertical direction. Whether this implies an additional or increased 'halo' and whether this causes additional losses in the BATMAN extraction system or not, is an open issue; unfortunately, the measurement of the current at the grounded grid was not available due to technical problems for the experiments with the "BMAX" configuration.

Figure 12: Comparison of the vertical beam profiles for pulses with the standard and the "BMAX" magnetic configuration. All pulses have the same normalized perveance (0.11) and the same vertical beam width (8.9 cm). Other parameters (standard / BMAX): extraction voltage: 6.5 / 4.7 kV, acceleration voltage: 13 / 15 kV, acc. ion current density: 19.4 / 10.2, 7.7 mA/cm^2.

Another interesting feature is the dependence of the position of the beam maximum at the calorimeter on the source performance. In principle, the position of the beam at the calorimeter depends on the extraction voltage, as the deflection of the beam by the field in the acceleration depends on the ion velocity:

$$\theta \propto L / r_g \propto \int BdL / mv \; ,$$

θ being the deflection angle, r_g the gyro radius, and L the length of the deflecting zone — and on the symmetry of the source, as there might be an overlap of two (or more) different Gaussian beams from the different parts of the extraction grids according to the profile of negative hydrogen ions across the extraction aperture menisci. This overlap will also cause changes in the beam profile at the calorimeter.
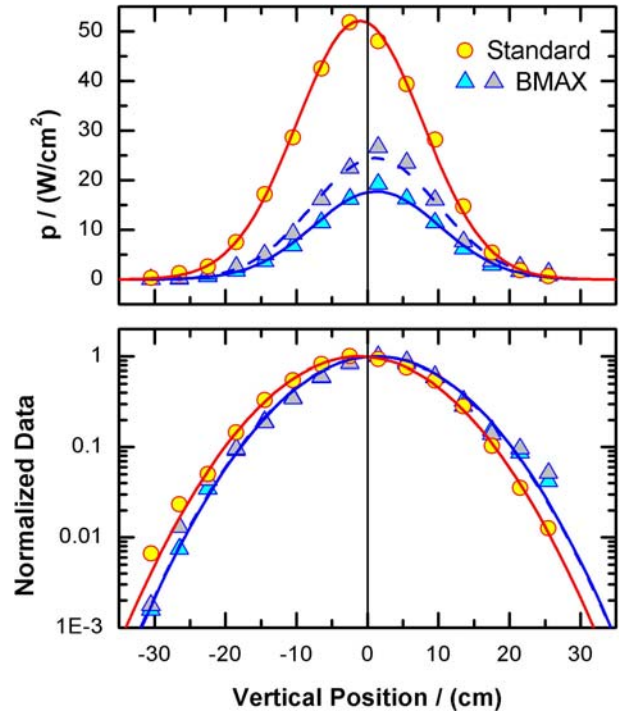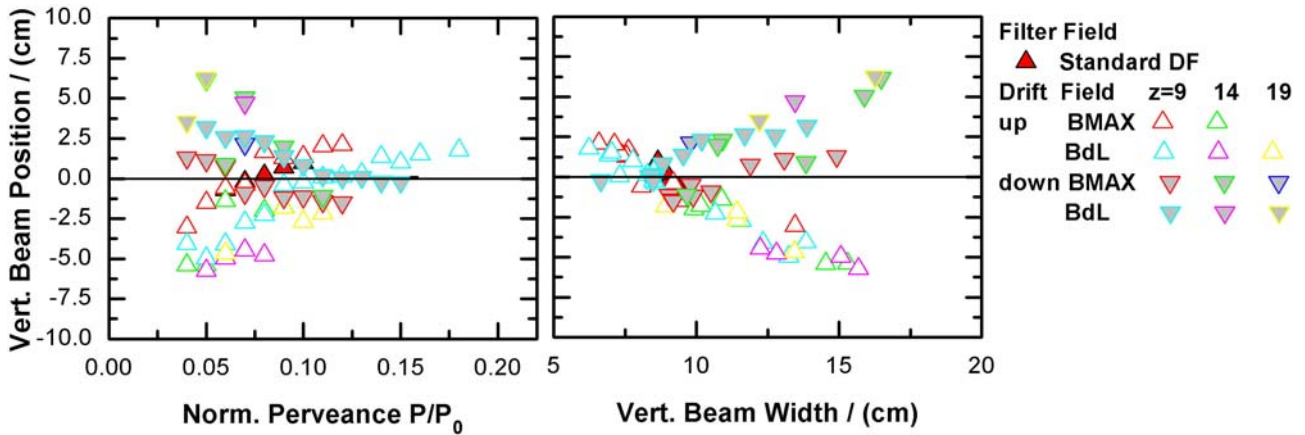
Figure 13: Dependence of the average vertical beam position on the normalized perveance and the minimum vertical beam width. Data are selected for intervals of 0.01 of the normalized perveance.

The data, however, show a clear dependence of the vertical beam position on the perveance (see figure 13), whereas the dependence on the extraction voltage — what would be expected from above — is less pronounced (not shown here). The dependence of the vertical beam position on the perveance is even more highlighted by the nice correlation of the vertical beam position with the vertical beam width (figure 13, right part). As already mentioned, the data shown in figure 13 are somewhat in contradiction to the expectations discussed above: For the LAG, low perveance means a high extraction voltage and hence, the beam deflection in the field within the accelerator should be less than for high perveance conditions, i.e. low extraction voltage. Furthermore, the deflection is less pronounced for the magnetic field cases with large magnetic field components in the accelerator (standard and "BMAX"). Hence, other effects must dominate the beam position. This will be discussed in the next section.

The vertical beam position shows also some more significant features: (1) the dependence of the deflection on the perveance is reversed when the magnetic field direction is reversed; this changes the direction of both the plasma drift in the ion source and the deflection of the beam within the accelerator; (2) the curves are symmetric with respect to the center of the extraction system and the calorimeter.

The beam profile dependencies observed are still an open issue, but these data offer a possibility for a better understanding of negative hydrogen ion production and extraction in cesiated sources. Beam optics calculations by IPR India are under way; but these codes must be coupled with source codes or data regarding the asymmetry of the negative hydrogen ion density across the plasma grid. First data of the plasma asymmetry and its correlation with the beam properties are discussed in the next section.

3.1.3.3 Source Symmetry

The plasma asymmetry S_p in the negative ion source is defined in this report by

$$S_p = \frac{\int \varepsilon_{H_\beta} dx_{top}}{\int \varepsilon_{H_\beta} dx_{bottom}} - 1;$$

the corresponding horizontal ("*x*") line-of-sights are shown in figure 14; the used line-of-sights collect the light nearly in the center of both grid halves at a distance of 7 mm from the plasma grid. The H_β line emission is used, as it is in the most cases available, the H_α line is frequently overexposed when the spectrometers are used for measurements of the Cs 852 nm line. Furthermore, the H_β emission is solely caused by collision of atoms and ions with electrons and reflects so the 'plasma' conditions, whereas the H_α emission results also from mutual neutralization of positive and negative ions.

With this definition, a homogeneous source is characterized by $S_p = 0$. Positive values of S_p indicates that the plasma Balmer emission is more pronounced at the upper part of the source, i.e. a drift upwards, negative values of S indicate accordingly a drift downwards.

Figure 15 shows the dependence of the plasma asymmetry on some of the magnetic field parameters for the cases with the magnet frame. The bars do not indicate the error, but the upper and lower value of the respective dataset and so the range of the data for a given magnetic field configuration. There is a strong linear correlation between the plasma asymmetry and the magnetic field strength at the plasma grid, less
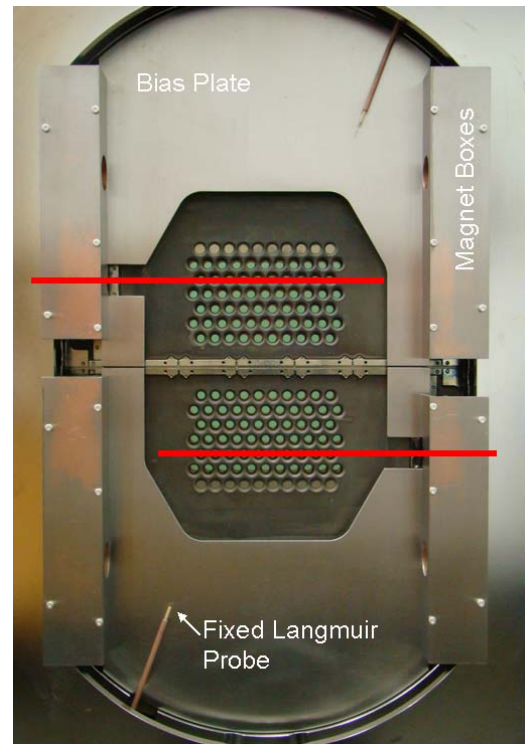

Figure 14: View onto the plasma grid with bias plate of the IPP prototype source at BATMAN. Also indicated are the line-of-sights for the OES measurements of the plasma asymmetry. Both have a distance of 7 mm from the plasma grid.

correlation with the magnetic field strength at the driver exit — the latter two magnetic field quantities have also some correlation in this range (see figure 5) — and no correlation at all between the plasma asymmetry near the plasma grid and the integral magnetic field *Bdz* in the source. This indicates that also the plasma drifts near the plasma grid in total, not only the negative ion transport, is determined by the magnetic field near the plasma grid.

Furthermore, the dependence of S_p on the magnetic field strength is reversed when the magnetic field direction, i.e. the plasma drift direction, is reversed. However, this dependence is not symmetrically with respect to zero, it seems that there is an 'intrinsic' offset of about 12% plasma asymmetry.

Although this 'intrinsic' offset of the plasma asymmetry might be caused by measurements errors — the error of the H_β line emission is in the range of 10%, it might also be caused by the asymmetric position of the Cs oven. The plasma asymmetry in the IPP cesiated negative hydrogen ion source has in principle two causes: (1) the vertical plasma drift in the filter field leading to an asymmetry of the transport of the negative ions — due to an asymmetric distribution of positive ions needed for space charge compensation — and of the destruction of negative ions by electron collisions; (2) an asymmetry of the negative ion production at the plasma grid due an asymmetric quality of the Cs layer at the plasma grid as the Cs oven is positioned on top of the source.
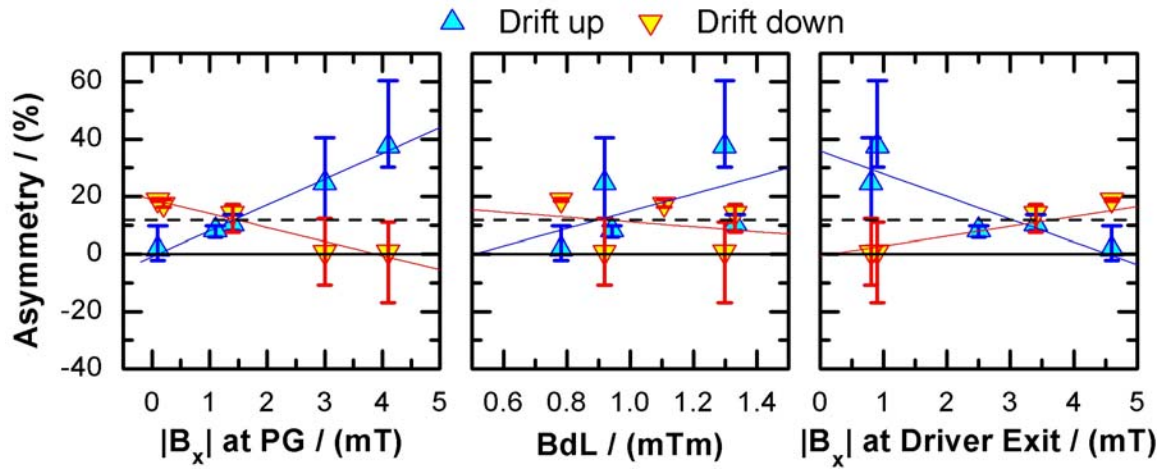
Figure 15: Dependence of the plasma asymmetry near the plasma grid on the magnetic field parameters. Shown are the average values as well as the maximum and the minimum value, indicated by the bars, for pulses with an RF power between 50 and 60 kW, an extraction voltage between 7 and 9 kV and a bias current between 9 and 12 A.

Figure 16 shows the dependence of the plasma asymmetry on the bias current. The asymmetry factor increases for the plasma drift being upwards and decreases for plasma drift downwards, respectively, with increasing bias current. Again, there seems to be an 'intrinsic' offset in the asymmetry of around 20%. The observed dependence, however, contradicts completely to the dependence of the plasma asymmetry on the bias current for the standard magnetic configuration. Due to the lack of data with exactly the same parameters as shown in figure 16, figure 17 shows published data [5] for the standard magnetic field configuration: it can be clearly seen, that here the plasma symmetry improves with increasing bias current, from S_p = 30% for 0 A bias current to S_p = 10% only for 16 A bias current. The improvement of the plasma symmetry with increasing bias current was a general trend for the standard magnet configuration, regardless on RF power, Cs conditions, bias plate present or not, or even changes of the magnetic field by adding additional rods at the source body that strengthened or weakened the standard magnetic field.

The dependence of the plasma asymmetry on the bias current for the standard magnetic filter field fits also in the present understanding of the drifts: these are most probably caused by a kind of *ExB* drift, where the electric field is generated by the difference of the potential of the plasma grid (i.e. the bias voltage) and the plasma potential in the source. The lower this potential difference, the less the drift is pronounced, and the plasma symmetry improves. This is indicated also in figure 17: the difference decreases with increasing bias voltage and subsequently the symmetry improves until the potential difference is zero. A further increase of the bias voltage (above the plasma potential) does not improve the symmetry further. (N.B.: deuterium plasmas are generally more symmetric than hydrogen plasmas and show a much less pronounced dependence of the plasma asymmetry on the bias current.)

Figure 17 shows another remarkable change of the source behavior for the present experiments: the dependence of the extracted current density on the bias current is much stronger for the standard filter field configuration as for the cases with the external magnet frame (see also figure 10). The reason for the differ-
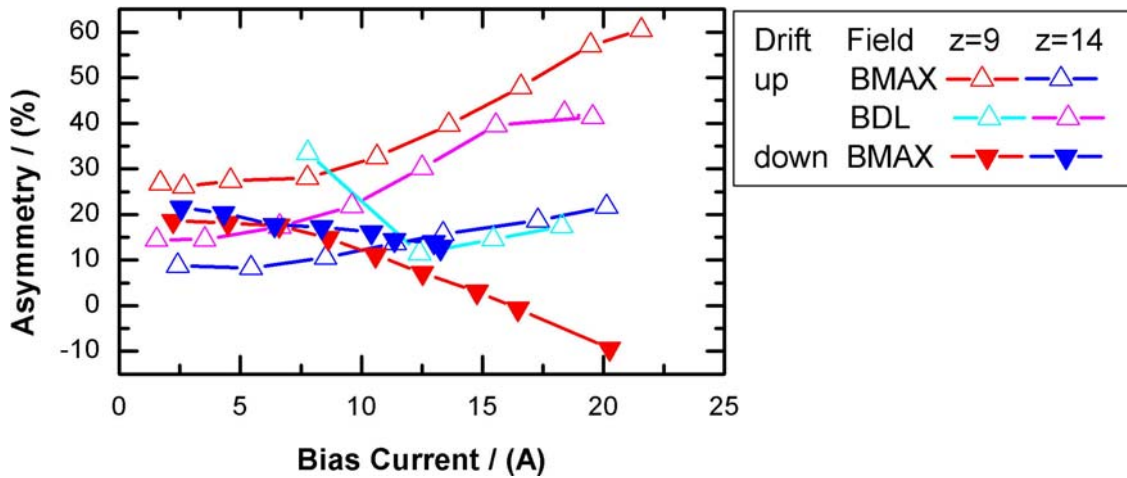
Figure 16: Dependence of the plasma asymmetry on the bias current for the various magnetic field configurations. Same data set as in figure 10.

ent dependence of the plasma asymmetry and source performance on the bias current for the magnetic field configurations with the external magnet frame is not understood yet. The main difference between the magnetic frame configurations and the standard field is that in the latter case the maximum field strength is closer to the plasma grid and that the magnetic field gradients at the source edges are smaller and that the field free region is closer to the driver exit. As already mentioned above, Langmuir probe measurements show a much larger plasma potential for those configurations than for the standard field for unknown reasons. Detailed data evaluation is under way.

The plasma asymmetry is also correlated with changes of the beam properties. A first example is given in figure 18 where the dependence of the vertical beam position on the plasma asymmetry is shown. The dataset is the same as shown in figure 10 and figure 16; all pulses for a given magnetic field configuration have the same extraction voltage and have almost the same perveance, as the asymmetry was changed by the bias current and that does not change the extracted current density considerably. Hence, the changes of vertical beam position for the data set shown in figure 18 are caused mainly by the different magnetic field configurations by two effects: (1) due to the different deflection of the beam within the accelerator field and (2) to a smaller amount, due to changes of the plasma asymmetry causing different contributions of the different plasma grid areas to the beam.

Figure 18 shows some interesting features that are part of the ongoing and future data evaluation and experiments. One of that is that the majority of the beam is created at parts of the plasma grid opposite to the plasma drift; i.e., in the case of the plasma drifting upwards, more negative ions are extracted from the lower part of the source and vice versa. This behavior is consistent with measurements of the beam properties at MANITU with the spatial resolved H_α Doppler-Shift spectroscopy system.

The fact that the beam comes mainly from the region opposite to the drift direction can be explained by the physics of negative ion generation and destruction of negative ion sources: even if the generation of negative hydrogen ions is more or less symmetric due to the fact that most of them are generated by neu-
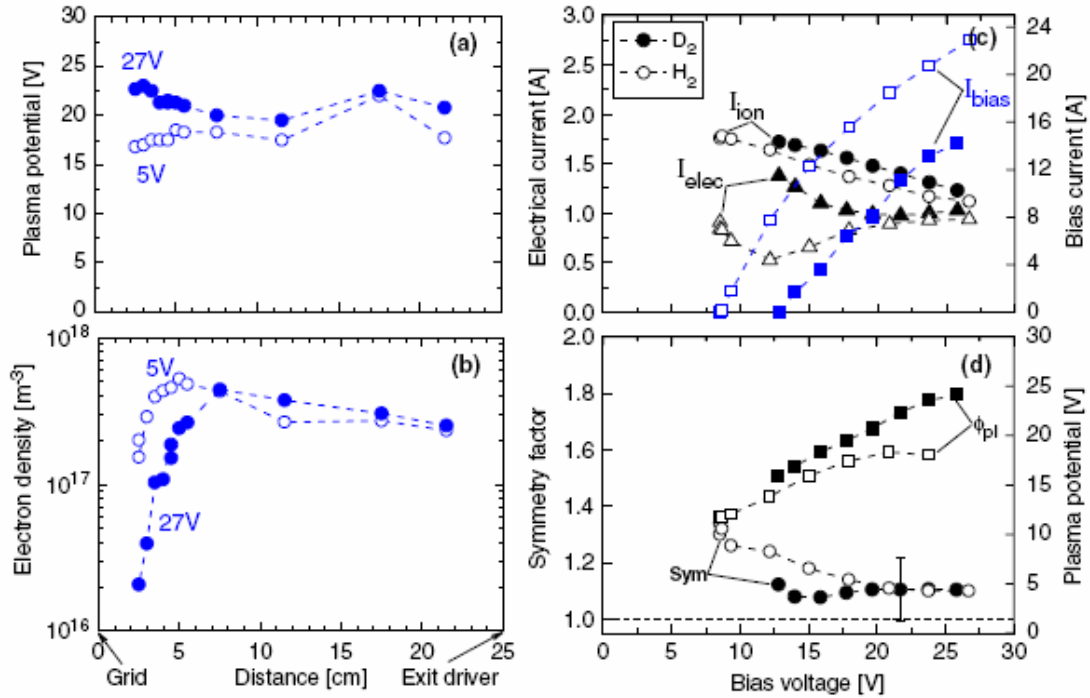
Figure 17: Plasma symmetry (d) at BATMAN in dependence on the bias voltage / current for standard magnetic field configuration (figure 3 in Ref. [5]). The symmetry factor is defined here just by the ratio of the line emission without subtracting 1.

trals, the destruction of these ions prevails in the region of the ion source, where the drift goes, i.e. in the region with enhanced electron density and perhaps also enhanced electron temperature. This effect seems to dominate also over the space charge compensation by positive ions; the positive ion density across the plasma source seems to be more symmetric than the electron density. This is confirmed by measurements with the fixed Langmuir probes that showed an electron-ion-plasma in the region where the drift goes and an ion-ion-plasma in the region opposite to the plasma drift.

The details of the dependence of the vertical beam position on the plasma symmetry are still not understood: there is at first glance no correlation of the deflection with the amount of magnetic field in the accelerator (see also figure 13 and the respective discussion on page 25). The beam position in the case of the drift upwards is more downwards for the "BMAX" field at z=14 as at z=9, in the latter case the field in the accelerator is almost three times larger (see figure 4 and table 1). The same trend is observed for the "BMAX" case with the drift downwards. In contrast, there is almost no difference observed for the BDL case at z=9 and z=14, respectively, although also here the field in the accelerator differs by almost a factor of three. Furthermore, the latter cases show no clear dependence of the vertical beam position on the plasma symmetry.

Hence, other effects play a role, possible candidates are 3D effects of the magnetic field in the accelerators (edge effects, or a dependence on the gradients) or, more probably, that the correlation of the plasma symmetry, measured by a ratio of the Balmer line emission in a distance of 0.7 cm from the plasma grid, with the symmetry of the extracted current density profile of the negative hydrogen ions at the plasma meniscus near the extraction aperture is not straightforward. The latter quantity, however, is experimentally not simply accessible.
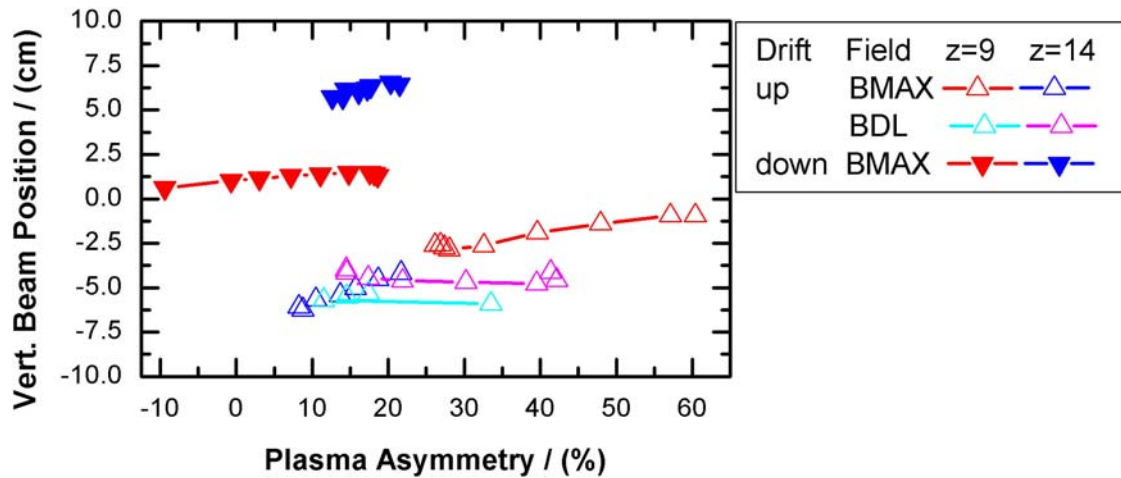
Figure 18: Dependence of the vertical beam position on the plasma asymmetry for the different magnetic field configurations. All pulses for a given magnetic field configuration have the same extraction voltage and the same perveance.

Meanwhile, first calculations of the beam deflection within the field from GG to the calorimeter for a symmetric divergence profile have been started with a beam transport code (see section 7.1). Although some general trends could be validated — the deflection is larger for the "z=14" case as for the "z=9" case —, the amount of deflection is much less (~cm instead of several cm's as shown in figure 18). The analysis including asymmetric divergence profiles is ongoing.

3.1.3.4   Plasma Parameters

Two RF compensated movable Langmuir probe were used to scan the plasma parameters (electron and positive ion densities, plasma and floating potentials, electron temperature) from the driver exit up to the neighborhood of the plasma grid. The BMAX filter field configuration was set in the "z=9", "z=14" and "z=19" configurations. The probes were symmetrically located in order to obtain profiles from top and bottom locations in the expanding chamber as can be seen on figure 19. The probe dimensions are 25 μm radius and 5 mm length. Both can move up to 225 mm which corresponds to a distance of 2.5 mm from the PG.

RF compensation was a critical aspect of this study. Indeed, depending on the used RF filter, a ground loop appeared which created a distortion of the IV curve as shown on figure 20. The red curve on figure 20 shows a "flat" dependency of the current in the electron branch instead of the expected exponential increase. Moreover, this curve shows no plasma potential since there is no saturation in the electron current. The black curve was obtained after the ground loop was fixed, and has a regular Langmuir probe shape.
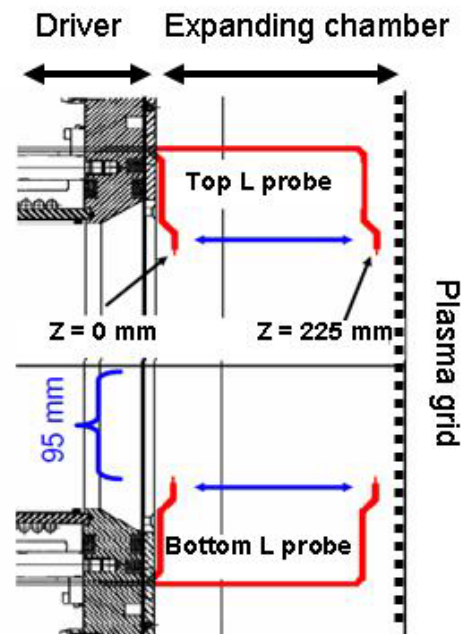

Figure 19: Location of the L probes

30

Figure 21 compares the plasma symmetry with the FF position measured by spectroscopy and Langmuir probe. The ratio of the bottom over top (probe ion density or H beta emissivity) measurement is plotted. Sym PG and Sym PG spectro are the ratio of the of the L probe ion density and H beta emissivity respectively taken near the PG. Sym driver represents the ion density ratio taken only with L probe close to the driver exit since no spectrometer LOS are available at this position. It appears from figure 21 that the position of the magnetic field strongly influences the symmetry of the plasma depending of where the measurement is taken. Indeed, it can be seen that when the magnetic FF is located near the PG ("z=9"), a better symmetry is observed close to the driver exit, while a strong asymmetry can be seen near the PG. On the contrary, shifting the FF near the driver exit ("z=19") leads to the opposite results: a higher asymmetry is observed near the driver exit while the plasma near the PG is more symmetric. The good agreement between spectroscopy measurements and L probe evaluation confirms this interpretation. From figure 21, it then appears that the highest asymmetry follows the FF position. Consequently, a cross B drift, and most probably an E x B drift is the probable explanation of this behavior.

Figure 20: Influence of a ground loop in the RF compensation filter on the IV curve

We will now discuss the variation of the plasma parameters measured by the movable L probe and obtained for different FF position. Figure 22a) recalls the magnetic field intensity for the three positions from PG to the driver. Figure 22b) and c) show the measured positive ion density and electron temperature for the top (square) and bottom (star) probes, while figure 22d) exhibits the plasma and floating potentials of the top probe. All these measurements were obtained with a drift down, the results for a drift up being symmetric by reversal of top / bottom probes.

Let us first describe the positive ion density profiles behavior. For the three FF position, it is observed a strong density gradient in favor of the top probe in the driver exit vicinity. The "z=9" case shows a decrease of the density of the top probe all along the probe path while the bottom probe shows an increase of the density followed by a maximum and a decrease when going from the driver exit towards PG. The increase of the bottom probe ion density being concomitant with the decrease of the ion density of the top probe, it is assumed, having in this case a drift down, that the plasma flows from the top part of the expanding chamber to-
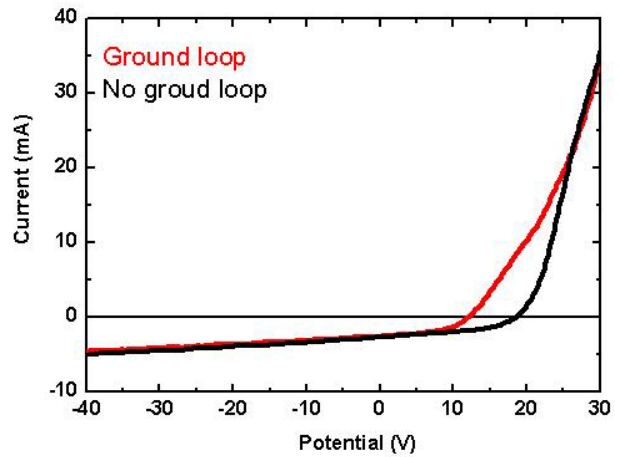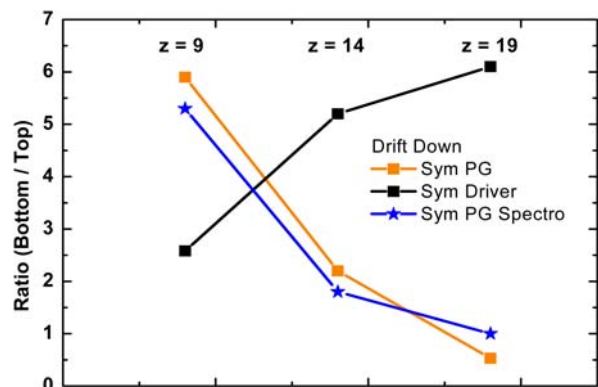

Figure 21: Bottom over Top ratio of the positive ion density (Sym PG and Sym Driver) and H beta (Sym PG spectro)

wards the bottom part. The maximum of the ion density measured by the bottom probe is reached closely to the maximum of the FF intensity, thus when the drift is enhanced. The decrease observed in the ion density measured by the bottom beyond this point is thought to be due to electrons losses to the walls, as they follows the FF magnetic field lines.

A same behavior is observed when the FF is moved in the "z=14" position: a decrease in the top probe ion density is observed in favor of the bottom probe. The maximum of the ion density measured by the bottom probe is reached near the maximum of the FF intensity. Beyond that point the plasma is homogenous as top and bottom densities are the same.

The "z=19" case is different. First of all, the density at the driver exit of top and bottom probes is by far lower compared to the two previous cases. It is thought to be due to the FF position: in this configuration the FF intensity at the driver exit is larger than for the previous cases and thus, the electrons following the field lines, losses to the walls occurs at the beginning of the expanding chamber, explaining the density drop. Besides a lower density, it can be seen a decrease of the top probe ion current, while the bottom probe density remains stable. For the three FF positions, a drift towards the bottom part of the expanding chamber is observed leading in most of the cases to and increase of the ion density in this part of the chamber.

Comparison between the electron temperatures of figure 22c) shows, as expected, for top and bottom probes, a higher electron temperature near the driver exit ("z=9", in red), when FF is far from it. The FF influence on the electron temperature is straightforward: in all the cases a decrease
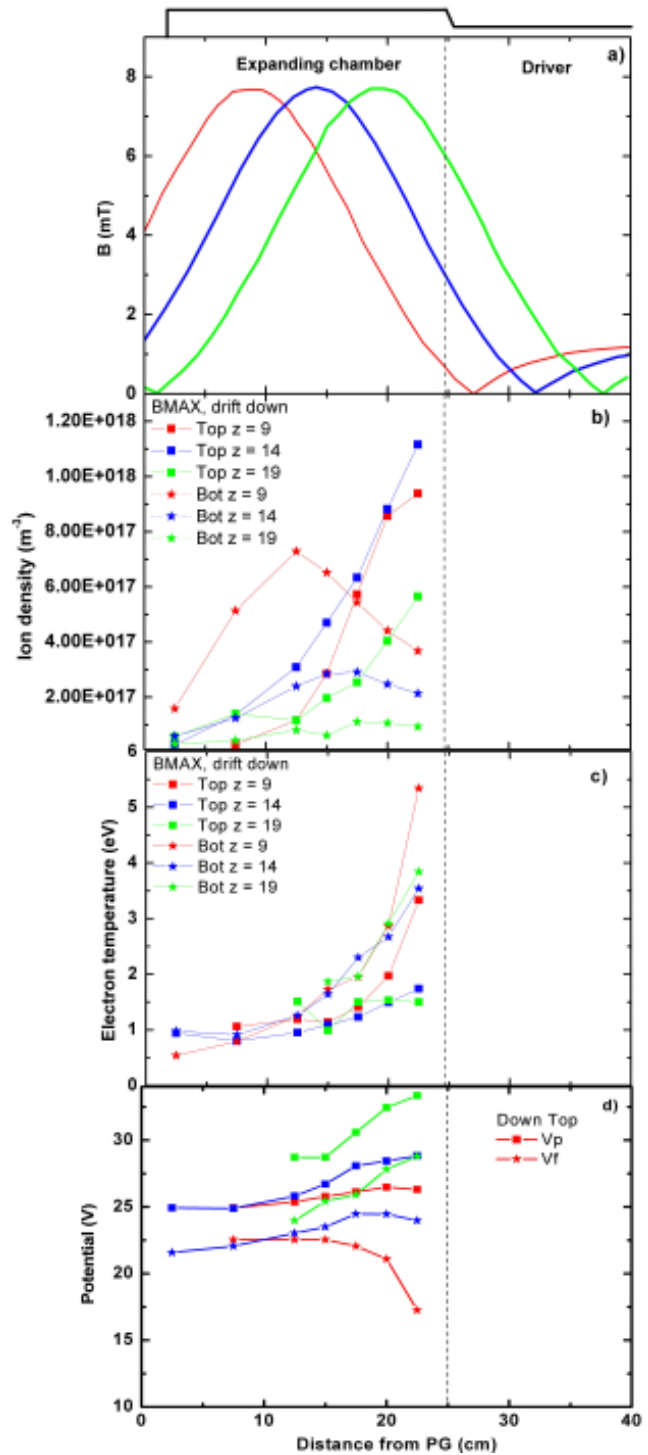

Figure 22: a) recalls the FF strength for the three different positions, b) the positive ion densities for the top L probe (squares) and bottom L probe (stars), c) the electron temperature and d) the plasma and floating potentials for the top L probe only. All these measurements were performed with a drift down, the colors in b), c) and d) corresponding to the FF positions in a).

is observed when going from the driver exit towards the PG. The electron temperature difference between top and bottom probes, especially near the driver exit is still under investigation.

Plasma potentials profiles are plotted on figure 22d). Comparing the profiles near the driver exit shows that the plasma potential is high when the FF is in the "z=19" position (in green) and lower when the FF is far from it (in red for "z=9"). High plasma potential being related to higher electron losses, this confirms that as electrons follows the field lines, more losses occurs near the driver exit when FF is in the "z=19" position, this result being in good agreement with the lower measured ion density (in green on figure 22b). The high voltage difference between plasma and floating potential is also in good agreement in the case of the "z=9" FF position, with the high electron temperature at the driver exit (in red on figure 22c) and d).

3.1.4   Results in Deuterium

Due do the technical problems with water and air leaks in fall 2010 the magnetic filter field studies with deuterium started at the end of the contract only. Hence, only some preliminary results obtained in December 2010 are shown in this final report. The experiments have been joined by personnel from CCFE.

The main problem regarding deuterium operation is the much larger amount of co-extracted electrons than in hydrogen. Hence, larger filter fields are needed than in hydrogen. Both effects lead to problems for a systematic evaluation of the effect of the different filter field parameters on the performance, in particular:
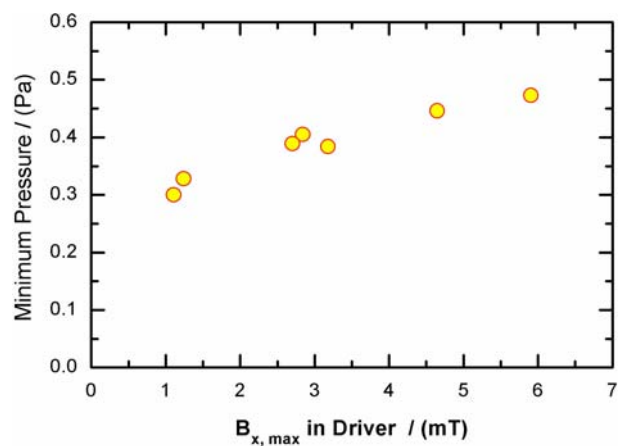

Figure 23: Minimum pressure at BATMAN for plasma sustainment in deuterium operation in dependence on the maximum magnetic filter field strength in the driver.

- The power on the extraction grid limits the parameter region for the filter field, RF power and extraction voltage. This is additionally hindered by the fact that the maximum allowable power was reduced from 25 kW (i.e. 200 W/aperture) for the hydrogen phase to 20 kW (160 W/aperture) in order to avoid further water leaks at the extraction grid.

- Increasing the filter field means also, that due to the present technical setup of the magnet frame the field in the driver also increases. This leads, as already mentioned in section 3.1.3.1, at BATMAN to problems with the plasma sustainment at low pressures. A first evaluation of the data showed, that the minimum pressure for plasma sustainment depends on the magnetic filter field strength in the driver (see figure 23). But this dependence is most probably a particular characteristic of the small IPP prototype source; experiments at RADI showed that for larger sources the plasma sustainment is not problematic even for pressures down to 0.2 Pa (see section 0).
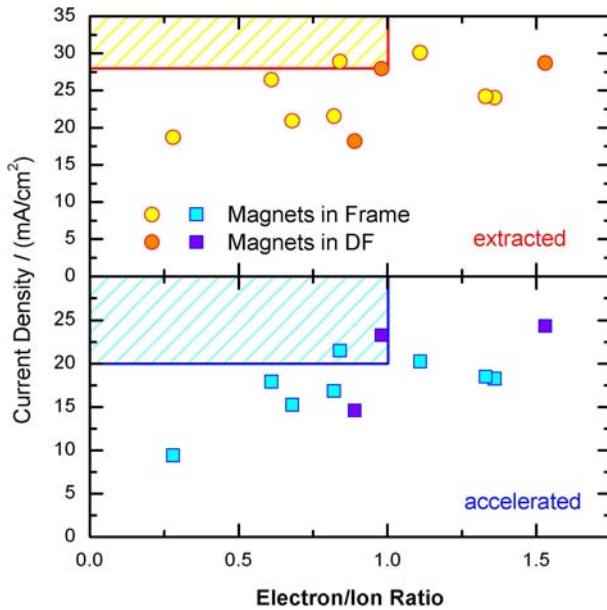
Figure 24: Performance of BATMAN in deuterium operation. Top: extracted current density vs. electron/ion ratio; bottom: accelerated current density vs. electron/ion ratio. The dashed areas denote the ITER requirements.
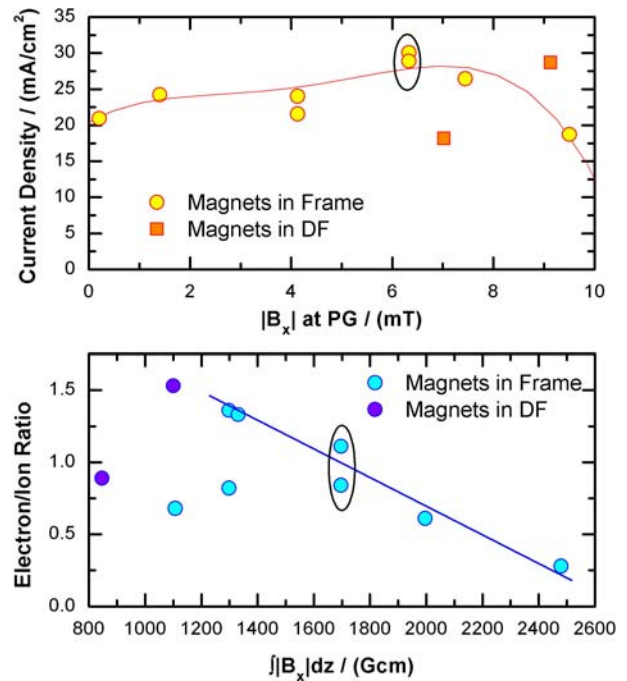

Figure 25: Top: dependence of the extracted current density in deuterium on the magnetic filter field strength at the plasma grid. Bottom: dependence of the electron/ion ratio in deuterium from the integral BdL value. Note; both field parameters are correlated (see figure 6). The indicated best performance has been obtained with the "BDL, z=9, side bars only" configuration.

Both effects had the consequence, that up to now no consistent data set was achieved, i.e. performance measurements at identical parameters for all magnetic field configurations. However, some important and encouraging results have been obtained.

Figure 24 shows the overall performance for the magnetic filter field configurations used so far. The results, however, have been obtained for different parameters regarding extraction voltage, RF power and pressure. The best results, however, have been obtained at a filling pressure of 0.35 Pa, an extraction voltage of 8.5 kV and a RF power of 67 kW. Furthermore, the former results from 2005 with the standard magnetic field configuration could be achieved also with the magnets in the magnet frame.

Figure 25 shows as a first example of the dependence of the extracted current density on the magnetic filter field strength at the plasma grid and the dependence of the electron ion ratio on the integral BdL in the source. Due to the reasons discussed above, the present data set does not allow a clear separation of the effects, as there is no consistent data set for all magnetic field configurations and as there a strong correlation of the filter field parameters (see figure 6). But deuterium shows the same trends as hydrogen, but with larger absolute values: for sufficient ion extraction some field at the plasma grid is necessary, and for sufficient electron suppression a sufficient large BdL is necessary. The best values so far have been obtained with the "BDL, z=9, side bars only" configuration with about 6 mT field at the plasma grid and an integral BdL value of 1700 Gcm.

3.2 Basic Investigations on Helicon Discharges

3.2.1 Background

At present rather high RF power is needed to generate the plasma in the driver of the IPP RF driven negative ion source. Hence, it would be desirable to reduce the power needed to sustain the same plasma in order to have more operational margin and reliability and/or cost reduction.

Furthermore, it is also desirable to reduce further the source filling pressure. This would reduce the stripping losses and enhance the overall efficiency of the NBI system as well the pumping and grid cooling requirements.

Experiments at MANITU and BATMAN have shown that the present inductive coupling has a lower pressure limit as the RF depletes the driver and hence no discharge can be sustained below that limit. The exact value of the limit depends (most likely) on the driver, the source geometry, and the gas flow; it is however for the IPP RF source just below 0.3 Pa.

Hence, a new concept of RF plasma heating allowing the generation of a dense enough plasma at pressures well below 0.3 Pa will provide many advantages. A very promising candidate which even needs no change of the driver concept is the helicon discharge by using an RF antenna with special geometry together with a magnetic field.

Typically, discharges operated in the helicon mode have an electron density that is roughly an order of magnitude larger than an ICP discharge at the same power. Most experiments so far have been done in rare gases (mostly argon) at 13.56 MHz, at low RF power levels (below 10 kW) and small cylinder (5 cm od) for plasma generation.

The aim of the experiments is to explore the possibility of generating helicon(-like) discharges in an IPP RF driver. Even if not the full helicon mode can be achieved, an increase of a factor 2 in the RF efficiency will have a big advantage.

The experiments are performed mainly at the University of Augsburg for the basic understanding and principle investigations on Helicon discharges in hydrogen/deuterium. A new experiment has been built in the framework of a diploma thesis from already available equipment (vacuum flanges, pressure gauges, gas flow meters, permanent magnets) and from new equipment (RF generator, matchbox, Helmholtz coils with power supply) bought from ITER money. First basic experiments will be presented in this report. Further investigations will be carried out in the framework of a PhD thesis; having the input from the basic experiments, helicon experi-
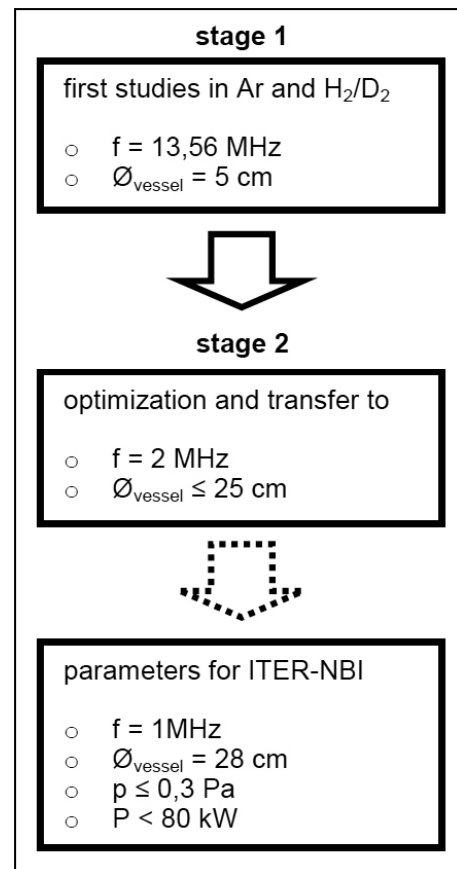
stage 1

first studies in Ar and H_2/D_2

○ f = 13,56 MHz
○ $\varnothing_{vessel}$ = 5 cm

stage 2

optimization and transfer to

○ f = 2 MHz
○ $\varnothing_{vessel} \leq$ 25 cm

parameters for ITER-NBI

○ f = 1MHz
○ $\varnothing_{vessel}$ = 28 cm
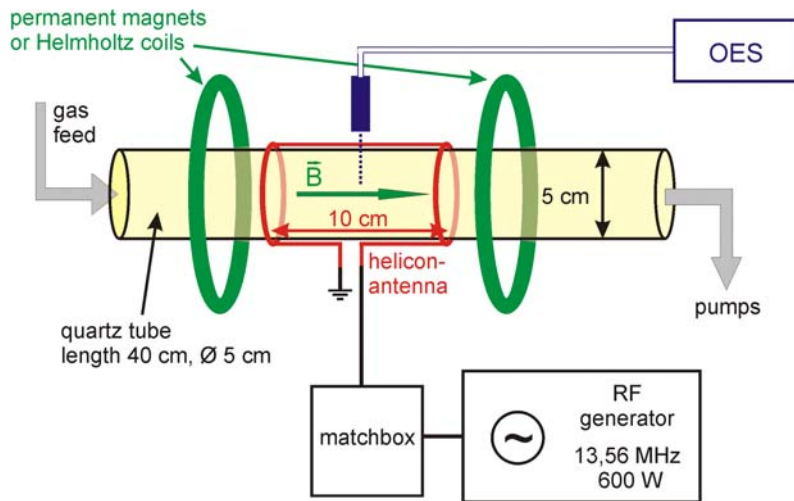○ p ≤ 0,3 Pa
○ P < 80 kW

Figure 26: Strategy

Figure 27: Experimental setup.

ments are then also planned at BATMAN, also to test the concept with extraction.

These experiments were accompanied by investigations at BATMAN to generate an improved confinement with a parallel magnetic field in the driver (parallel to axis) without changing the coil geometry.

3.2.2 Helicon Experiments (University of Augsburg)

The strategy for first basic investigations on helicon discharges at the University of Augsburg is as follows (see figure 26):

Initially an experimental setup was installed in which argon and hydrogen/deuterium plasmas can be generated in vessels of 5 cm or 10 cm in outer diameter and at the standard RF frequency of 13.56 MHz. The detailed setup and the experimental results obtained in this "stage 1" will be presented in the following chapters. The reason for using both argon and hydrogen was to achieve certain comparability with other Helicon experiments that mostly have been and are done in rare gases.

In "stage 2" the experiment will be optimized and transferred to larger plasma vessels and a lower RF frequency of 2 MHz – values being closer to the intended parameters for ITER-NBI (1 MHz, 28 cm od).

The general idea behind the pursuit of the depicted strategy is to have a flexible setup starting from a standard helicon configuration and then to explore the helicon discharge towards IPP/ITER driver geometry and RF frequencies.

3.2.2.1 Experimental Setup

The current setup of the helicon experiment is shown schematically in figure 27. As mentioned before this setup corresponds to "stage 1" of the depicted strategy.

It consists of a cylindrical quartz tube (40 cm length, 5 cm or 10 cm od) integrated into a vacuum system that can be filled with different gases via a gas flow meter (hydrogen: max. 7 sccm/min). Operating pressure is measured by a capacitive pressure gauge and was in the range between 0.3 and 10 Pa for all investigations so far.

Generation of the plasma is achieved through a helicon antenna (a so called Nagoya antenna) that surrounds the quartz tube and is connected to the RF generator (13.56 MHz, max. 600 W) via a matching network (commercially available VarioMatch™ by Advanced Energy). Alternatively, a coil (three windings) can be used instead of the antenna to compare results with standard ICP configuration.

In order to produce a helicon discharge one also needs a constant magnetic field parallel to the cylinder axis. The generation of this magnetic field was realized by two different methods: either by an array of permanent magnets or by a pair of Helmholtz coils.

For the usage of permanent magnets (CoSm magnets with dimension of 9x13x50 mm^3 – the same magnets as used for the magnetic filter field studies in section 3.1) two frames for up to eight permanent magnets each have been built (geometry see figure 28). The resulting axial field when both frames are installed at a distance of 20 cm is displayed in figure 29. In the antenna region the field strength is about 10 mT in this "permanent magnet configuration" (PMC). Its most evident feature is the reversal of the magnetic field under

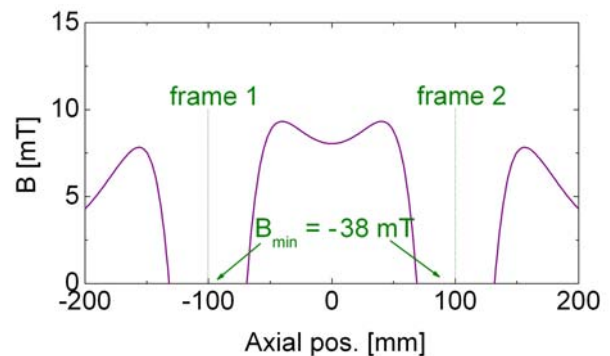*Figure 28: Frame for up to eight permanent magnets.*

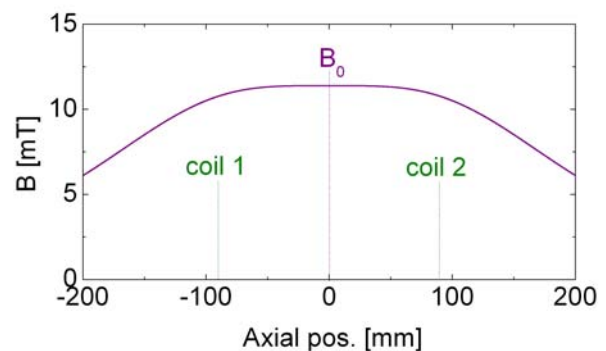*Figure 29: Axial magnetic field in the permanent magnet configuration (PMC)*

Figure 30: Axial magnetic field in the Helmholtz coils configuration (HCC)

the frames. Hence it is no surprise that the plasmas produced in the PMC are strongly inhomogeneous in axial direction.

Alternatively, the magnetic field was produced by a pair of Helmholtz coils (380 windings and 18 cm radius each). The axial field in the "Helmholtz coils configuration" (HCC) scales with electrical current carried by the coils and is displayed in figure 30 for a current of I_c = 6 A through each coil. It is obviously far more homogeneous than in the PMC and furthermore does not show the field reversal. Accordingly, plasmas produced in the HCC are more homogeneous than those produced in the PMC. A big advantage of the HCC is the possibility to vary the magnetic field under operating conditions. The accessible range of the field

strength was limited to $B_0 \approx 14$ mT (corresponding to I_c = 7 A). By installing better cooling components, the maximum magnetic field can be increased to approximately 20 mT in future experiments.

Diagnostics have been carried out by Optical Emission Spectroscopy (OES) in argon, hydrogen and deuterium as well as in both magnetic configurations. The high-resolution spectrometer is characterized by $\lambda_{FWHM} = 0.05$ nm and uses an ICCD camera which leads to Lorentzian-type peak profiles. Accomplished measurements include

- determination of electron density and temperature in argon discharges at variable pressure, input power and magnetic field using the collisional-radiative model Ar-Yacora

- determination of dissociation $n(H)/n(H_2)$ in hydrogen/deuterium at variable pressure and magnetic field under the assumption that $n(H)/n(H_2)$ is directly proportional to the ratio of atomic Balmer-H_γ to molecular Fulcher-radiation

- determination of gas temperature and vibrational temperature of the molecules in hydrogen/deuterium at variable pressure and magnetic field

Electron density and temperature in hydrogen/deuterium is difficult to obtain from OES alone but can roughly be estimated from the Collisional Radiative model Yacora for atomic hydrogen.

3.2.2.2 Results

Figure 31 shows dissociation obtained from early measurements of hydrogen and deuterium plasmas in the 5 cm vessel. It shows results for the helicon setup

Figure 31: Comparison of $n(H)/n(H_2)$ in the helicon setup with ICP setups
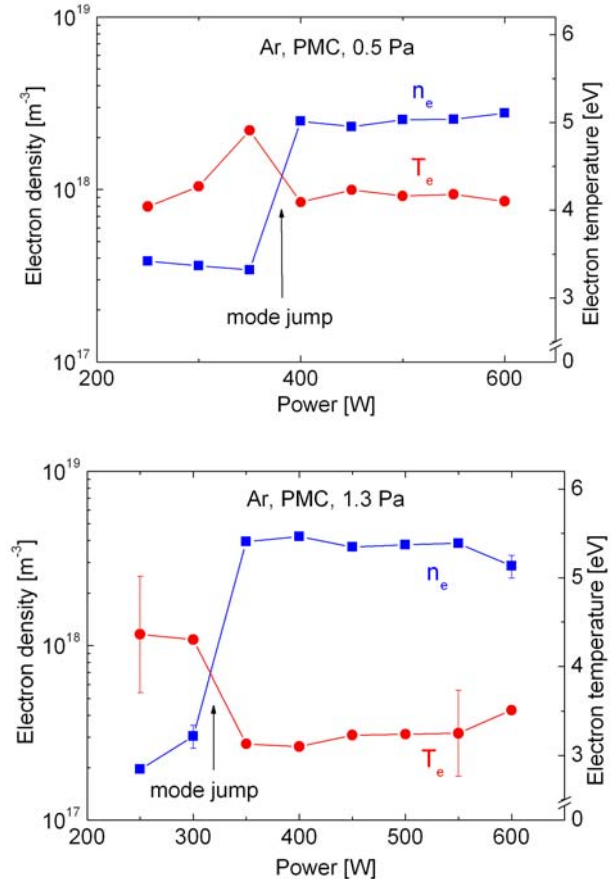
Figure 32: n_e and T_e in argon at 0.5 Pa and 1.3 Pa, respectively, and variable input power (PMC)

(PMC) compared with dissociation in an ICP setup (helicon antenna replaced by a 3-turn coil and no magnetic field) as well as dissociation in another planar ICP experiment at the University of Augsburg. The input power was kept constant at 250 W for all measurements and OES was done with an axial line of sight (in
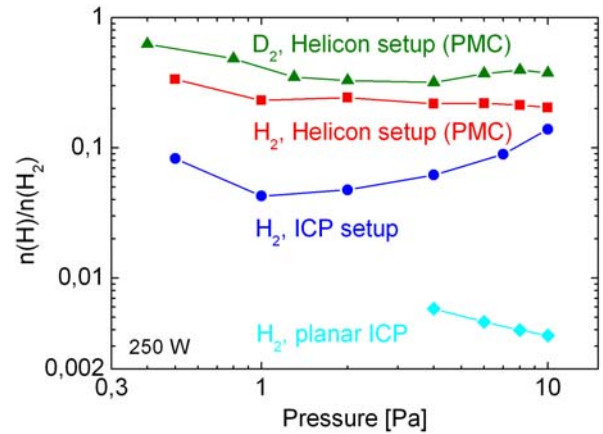
contrast to the radial line of sight under the antenna in figure 27 that was used for all other measurements presented in this report).

It is clearly evident that the helicon setup offers better performance with regard to dissociation – especially at low pressures. In the planar ICP experiment it was not possible to launch hydrogen discharges below 4 Pa at all. Possible reasons for these observations will be presented later in this report. As already observed in several experiments, deuterium discharges are much easier to generate, are much more stable and show a higher degree of dissociation and ionization than hydrogen plasmas for same power and pressure.

Figure 33: Ionization degree in argon at 400 W and variable pressure (PMC)

3.2.2.3 *Measurements in Argon*

Before going further into presenting and discussing the results obtained in hydrogen it is reasonable to look at the accomplished measurements in argon first. This is due to an overall better performance and easier handling of argon discharges in general. In fact more evidence for a helicon discharge was found in argon than in hydrogen so far. The measurements presented in this chapter were carried out in the 5 cm vessel.

In figure 32 the most prominent difference between observations in argon and hydrogen becomes clear: By varying the input power a jump in electron density of about one order of magnitude occurs in argon. It has not yet been possible to detect such a jump in plasma parameters in hydrogen. The jump in electron density is accompanied by a decrease of electron temperature. With rising pressure the transition occurs at lower input power. In general, the ionization degree n_e/n_0 is high (some percents) and increases with lower pressure (figure 33).

Although the jump appears in all configurations (PMC, HCC as well as without magnetic field) it is most distinct in the PMC where it is accompanied by an intensive blue-light of the plasma under the antenna at low pressures (< 1 Pa). This blue-light originates from Ar ion lines has only been observed with permanent magnets so far for $n_e > 10^{18}$ m^{-3} and could be an indication for the actual formation of a helicon discharge since the observation of a "blue mode" has been reported by many groups investigating helicon discharges.

If the observed "blue mode" is a helicon or not can, however, only be clarified by measuring the time dependent magnetic (wave-) field. For the moment it
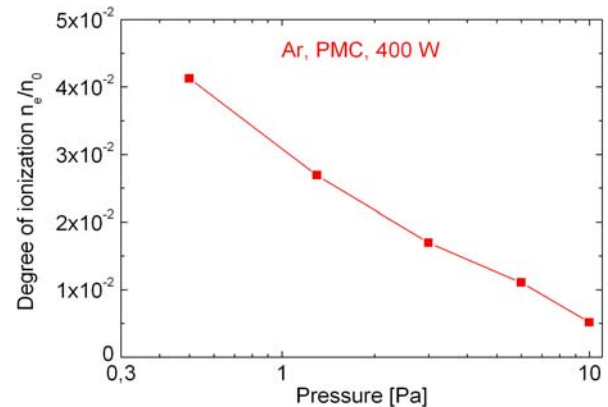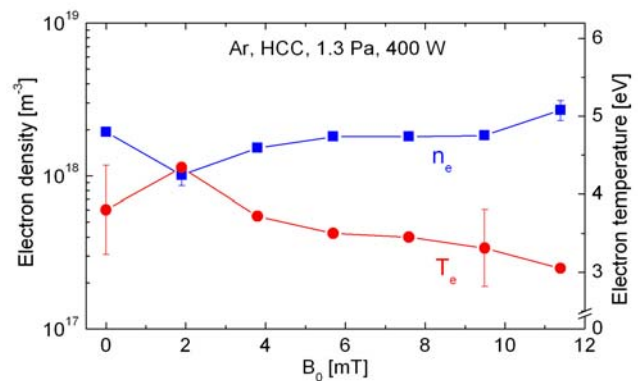

Figure 34: n_e and T_e in argon at 1.3 Pa, 400 W and variable magnetic field (HCC)

is not clear if the observed jump corresponds to a transition into the helicon mode or if it is simply the transition from E- to H-mode.

In order to further investigate the influence of the magnetic field on the plasma, a series of measurement has been carried out in the HCC. Figure 34 shows both electron density and temperature plotted against the magnetic field strength under the antenna at constant pressure and input power. As one can see, electron density slightly increases and electron temperature decreases when the magnetic field is raised. At least the increase in electron density can be explained through better confinement of the plasma by the axial magnetic field. There is however

Figure 35: Input power needed for stable operation in the "high n_e" mode in mixtures of argon and hydrogen.

no further evidence for a helicon discharge, as in the case of helicon there should be another jump in electron density when magnetic field is raised. It is possible that the magnetic field was not sufficient to show this jump.

3.2.2.4 Measurements in Mixtures of Hydrogen and Argon

Discharges in mixtures of argon and hydrogen have been generated in the 5 cm vessel (PMC) in order to determine the influence of the argon to hydrogen density ratio on the input power needed to induce the jump in electron density described in the previous chapter. The measurements were carried out at constant pressure of 1.2 Pa and constant total gas flow of 10 sccm/min. The input power was increased until the distinct jump in electron density occurred. This was always indicated by a major rise of plasma emission. Figure 35 shows a linear slope of the input power needed to observe the jump with increasing hydrogen content between 0 and 20 % of hydrogen in argon. In plasmas with higher percentages of hydrogen the electron density jump could not be induced. This is due to a change in RF matching accompanying the mode jump. When the hydrogen content is above 20 %, the forward power in the "low n_e" mode reaches its maximum of 600 W before the jump occurs.

The observations for deuterium were the same as for hydrogen. Particularly it was likewise impossible to induce the electron density jump with more than 20 % deuterium in argon. It should be emphasized that in mixtures of argon and hydrogen the jump in electron density (determined by argon emission) comes along with a considerable rise in both
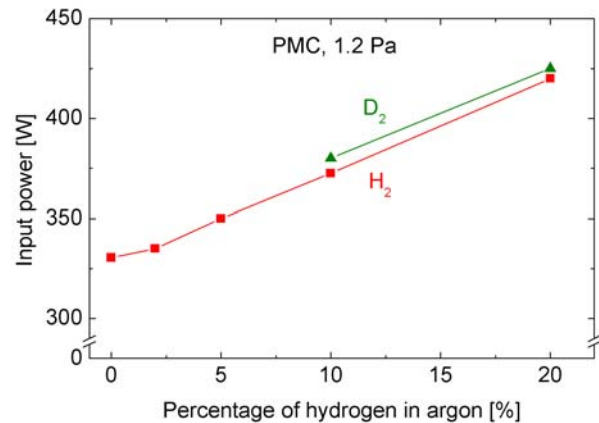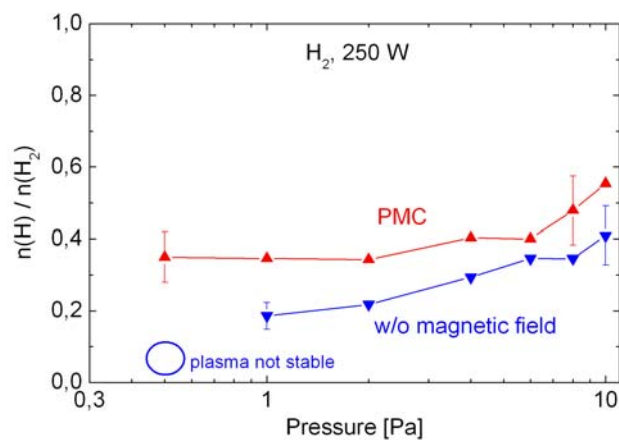

Figure 36: Degree of dissociation in hydrogen at 250 W input power and variable pressure (PMC and w/o magnetic field)
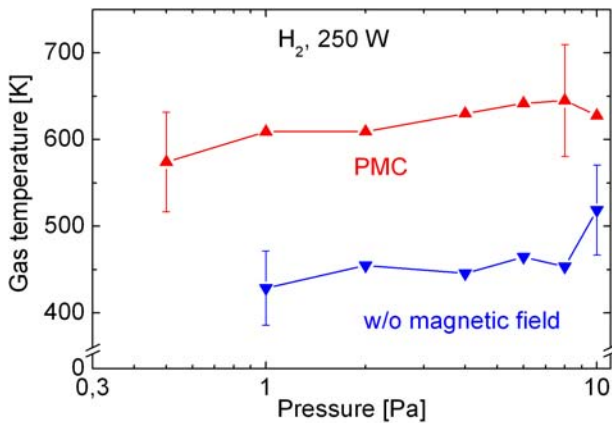
Figure 37: Gas temperature in hydrogen at 250 W input power and variable pressure (PMC and w/o magnetic field)
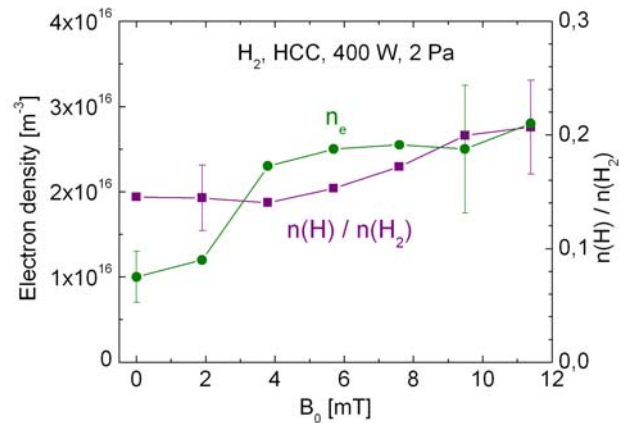
Figure 38: Electron density and dissociation in hydrogen at 400 W, 2 Pa and variable magnetic field (HCC)

dissociation $n(H)/n(H_2)$ and gas temperature of hydrogen molecules (determined by hydrogen emission). All these results indicate that it should be possible to launch the mode jump in pure hydrogen as well. To achieve this, however, more input power is needed.

3.2.2.5   Measurements in Hydrogen

Some prominent results in hydrogen/deuterium have already been presented at the beginning of this chapter (see 3.2.2.1). A higher degree of dissociation with magnetic field (PMC) compared to a standard ICP configuration without magnetic field has been observed in these axial measurements.

Analog results follow from early radial measurements in the 5 cm vessel. Figure 36 shows dissociation in a helicon setup (PMC) compared to dissociation in a setup with the helicon antenna but without any magnetic field. It is evident that dissociation goes up when a magnetic field is added. As in argon this can be explained through better confinement of the plasma in the presence of a magnetic field. The different pressure dependency of the radial measurements in comparison with the axial measurements is a consequence of changing plasma geometry.

As noted in figure 36, it was not possible in these early measurements to generate stable discharges without magnetic field below 1 Pa. This is another evidence for the increasing positive influence of the magnetic field on dissociation and plasma stability at lower pressure.

Beside its effect on dissociation, the magnetic field also influences gas temperature (see figure 37) and electron density (see figure 39). Both go up when the field is added – presumably for the same reason (better confinement) as dissociation. The degree of ionization n_e/n_0 is about 3×10^{-4} at low pressures and thus two orders of magnitude below the values for argon.

As in argon, a series of measurements have been carried out in the HCC in order to investigate the change of plasma parameters with varying magnetic field. Figure 38 early results from measurements in the 5 cm vessel with an inappropriate power supply for the Helmholtz coils which was strongly perturbed by the electromagnetic RF field and hence did only allow coarse adjustment of the magnetic field. One can see,

however, that both dissociation and electron density increase with magnetic field. Ionization is proportional to electron density in this figure and about 1×10^{-4} at the highest accessible magnetic field. In comparison with the investigations in the PMC (figure 39), there is a noticeable deviation between the measuring points at 2 Pa for the degree of dissociation.

Although the measurement in HCC was carried out at higher input power, its dissociation is about two times less the dissociation in PMC. It is still unclear why the permanent magnets provide better results in hydrogen as well as in argon ("blue mode" only in PMC) but it is presumably an effect of magnetic field geometry, namely the field reversal under the magnets.

Figure 39: Electron density in hydrogen at 250 W input power and variable pressure (PMC and w/o magnetic field)

After the installation of a new power supply for the Helmholtz coils which is not perturbed by the RF field, more detailed measurements of the influence of magnetic field on hydrogen discharges were feasible. Figure 40 shows axial measurements of dissociation in hydrogen and deuterium plasmas in the 10 cm vessel plotted against the magnetic field. Both pressure (0.6 Pa) and input power (400 W) were held constant during the measurements. In hydrogen dissociation varies only little with magnetic field and shows some sort of mode transition (hysteresis between 4 mT and 6 mT). This is presumably an effect of plasma geometry since radial measurements show a transition to a slightly lower level of dissociation when magnetic field is raised. Dissociation in deuterium is higher than in hydrogen in the accessible range of magnetic field and shows a different characteristic as well: A distinct peak of dissociation at a low magnetic field of about 3 mT is followed by a nearly linear increase of dissociation with magnetic field above 4 mT. The peak at low magnetic fields in deuterium does also appear in the 5 cm vessel and for radial measurements as well as for

other plasma parameters such as gas temperature, vibrational temperature and plasma emission (atomic as well as molecular emission). By increasing the input power the peak becomes even more pronounced.

Since a peak of electron density at low magnetic fields ("low-field peak") is reported for many rare gases helicon discharges it would be interesting if the peak observed in deuterium plasmas does also develop in electron density. Unfortunately, exact measurements of electron density were unfeasible up to now.

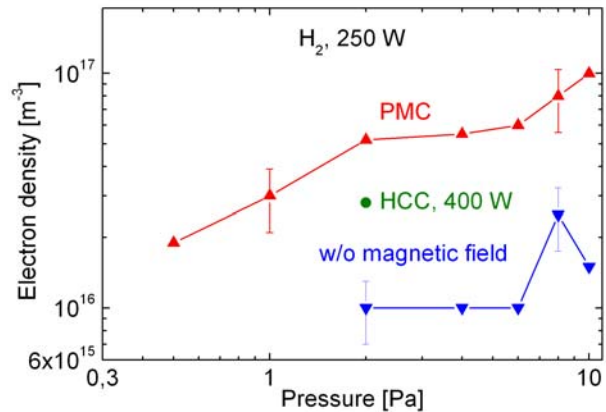In summary, a positive effect of magnetic field on dissociation and ionization in hydrogen has been dem-
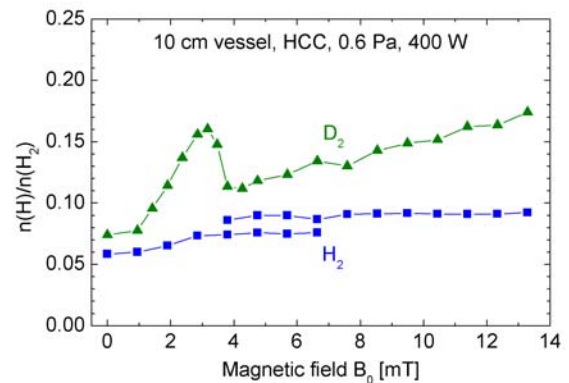

Figure 40: Dissociation in hydrogen and deuterium at 400 W, 0.6 Pa and variable magnetic field (HCC)

onstrated with the experiments carried out so far. This positive effect is most distinctive at low pressure which could be important for future ion sources. Although no evidence for a helicon discharge (no jumps, low ionization) was found in hydrogen so far, it should be emphasized that the limit of the magnetic field in HCC will be increased by adding better cooling components within the next modifications on experimental setup. Accessible input power will also be enhanced when the 2 MHz generator (max. 2 kW) will be brought on line. So there are plenty of chances to achieve even more interesting results.

3.2.3 Axial Magnetic Field Experiments at BATMAN

The dominant channel for surface production of H^- is the conversion of hydrogen atoms. However, it has been shown recently using a PIC code that the number of negative ions emitted from the plasma sheath into the plasma volume is space charge limited [see Ref. 6 and section 7.2]. Thus, it is expected that the H^- or D^- current density extracted from the ion source can be increased by increasing the positive ion flux onto the plasma grid surface at constant flux of hydrogen atoms.

The plasma density and thus the fluxes of charged particle inside the ion source can be increased by either increasing the RF power or improving the plasma confinement.

A promising method for significantly improving the plasma confinement is to generate the plasma by coupling of Helicon waves into the driver.

In parallel to the basic investigations on this technique using small scale laboratory experiments that are currently accomplished at the University of Augsburg (see section above); a dedicated experimental campaign has been performed at the IPP negative ion source prototype at BATMAN with a set of Helmholtz coils mounted around the driver, generating an axial magnetic field in this region.

Although this setup constitutes no Helicon configuration, a significant influence of the additional magnetic field on the plasma confinement in the driver region as well as on the plasma density and the fluxes of charged particles in the whole ion source are expected. A schematic overview of the driver region and the Helmholtz coils is given in figure 41.

Measurements were performed for the ion source being non-cesiated and cesiated, i.e. negative ion production predominantly by volume production and surface production, respectively. Since in the first case the negative hydrogen ion density in the ion source is low, the influence of the additional magnetic field on the plasma parameters (electron density, positive ion density) can be investigated. The latter case, with high negative ion density, reveals the influence of the additional field on the transport and extraction of the negative hydrogen ions.

This section describes the observed effect of the additional magnetic field on the plasma parameters and the current
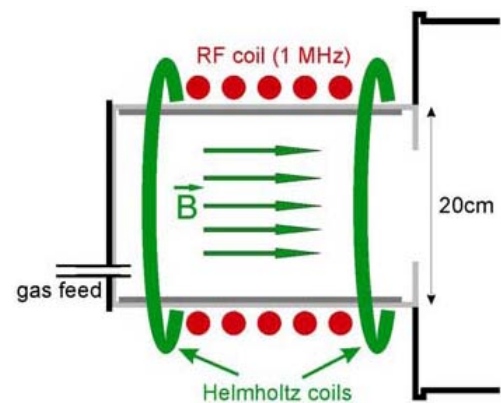

Figure 41: Schematic overview of the Helmholtz coils placed at the driver.

densities extracted from the ion source. Beam and plasma parameters were measured using the calorimeter, optical emission spectroscopy and Langmuir probes.

3.2.3.1 Experimental Setup

Experiments were performed with hydrogen plasmas, without and with cesium seeding. In the first case, negative ions are mainly formed by the volume process (dissociative attachment of electrons to highly vibrationally excited hydrogen molecules), in the second case by the surface process (conversion of hydrogen atoms and protons on surfaces with a low work function). In volume produc-
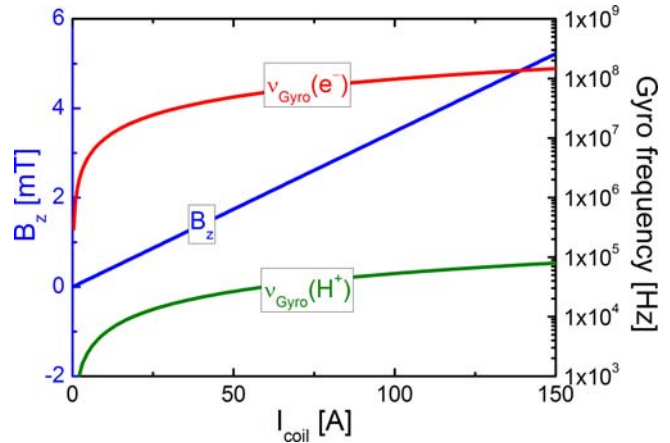

Figure 42: Axial component of the magnetic field in the center of the driver region generated by the Helmholtz coils and the corresponding gyro frequencies for electrons and protons in the driver.

tion the resulting negative ion currents are usually by an order of magnitude smaller than in surface production; the co-extracted electron current is larger by around an order of magnitude. The experiments were conducted at a pressure of 0.65 Pa (volume production) and 0.42 Pa (surface production); in both cases the RF power was 55 kW. The source was run at a higher pressure when no Cs was seeded in order to limit the power load due to co-extracted electrons on the extraction grid.

The Helmholtz coils (d=20 cm, 3×2 windings per column) were attached around the two ends of the driver cylinder to generate a magnetic field inside the driver with homogeneous axial component (directed towards the plasma grid). Figure 42 shows the dependence of the axial field strength component in the center of the driver on the current flowing through the coils (I_{coil}), calculated using the 2d code QuickField [2].

The general influence of the magnetic field on the plasma species was roughly estimated by comparing the gyro frequency (28 MHz for electrons, 15 kHz for protons at 1 mT field strength) with the collision frequency ($\approx$7 MHz for electrons and protons at the plasma parameters inside the driver region). Particles are magnetized if the gyro frequency is larger than the collision frequency. Due to their low mass, this is the case for electrons even at low field strengths while the protons (and consequently also the heavier H_2^+ and H_3^+ ions) are not magnetized even for the strongest applied additional magnetic field. However, the positive ions will feel the ambipolar force caused by the magnetized electrons attached to the magnetic field lines. Thus, it is expected that the additional axial magnetic field improves on the one hand the plasma confinement and on the other hand the plasma transport from the driver to the expansion volume.

The main question is: how does the improved plasma confinement and transport affect the plasma parameters in the expansion region and what is the influence of this change on the production and transport of negative ions in the ion source?

3.2.3.2   Results

3.2.3.2.1   Extracted Currents

Measurements were performed for coil currents from -100 A to 100 A, resulting in absolute values of the axial field strength between 0 and 3.5 mT.

Figure 43 shows the density of the extracted ion current and the co-extracted electron current. In the non-cesiated source, the electron to ion current ratio is high — about 5 — while in the cesiated source this value is significantly decreased to values around one.
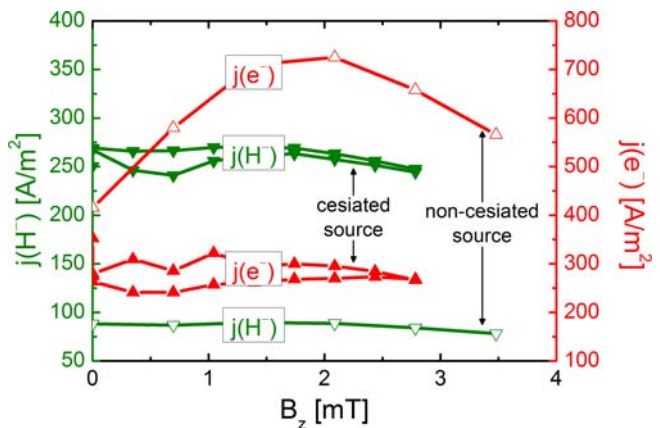

Figure 43: Dependency of extracted ion and co-extracted electron current density on the axial magnetic field in the driver for a cesiated and a non-cesiated source..

A clear influence of the axial magnetic field can be only seen for the electron current density in the non-cesiated source: a local minimum exists for no axial magnetic field and a maximum at $B_z \approx 2$ mT; for higher absolute values of the field strength the electron current density decreases. In contrast, the ion current in the non-cesiated source as well as the electron and ion currents in the cesiated source show only a very weak dependence on the axial magnetic field in the driver.

The observed characteristics indicate a similar dependence of the electron and negative ion densities close to the extraction system inside the ion source on the additional magnetic field. Further investigations regarding the plasma parameters in this region have been performed using optical emission spectroscopy and Langmuir probes.

3.2.3.2.2   Optical Emission Spectroscopy

Spectroscopic measurements were performed by means of two survey spectrometers which observe the complete visible range (λ=200-870 nm) with low spectral resolution ($\Delta\lambda$=1.5 nm). The positions of both LOS are indicated in figure 44.

The first spectrometer was attached to the line of sight (LOS) through the center of the driver volume perpendicular to the plasma grid (ZC1). Because the emission originating from the plasma volume close to the grid
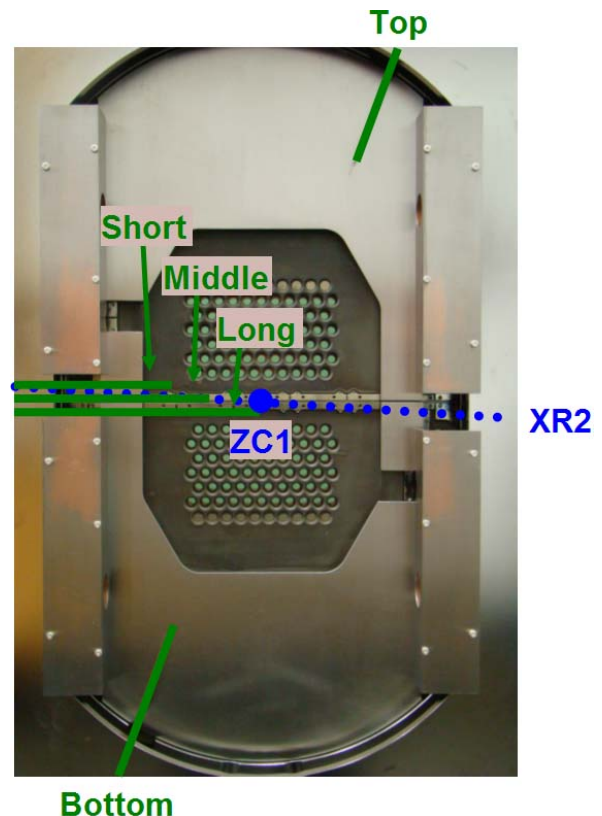

Figure 44: View from the driver onto the plasma grid of the type 6.1 ion source attached to the BATMAN test bed. Indicated are the two lines of sight used for OES (in blue) as well as the position of the five pin probes (in green).

is much less intense than the light emission from the driver, this LOS can be used to detect the plasma parameters in the driver volume. The second spectrometer was attached to a LOS parallel to the grid, at 2 cm distance (XR2) and thus overlooks the boundary layer close to the plasma grid surface which is relevant for the transport of the surface produced negative ions from their point of birth to the extraction apertures.

Results of the measurements in volume production of negative ions are shown in figure 45 and figure 46 for the driver and the extraction region, respectively. Both figures show the absolute emissivity ε of the Balmer line H_β and the line ratios

Figure 45: Absolute emissivity ε of the Balmer line H_β; line ratios H_α/H_β and H_α/H_β measured in volume production in the driver.

H_α/H_β and H_β/H_γ. For both LOS the dependency of emissivities and line ratios on the strength of the additional magnetic field are perfectly symmetric for positive and negative magnetic field values and thus just the results for positive axial magnetic field are shown here. The results shown have been measured during the RF phase of the discharge after the end of the extraction. Unless specifically mentioned, these results are identical to the results of measurements during the extraction.

The Balmer line emission in the driver is almost constant at low magnetic field strength. For larger field strengths an exponential decrease takes place: the emissivity at 3.5 mT is approximately by a factor three smaller than with no magnetic field.

The measured line ratios show almost no dependency on the magnetic field: while H_α/H_β is constant, H_β/H_γ decreases slightly with increasing field strength. Using results calculated by a collisional radiative

model and assuming high electron temperatures ($T_e>7$ eV, which is the case in the driver volume) it can be determined from the H_α/H_β that the electron density is between 2.0×10^{18} m^{-3} (B_z=0 mT) and 1.7×10^{18} m^{-3} (B_z=3.5 mT). The dominant excitation process is the direct excitation from the ground state of the hydrogen atom. It needs to be noted that these values of the electron density are averaged over the plasma volume along the used LOS, i.e. the centre axis of the driver. Possible effects of the additional magnetic field on the radial profile of the electron density in the driver can not be determined using the available OES setup.
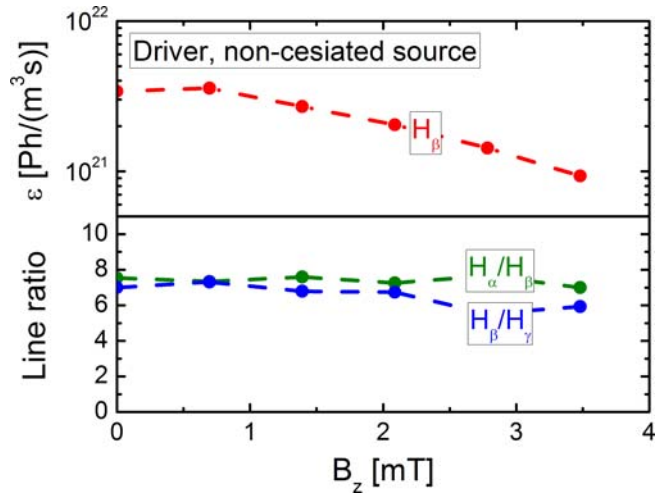

Figure 46: Absolute emissivity ε and line ratios of the Balmer lines measured in volume production in the boundary layer close to the plasma grid.

A different behavior than that in the driver is seen in the extraction region, as shown in figure 46: the emissivities show a local minimum with no additional axial magnetic field. With increasing magnetic field the radiation increases up to a maximum at $B_z \approx 1.5$ mT and then decreases for larger field strengths.

The ratio H_β/H_γ is almost unaffected by the magnetic field. The determination of n_e requires knowledge of T_e since for low temperatures this line ratio depends on both the density and temperature. Using T_e=1 eV (measured by the Langmuir probes) an electron density of between 5×10^{17} m^{-3} (for B_z=1.4 mT) and 2.5×10^{17} m^{-3} (for B_z=3.5 mT) results
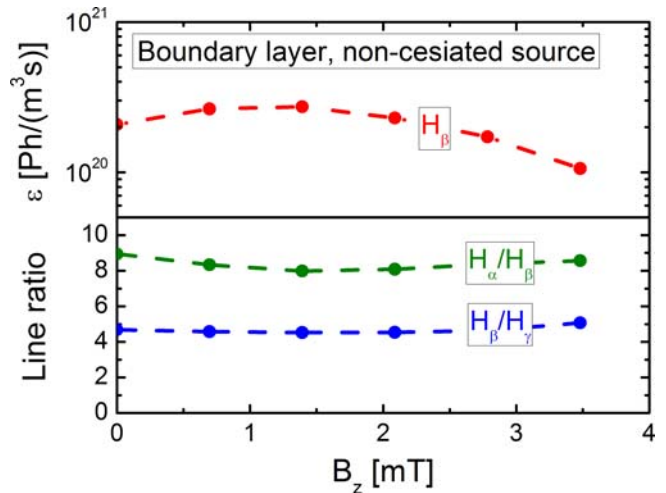

Figure 47: Absolute emissivity ε and line ratios of the Balmer lines measured in surface production in the boundary layer close to the plasma grid.

in a very good agreement of measured and calculated absolute emissivities of H_β and H_γ as well as the corresponding line ratio. The dominant excitation process is dissociation and dissociative recombination of the molecular ion H_2^+.

In contrast to H_β/H_γ, the ratio H_α/H_β shows a weak dependency on the magnetic field and a maximum for B_z=0. This shape can be explained by the influence of negative hydrogen ions present in the volume close to the plasma grid on the H_α radiation: mutual neutralization of H^- with H^+ results in atoms in the ground state and exited atoms. In the relevant energy range the latter are predominately excited to the level n=3, i.e. the upper level of the H_α transition. In addition, H_α/H_β is slightly depleted during the extraction process, being in accordance with the influence of negative hydrogen ions on H_α described above.

Due to a low cesium density in the driver region, the influence of source cesiation on the plasma parameters in this plasma volume is low. Thus, the comparison of results in volume production and surface production is made for the extraction region only. In comparison to figure 46 (non-cesiated source), the absolute Balmer line emissivities and line ratios measured in the extraction region of the cesiated source are shown in figure 47. The line emissivities are by a factor of between 6.5 and 9.5 smaller than in volume production. This effect can be explained on the one hand by the lower pressure and the corresponding lower neutral particle density in the ion source during the surface op-
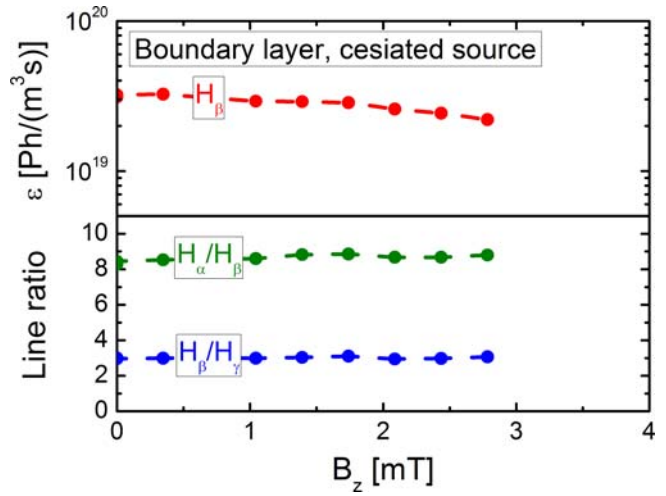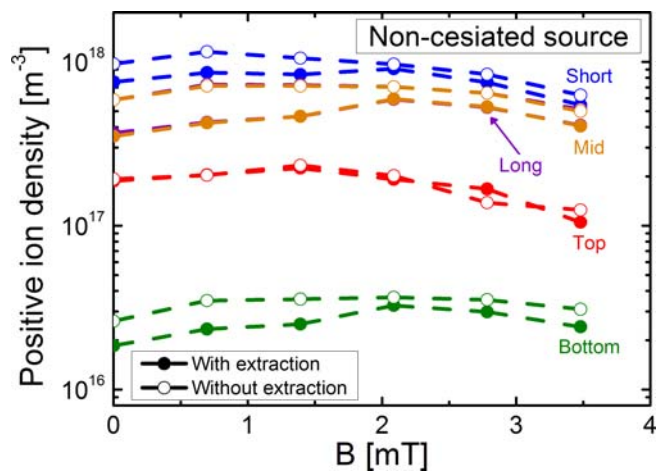

Figure 48: Positive ion density obtained for the pin probes with and without extraction for a non-cesiated ion source.

eration experimental campaign. On the other hand, a change of the plasma parameters is observed: the measured line ratio H_β/H_γ is decreased by a factor of around 1.5 by the cesiation of the ion source, while H_α/H_β stays constant. Under the assumption that the electron temperature (T_e=1 eV) is not affected by cesium, the measured H_β/H_γ ratio corresponds to a decreased electron density. Although it is difficult to match measurement and model under these condi-tions, an electron density of around 10^{17} m^{-3} is ob-tained (compared to 2.5×10^{17} to 5×10^{17} m^{-3} in pure volume operation of the ion source).

Figure 49: Comparison of top and bottom Langmuir probe measurements.

The lower electron density would result, in principle, also in a decreased H_α/H_β ratio. The reason for the stability of this line ratio is a strong increase of the negative hydrogen ion density (not estimable in the non-cesiated source, in the range of 5×10^{16} m^{-3} to 1×10^{17} m^{-3} in the cesiated source).

The dependence of the electron density in the boundary layer on the additional axial magnetic field determined by the optical emission spectroscopy for the non-cesiated ion as well as for the cesiated source is in good qualitative agreement with the shape of the corresponding co-extracted electron current densities shown in figure 43.

3.2.3.2.3 Pin Probes

During this campaign five uncompensated pin probes were used. Three of them are placed at the po-sitions x = -10, -5 and 0 cm (referred as short, middle and long probe respectively), 0 cm being the center of the plasma grid and -15 cm being the flange edge. The distance between the three probes and the surface of the plasma grid varies between two and three cm. Moreover, they are aligned along the LOS used by the OES which is parallel to the grid. Additionally, two probes (top, bottom) were installed in the left bottom and right top corner, at 1 cm distance from the bias grid. The position of all probes is also indicated in figure 44.

Figure 48 represents the measured densities of positive ions, determined by evaluation of the ion saturation branch of the probe characteristics, without Cs seeding. For all probes, the behavior of the ion density with the additional magnetic field strength is the same as obtained with OES in the extraction region (see figure 46). Each probe shows a small increase in the ion density followed by a decrease as magnetic field strength increase.

The highest positive ion densities are found vertically at the centre of the plasma grid (long, middle and short probes). Compared to these values, the densities measured in the top and bottom of the source are lower by a factor of around five and 50, respectively. However, since the top and bottom probes are dis-posed symmetrically (with respect to the center and edge of the plasma grid) no significant difference be-tween top and bottom measurements should be found in the case of homogeneous plasma. Hence, this re-
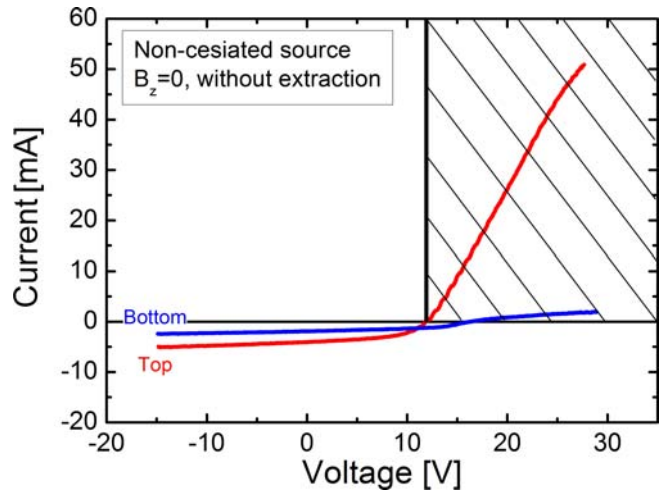
sult indicates a plasma drift, caused by the magnetic filter field, in agreement with previous measurements using other diagnostic techniques (e.g. optical emission spectroscopy).

The probe IV curves measured by the top and bottom pin probe are compared in figure 49. Especially the IV curve of the bottom probe shows a non-classical Langmuir probe characteristic; the evaluation of the plasma parameter is rather difficult as the classical Langmuir probe theory cannot be applied, a reliable probe theory including a large fraction of negative hydrogen ions and magnetic fields is not available up to now. The non-classical IV characteris-

Figure 50: Influence of extraction on the bottom Langmuir probe characteristic.

tic seems to be associated with the difference of the bias potential of the plasma grid and the local plasma potential: During the measurements in the non-cesiated source Φ_{bias}-Φ_{plasma} was around 6–7 V. Probe characteristics taken during campaigns with Φ_{bias}-Φ_{plasma} < 0 show a classical electron branch. Due to the lack of the theory, only the ion branch was used to determine parameters. However, the electron branch can still give the trend of evolution. The absolute value of the ion saturation current measured in the top is significantly higher than in the bottom. In an equivalent manner the bottom electron branch is almost negligible with respect to top electron branch. Consequently, very low density plasma is situated in the bottom of the ion source.
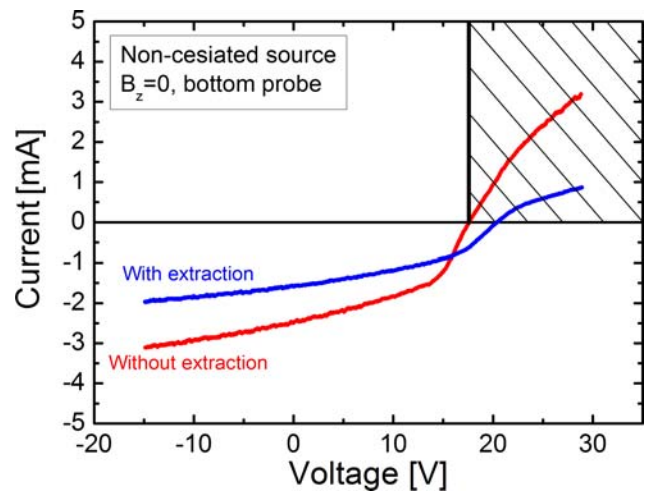
The results of the long, middle and short probes give an idea of the radial plasma behavior, from the middle to the edge of the plasma grid. The short pin probe data evaluation is difficult due to the neighborhood of the strong magnetic filter field. Hence, as discussed already above, the results provided by the short probe should be taken carefully. However it can be seen that from long to middle, the ion density remains almost identical.

Figure 48 also exhibits the influence of extraction on densities: while the positive ion density measured by the long, middle, short and long probes stays constant, the results of the bottom probe is significantly decreased by the extraction. The effect of extraction is highlighted in figure 50 showing the IV characteristics for the bottom probe with and without extraction. An interesting effect can be seen: extraction tends to change the probe characteristic. Since the negative ion mass is significantly higher than the electron mass, the relative influence of extraction on electrons is higher than on
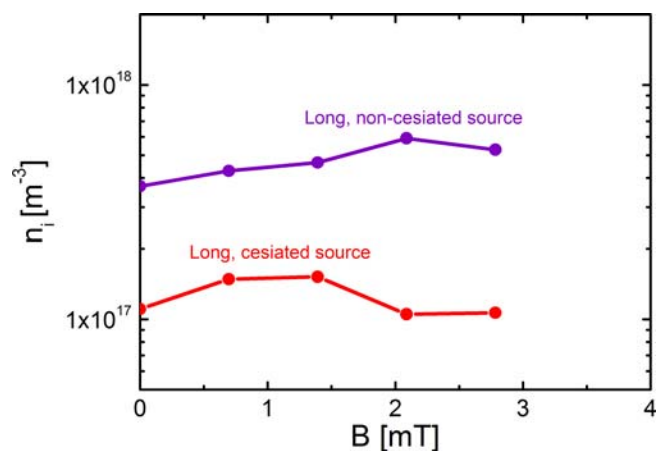

Figure 51: Ion density obtained for the long probe with and w/o Cs for different axial magnetic fields in the driver.

negative ions. Electron depletion caused by the extraction could leave a plasma almost uniquely composed of H_x^+ (x = 1…3) and H^- ions. The observed symmetry in probe characteristics could be due to such an effect, however, further investigations are needed to conclude.

Figure 51 compares the positive ion densities obtained by the long probe with and without Cs seeding. It can be seen that in both cases changing the axial magnetic field strength in the driver poorly affects the ion density. This behavior is in good agreement with the spectroscopic results described above and the variation of extracted negative ions with the magnetic field in the driver. Moreover, a

Figure 52: Langmuir probe characteristics measured in a cesiated source.

reduction of the ion density compared to Cs free measurements is observed. This is due to the fact that the source was run with a lower pressure when Cs was seeded.
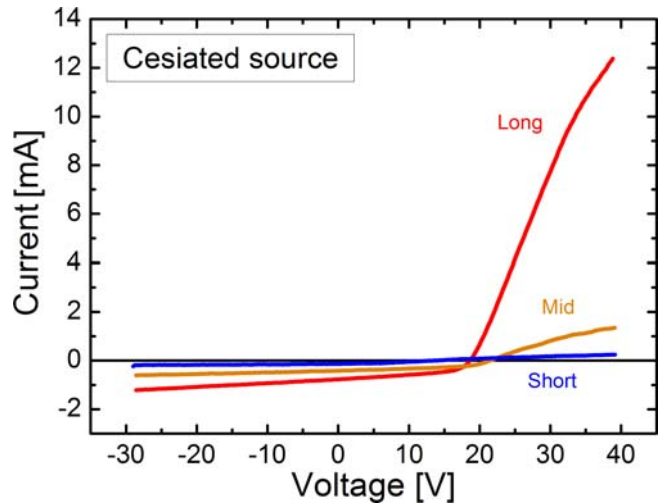
It was not possible to analyze middle and short probe characteristics (see also the discussion above) since the currents drawn by these two probes were too low and thus the curve shape was not as it can be expected from a classical Langmuir probe, as can be see on figure 52. The latter compares the three pin probes characteristics simultaneously recorded. However, it appears from figure 52 that the plasma properties between the edge (short probe), the first quarter (middle probe), and the middle of the plasma grid (long probe) change when Cs is added. Indeed, results from figure 48 (without Cs seeding) showed no difference between ion densities obtained with long and middle probe. However, figure 52 (with Cs seeding) suggests that a density gradient now exists between these two probes.

The magnetic filter field plays a key role, since the three curves characteristics are very similar when measurements are performed without filter field (with and without Cs seeding). Top and bottom probes were used, when Cs was seeded, only to record the ion saturation current. These two probes still show a strong difference in the collected ion saturation current, indicating that the previously described density gradient between the top part of the plasma grid and the bottom part of it is still present (not shown here).

3.2.3.3 Conclusion

In the non-cesiated source investigations on the dependence of the plasma parameters (electron density, positive ion density) on the additional axial magnetic field in the driver were performed: an influence of the magnetic field on the co-extracted electron current density was clearly seen: for $B_z<2.1$ mT the electron currents increase with the magnetic field and decreases for stronger field strength. The electron densities in the boundary layer determined from the spectroscopy of Balmer lines as well as the positive ion density determined using the saturation current of the pin probes show a very similar dependence on the axial field. The negative hydrogen ion current is independent of the additional magnetic strength. Due to improved con-

finement caused by the additional axial magnetic field the electrons are removed more efficiently from the driver to the expansion region. More electrons directly implicate an increase of the co-extracted current density. On the other hand the probability for dissociative attachment (which is responsible for the production of negative ions in volume operation) as well as the probability for electron stripping is increased. The combination of increased production and destruction probabilities for negative hydrogen ions results in a constant extracted current density. Due to the ambipolar force the density of protons in the expansion region increases also; this explains the shape of the probe signals.

The decrease of all signals for B_z>2.1 mT can not be explained yet: it has to be remarked that in this range the quality of the RF circuit matching (cos φ) slightly decreases with increasing (from $\approx$0.82 at 0 mT to $\approx$0.66 at 3.48 mT) but at a first glance it seems that this decrease is to small to explain the observations.

The measurements in the cesiated source reveal the influence of the plasma parameters determined in the non-cesiated source on the production of negative hydrogen ions at the surface of the plasma grid and their transport towards the extraction apertures. In combination with the magnetic filter field which divides the expansion region from the extraction region a broad (several cm) boundary layer forms close to the plasma grid in which a high negative in density pushes back the electrons from the plasma grid and the extraction apertures. This boundary layer may be the explanation why in the cesiated source the improved transport of electrons from the driver to the expansion region does not result in a significant increase in the co-extracted electron current. The dependence of the additional axial magnetic field on the positive ion density measured using the pin probes is very weak; this weak dependence explains why the extracted ion current density in the cesiated source shows almost no dependency on the axial magnetic field.

In conclusion, an influence of the magnetic field generated by the Helmholtz coils on the plasma parameters can clearly be seen. These changes of the plasma parameters, however, are not sufficient to change the extracted negative hydrogen ion current density significantly, especially in a cesiated source.

3.3   Influence of Source Temperature on Performance

For the ITER heating beams a reduction of the source body temperature is desirable as it eases the tempering systems in the HV deck. As the overall inlet temperature is 35 °C, source body operation at this temperature removes the necessity of installing a second heating circuit at HV (the first one is the heating circuit of the plasma grid). However, the IPP prototype source was operated in the past at source body temperatures in the range of 40 - 50 °C. From the performance point of view, a reduction of the source body temperature was not expected to be
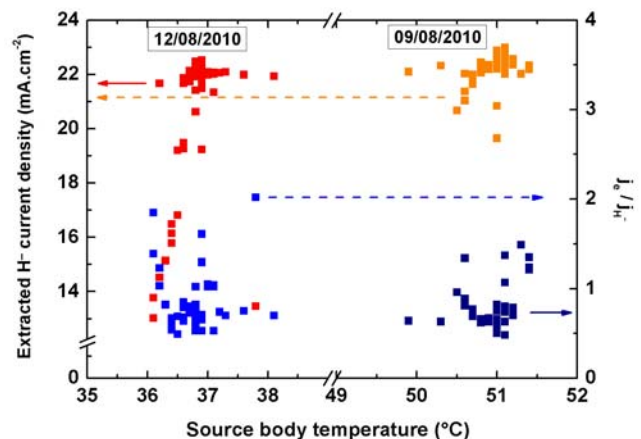
Figure 53: Influence of the source body temperature on the extracted negative ion current density and electron to ion ratio

problematic as the very first good results have been obtained with a cold source (at 20 °C), but the stability of operation as well as the conditioning times improved quite substantially for hot source body operation. Two dedicated tests at BATMAN have been performed:

- reduction of the source temperature for a source that was conditioned at 50 °C, and

- conditioning of a cleaned source at 35 °C.

Figure 53 shows the result of reducing the source body temperature for a preconditioned source. The source was already conditioned (at a 50 °C body wall temperature) when the body walls temperature was set during one operation day to

Figure 54: Source performance achieved the first day of conditioning with a body source temperature of 35 °C.

37 °C (12/08/2010). As expected from the above mentioned experience, no significant difference appears between the extracted negative ion density and electron to ion ratio when compared to operation at 50 °C. It is well known that it takes a few shots to recover the source performance achieved the previous day, most probably caused by a deterioration of the Cs layer over night by background impurities. This can be seen with the low extracted current densities (the 12/08/2010, between 13 and 17 mA.cm^{-2}) that were obtained at the beginning of the operations this particular day.

Figure 54 shows the extracted ion current density and electron to negative ion ratio achieved at the first day of conditioning with a body source temperature set to 35 °C. It appears that a current density of 27 mA/cm^2 is rapidly achieved, while the amount of co-extracted decreases down to 0.3. This conditioning to full performance is even faster as when the body source temperature is set to 45 deg. Furthermore, the amount of Cs needed for full performance was much lower than previously. The most probable reason for this promising behavior is that before the start of operation almost all small (and big) leaks have identified and removed, resulting in a background pressure of 5-8x10^{-7} mbar only. This is much lower than the usual base pressure in the past (1-3x10^{-6} mbar). The following days (not shown here) shows a slightly increased extracted negative ion current, while the electron to ion ratio remains around 0.3-0.5. No deterioration of the Cs oven performance, i.e. the need of increasing the oven temperature for the same flow rate, was observed.

These results show that the conditioning and the Cs consumption is not a question of the source temperature (when it is above the melting temperature of Cs), but a question of the vacuum conditions. This agrees with the observation at MANITU that the daily re-conditioning of the source is much faster when the source gate valve was closed during the cryo regeneration.
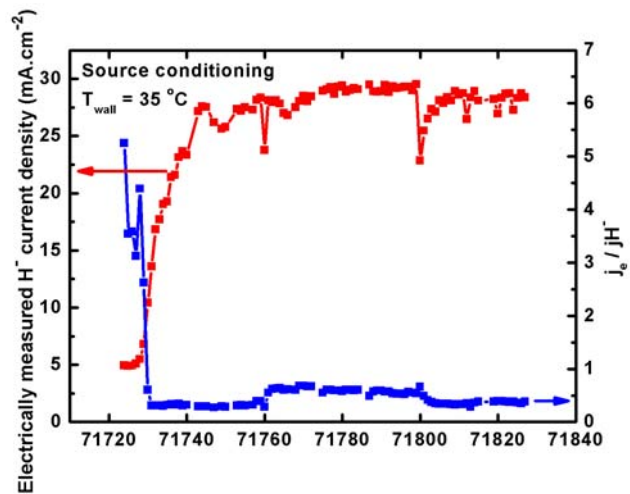
3.4 Future Plans

Although the first experimental campaigns regarding the magnetic filter field showed very interesting results, the experiments are not finished and will be continued.

Following experiments are on the agenda:

- continue the experiments with deuterium;

- measure axial plasma profiles with the movable Langmuir probes, one at top and one at bottom, in dependence on the magnetic filter field;

- experiments with more sophisticated magnetic filter fields, e.g. try to generate a combination of 3 mT at the plasma grid and a *Bdz* of 1250 Gcm simultaneously in hydrogen;

Further experiments with the Helmholtz coils at BATMAN are planned, accompanying the magnetic filter field experiments; the final aim is to apply the Helicon plasma generator being in development at the University of Augsburg to the IPP negative ion source prototype.

The next experiments planned at the University of Augsburg will focus on the observed "blue mode" in argon and the question, why such a transition did not occur in hydrogen thus far. Systematical measurements of argon-hydrogen mixtures and in Deuterium — here the results are expected to be much more pronounced — will be carried out in order to obtain the ratio threshold up to which the electron density jump occurs. Maybe these experiments will also bring further insight to the understanding of the better performance of the permanent magnets.

The next big step will be the transfer of the experiment to "stage 2" (see strategy, figure 26). This will include implementation of the new 2 MHz generator as well as usage of larger plasma vessels and other antenna types.

Also common experiments with RFX Padua are still planned, as part of the contract F4E-2009-GRT-032; these include tests of the fixed planar Langmuir probes foreseen in SPIDER.

4   Experiments at MANITU (WBS 2.2)

The experiments at MANITU concentrated on the achievement of the ITER requirements during long pulse operation at low pressure both for hydrogen and deuterium. To achieve the required long pulse reliability at high power several parts of the source design have been improved. The last remaining copper surfaces on the source back plate were coated with Molybdenum. This prevents the degradation of the Cesium layer on the plasma grid by copper, which is sputtered by backstreaming ions, and leads to more stable ion and electron currents in long pulses. Beam and plasma homogeneity were measured and the dependence on variations of the magnetic filter field was investigated. The pumping speed and capacity of the cryo pumps have been measured in collaboration with KIT, Karlsruhe.

4.1   Hardware & Diagnostic Upgrades

4.1.1   Coil Insulation

High power operation was hampered in the past by RF break down at the coil. Hence, the RF insulation of the antennal was improved by casing it in a SF_6 filled fiber glass containment (see figure 55). Reliable operation is now possible on a high power level >100 kW without destruction of the coil - a necessary condition to focus the experiments on high power operation in long pulses.
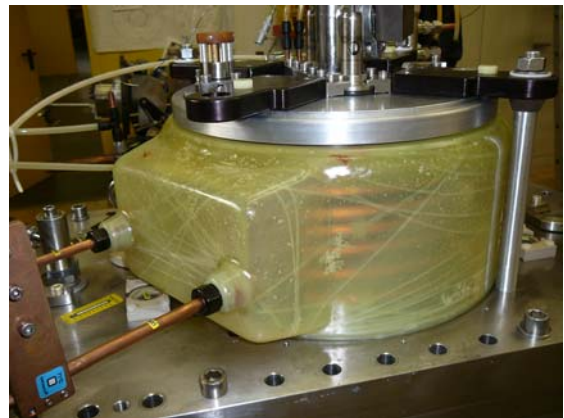
4.1.2   Faraday Screen with z-shaped Slits

At the IPP RF prototype source, the inner part of the driver, i.e. the quartz or alumina cylinder is protected against erosion by a Faraday screen. In order to couple the

Figure 55: Insulation containment of the RF coil at MANITU.

RF power to the plasma, slits in the Faraday screen are necessary. In the past (and also still at BATMAN) these slits were open, i.e. there is a direct line-of-sight from the plasma to the insulator. Hence, the insulator will be heated by the direct contact with the plasma. This is not critical for BATMAN for short pulses, but might be a problem for long pulse operation, especially when the driver is operated in vacuum, as it is foreseen in ITER/SPIDER/MITICA and also for ELISE, as in this case the insulator is not cooled at all.

Hence, a Faraday screen with z-shaped slits (see figure 56) was built as a proto type for ELISE and for the ITER ion source. With that design, the quartz insulating container has no contact with the driver plasma. Hence, the z-shaped slotted Faraday screen is of advantage for long pulse due to the lower cooling requirements of the insulator.

Such a z-shaped slotted Faraday screen was installed from October 2008 to June 2009 in MANITU for initial tests. In this period, the diagnostics for the measurement of the driver RF efficiency, i.e. the light emission out of the driver and the water calorimetry of the Faraday screen was improved and are now reliably
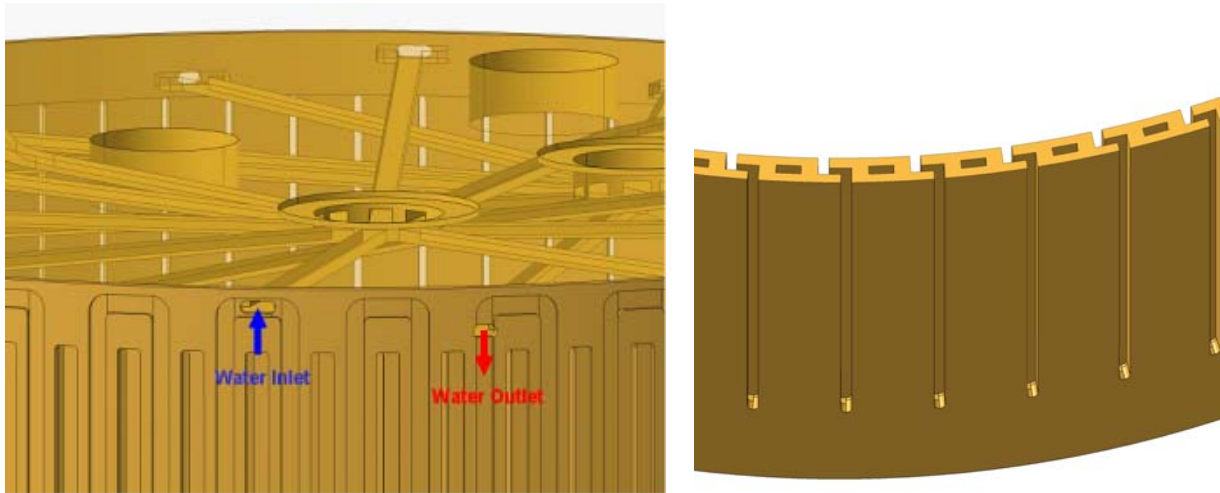
Figure 56: Faraday screen, cooling loops (left) and "z-shaped" slits (right)

operational. Hence, the normally slotted Faraday screen was installed again during the maintenance phase in June/July 2009 (see above) for a robust comparison of the driver efficiency of both driver concepts.

4.1.2.1 Water Calorimetry of the Faraday Screen

At MANITU, the Faraday Screen is cooled and tempered by two different water circuits due to the limits of the available cooling systems and the cooling / tempering requirements of the Faraday screens. The switching between both cooling systems is done automatically by the control system.

Between the pulses the Faraday screen is heated by the LAUDA system to temperatures of 40 - 50 °C — according to the source body temperature — in order to avoid cold spots and possible accumulation of cesium. The LAUDA system, however, has not enough cooling power for the cooling of the Faraday screen during long pulse operation, hence the Faraday screen is cooled during the RF phase by the so-called 'High pressure' cooling system. This system provides a water flow approximately three times larger than the LAUDA system, the water, however, cannot be heated, so that system cannot be used between the pulses.

Figure 57 shows as an example the temporal evolution of the inlet and outlet water temperatures of the Faraday screen. Before the start of the pulse (at about 2 s) inlet and outlet water have the same temperature, corresponding to the LAUDA temperature. Shortly before the start of the pulse (1 s) the cooling system is switched to the high pressure system. The 'overshoot' of the outlet temperature is not caused by the gas puff, because it is much too long; the reason is not quite well understood, but is most probably due to the fact that the switching of the cooling systems is too late, so that the Faraday screen is insufficiently cooled for the first seconds of the RF pulse. For the calorimetry, however, this transient behavior is not important, as for the evaluation of the power that is received by the Faraday screen the temperature difference of inlet and outlet water in the stationary phase is used.

This switching of the cooling systems at MANITU requires therefore an absolute measurement of the inlet and the outlet water temperature, as no correction of the temperature signals before the pulse can be performed. Such an absolute temperature measurement with the needed precision of less than 1 K is not

possible with the Ni-CrNi thermocouples that have been used at all IPP test facilities up to now. Furthermore, the signals of these thermocouples are rather noisy due to problems with RF pick-up. Hence, a reliable measurement of the power load of the Faraday screen was not possible.

The temperature measurements have been drastically improved by using silicon spreading resistance temperature sensors ('KTY19'). Signals of these sensors are already shown in figure 57. The signals are robust; no RF noise can be seen. In contrast to the thermocouple signals, the temperatures of inlet and outlet water during the LAUDA cooling phase are identical.

Figure 57 shows also already the comparison of the water temperatures for both geometries of the Faraday screen for otherwise identical pulses. As can be seen, the difference of outlet and inlet temperature is larger for the z-slotted Faraday screen, i.e. the power load is larger compared to the normally slotted Faraday screen. This power load P can now be easily calculated from the temperature difference ΔT by

$$P = c \times dm/dt \times \Delta T,$$

c being the heat capacity of water and dm/dt the mass flow. The measurement of the water flow in the high pressure cooling system is still to noisy, so that for both Faraday screen types a (identical) value is used that was measured during a pulse without RF.

Figure 58 shows as main result the amount of RF power that is received by the Faraday screen for both types. As already seen in figure 57, the z-shaped slotted Faraday screen receives more power than the normally slotted Faraday screen. The numbers vary between 45 and 55% for the normally slotted Faraday screen — with an average value of 50%, and between 50 und 60% the z-shaped slotted Faraday screen — with an average of 55%, respectively. The reasons for that variation might be inaccuracies of the measurements of hidden parameters; as an example, figure 59 shows that the relative power load of the Faraday screen does not depend on the RF power itself.
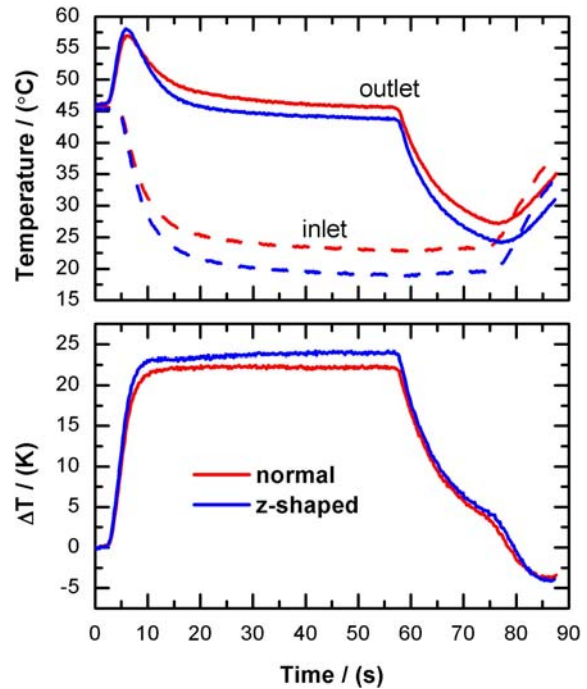

Figure 57: Top: Temporal evolution of the inlet and outlet water temperatures of the normal shaped and the z-shaped slotted Faraday screen. Bottom: Temperature difference. Both pulses have 60 kW, 0.37 Pa, 50 s.
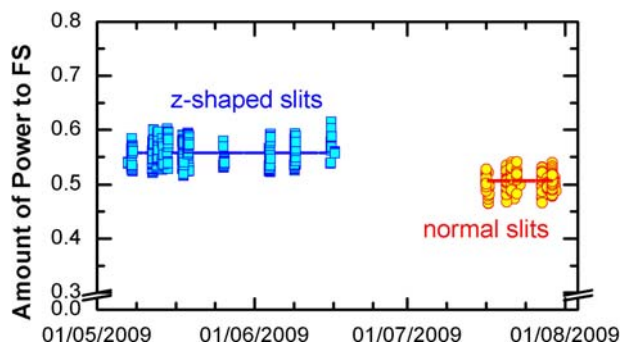

Figure 58: Amount of RF power received by the Faraday screen for the experimental campaigns May/June 09 (z-shaped slotted FS) und July 09 (normally slotted FS).

These measurements show that the z-shaped slotted Faraday screen receives about 5% more power as the normally slotted Faraday screen. This difference, however, was expected, as the area having contact with the plasma of the z-shaped slotted Faraday screen is larger by 5%. This shows also that the power load of the insulator in the case of the normally slotted Faraday screen is about 5% of the RF power. Furthermore, the agreement between the increase of the plasma contact area and the increase of the power load indicates that the plasma contact of the Faraday screen is rather homogeneous and that eddy current losses in the backplate of the Faraday screen can be neglected.
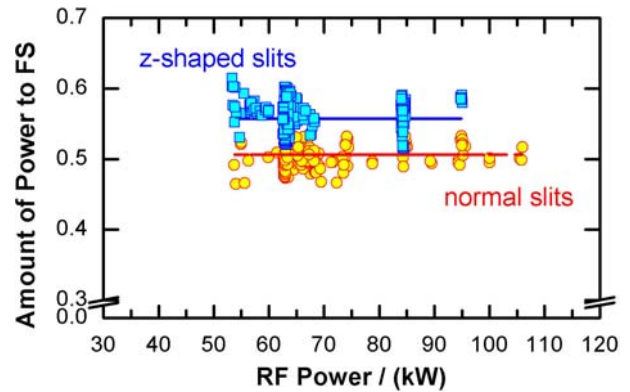
Figure 59: Amount of RF power received by the Faraday screen vs. RF power for the z-shaped slotted FS and the normally slotted FS.

These measurements show that the efficiency of both types of Faraday screens is identical.

4.1.2.2 Driver Light Emission

The light emission from the source of the driver has been used up to now for the RF ignition control and was measured rather simply with a light fiber and a photo diode. Due to the broad sensitivity of the used photo diodes this signal could not be used for a reliable RF efficiency measurement as other effects (i.e., Cs and other emission, thermal radiation, etc.) could alter the signal.

For a reliable comparison of the driver RF efficiency (also with BATMAN and RADI) all these photo diode diagnostics at the IPP test facilities have been upgraded by using an interference filter for H_α radiation and by subsequent calibration. Furthermore, all these photo diode diagnostics measure at the same driver position with the optic head in the center of the driver backplate.
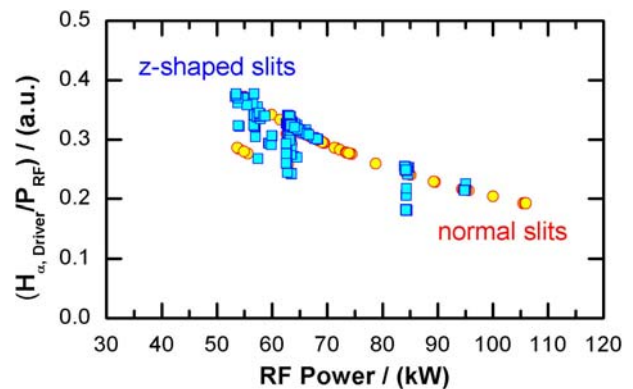
Figure 60: Normalized H_α emission from the driver vs. RF power for the z-shaped slotted FS and the normally slotted FS.

Figure 60 shows the comparison of the dependence of the driver H_α emission, normalized to the RF power, on the RF power itself for both types of Faraday screens. This normalized H_α emission decreases with increasing RF power, but — and this is important for the present analysis — the dependence is identical for both types of Faraday screens. This demonstrates again, that the coupling of the RF to the driver plasma and hence the driver RF efficiency is identical for both types of Faraday screens.

4.1.2.3 Summary

Both measurements show, that the RF efficiency, i.e. the efficiency of the RF coupling to the driver plasma is identical for both driver geometries. Hence, the z-shaped slotted Faraday screen can be used for ELISE and for ITER, due to its thermal advantages for the driver insulator.

4.1.3 Source Wall Coating

Another issue was the copper impurity problem (see also section 4.1.5). During the last experimental campaigns an increasing copper coating of the plasma grid was ob-

Figure 61: Mo coating of the Faraday shield and the source back plate including the cone

served. This was seen as a reason for poisoning the Cs layer and for the degradation of the source performance. The cone in the source back plate was identified being the last source of the sputtered copper and was therefore also coated with Molybdenum (see figure 61). After this change no further copper was observed on the plasma grid and in the long run the source performance became more stable in long pulses.

4.1.4 Beam Doppler-Shift Spectroscopy System

The beam Doppler-shift spectroscopy system is now working reliably and is used routinely during operation. The system is shown schematically in figure 62; it consists of 20 channels, 7 horizontal channels, viewing in vertical direction and 13 vertical channels, viewing in horizontal direction. The optic heads are mounted at the entrance of the water tank and are separated by a typical distance of 4 cm and have a viewing angle of about 50°. Due to the small background pressure in the tank, the H_α emission is rather weak; hence an integration time is rather large (typically 2 s).

The beam Doppler-shift spectroscopy is a rather simple tool, as no absolute calibration — both for the wavelength and the emission — is necessary. Even no relative calibration of the different LoS is necessary for divergence and stripping profiles. Figure 63 shows a typical H_α-spectrum of a central LoS at MANITU with a summary of the kind of information that can be gathered. The spectrum shows three peaks: (1) the un-shifted H_α peak at the nominal wavelength; (2) the Doppler-shifted peak, emitted by fast neutrals having the full accelerated energy; and (3) the so-called stripping peak in-between the latter two, caused by neutrals having less than the full energy. Those neutrals are generated by collisions of not fully accelerated ions with the residual gas in the tank and are therefore a measure of the amount of stripped ions in the acceleration system. As this happens at MANITU mainly in the first gap, the peak location corresponds to the extrac-
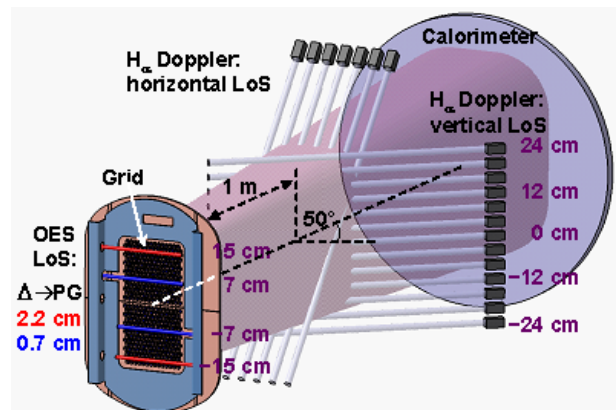

Figure 62: Sketch of the beam Doppler-shift spectroscopy system at MANITU.

tion voltage.

From those peaks, following information can be obtained:

- From the Doppler width, the divergence can be calculated taking various experimental line broadening effects into account. For the MANITU system, we assume furthermore no focusing effects due to simplicity. Since MANITU is typically operating below the optimum perveance, an increase in the Doppler width corresponds to a lower negative ion current density for constant extraction voltage.

Figure 63: Typical H_α Doppler spectrum of MANITU with the Doppler-peak caused by the fully accelerated ions, corresponding to the total voltage and the stripping peak, i.e. the Doppler-peak caused by not-fully accelerated ions.

- The stripping fraction can be calculated by the ratio of the integral of the stripping peak to the integral of the fully shifted peak, weighing with the different neutralization and emission cross

  section at the different energies. For simplicity, we assume that all stripped neutrals have the same energy, i.e. the extraction energy.

With the divergences and stripping factors obtained, a profile of these quantities across the beam and hence a measure of the beam homogeneity can be obtained (see section 4.4).

4.1.5 Reduction of Extraction Area

The extraction area at MANITU has been further reduced by covering the upper five and lower five rows of apertures from 204 cm^2 to now 132 cm^2.

Figure 64 shows the reason for the reduction: now almost all extraction apertures are within the driver projection, so that the plasma illumination of the extraction area is expected to be more homogeneous and hence the relative amount of apertures that contribute to the total current is increased; finally, the current density should be enhanced. The covers are made out of molybdenum and are cooled via the thermal contact to the plasma grid. This setup is very similar now to the
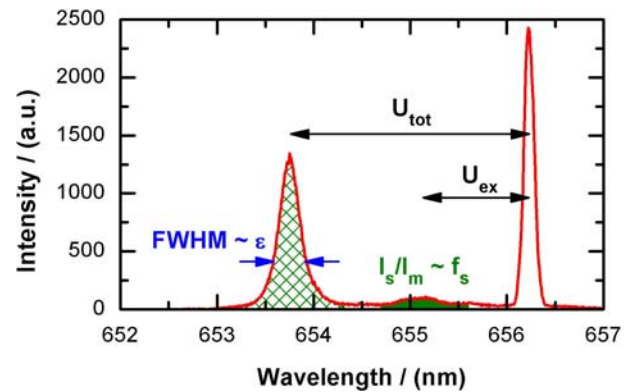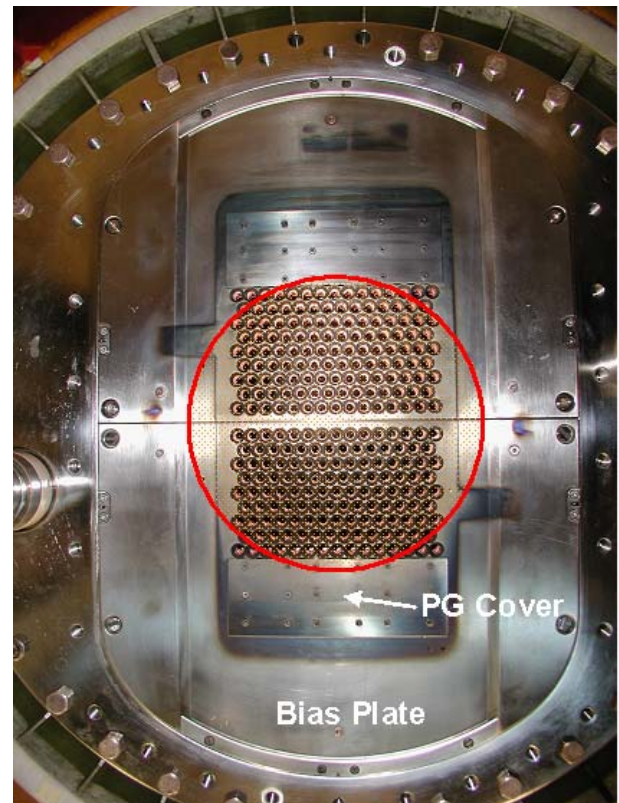

Figure 64: View onto the MANITU plasma grid with covers on top and bottom of the plasma grid. Number of apertures is reduced from 406 to 262 and the extraction area accordingly from 204 cm^2 to 132 cm^2. The red circle indicates the driver projection.

configuration at BATMAN, ELISE and the large ITER source. Here also all apertures are within the projection of the drivers.

Furthermore, the polarity of the magnetic filter field was turned in October 2009. Until then, the polarity of the horizontal magnetic filter field was so that the plasma was drifting to the top part of the plasma grid. There are strong indications (see sections 3.1 and 4.4) that the negative ions are produced mainly in the region opposite to the drift direction due to the deficit of electrons here so that less destruction takes place. With the present setup, the plasma drift directs to the bottom part of the source, i.e. the ions are created mainly in the top part. There was some hope, that this measure increases the amount of extracted negative ions: calculations with the CsFlow code (section 7.4) indicate that the Cs conditions at the upper part of the source should be more beneficial for the surface effect as the Cs oven is placed also at the top part of the ion source.

4.2   Identification of Copper Sources

The identification of the copper sources in MANITU was done by placing sputter probes within the source. Two campaigns were dedicated to this task. During the first campaign four copper probes were installed inside the source. Three of them were disposed on the border of the vessel and thus only received the ion flux from the out streaming plasma. The fourth one was installed at 45 degrees of the back streaming ion flux incidence, in the cone of the driver. It is the only one that presented erosion. Unfortunately, all the copper was eroded from this probe and thus only an estimation of the lower value of the back streaming ion flux was possible. This is what motivated the second campaign. During the second campaign, eight probes were symmetrically disposed in the cone of the driver and one on the border of the vessel. The goal was to determine more accurately the back streaming ions fraction and also to investigate on the existence of a gradient of the back streaming ions between the top and the bottom part of the cone (and thus between the top and the bottom part of the plasma grid). In all cases, the evaluation of the remaining copper was made by Rutherford backscattering spectroscopy (RBS). The experimental results were compared to simple 1D calculation. The calculations being rigorously the same for the first and second campaign, we will only detail the results obtained for the second campaign, and discuss the results of both campaigns.

This section is organized as follows: the first section is dedicated to the experimental results, while the second part is devoted to the calculations and the comparison with experiment.

4.2.1   Experimental Results

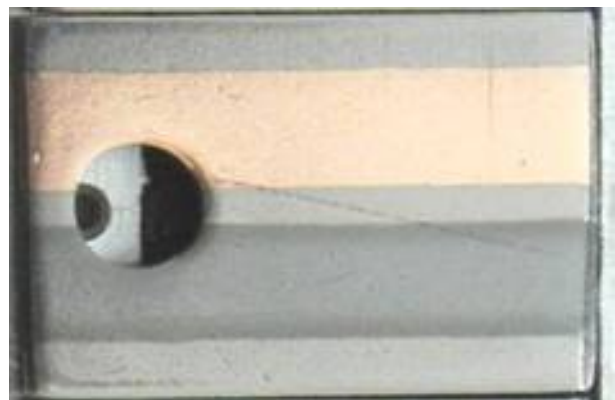During the first campaign, four probes were used. They consisted of a copper layer sputter depos-

Figure 65: Picture of one probe. The substrate is titanium; the top part is the deposited copper while the bottom part is chromium.

60

ited on stainless steel. The thickness of the copper layer, estimated by Rutherford backscattering spectroscopy was of 440±10% nm. None of the three probes which were located on the sidewall showed erosion. The fourth one, which was in the cone, showed erosion evidences, however all the copper was eroded. The exposure time to the back streaming ions was 48000 s. Consequently only the minimal value of back streaming ion fraction could be determined: it ranged between 2.2 and 2.7% (the evaluation procedure will be detailed for the second campaign).

Figure 66: Picture of the probes of the second campaign, taken at the end.

On the contrary to the first campaign, where only four copper probes were sputter-deposited on a stainless steel substrate, copper and chromium were used on the second campaign. The used substrate was titanium. Physical properties and especially the sputtering yield of chromium and copper by hydrogen being close motivated this choice. Figure 65 is a picture of one of the used sputter probes. The thickness of deposited copper and chromium was determined by RBS. Estimations are $12.8 \times 10^{18} \pm 10\%$ cm^{-2} (1505±10% nm) for copper and $5.4 \times 10^{18} \pm 10\%$ cm^{-2} (652±10% nm) for chromium.

Figure 66 shows the disposition of the probes on the cone which is located at the exit of the driver, at the end of the campaign. All the probes show the shadow of the screw (maintaining the probe to the vessel) that screened the flux of the back streaming ions. The orientation of this shadow (same direction as back streaming ion flux and behind the screw) proves that the observed erosion is due to back streaming ions. RBS analysis showed that on the six probes which were located in the flux of the back streaming ions, two were completely melted and one partially (no further analyze was possible). The remaining three showed traces of alloy formation and sputtering evidences. Bad heating conductivity (if, for example, the probe surface is not completely in contact with the cone) is responsible for the melting of the probes. The ones where alloy formation was found also indicate that the probes temperature went high (probes were exposed 86000 s in total to the back streaming ions flux). Finally, only one of the non melted probes showed low enough alloy formation not to hamper the analysis. The found erosion depth was of 10.2×10^{18} cm^{-2} for copper and 2.9×10^{18} cm^{-2} for chromium.

Figure 67: Sputtering yields of copper, chromium and molybdenum for incident H.

In order to determine the flux of the back streaming ions we need to know the sputtering yield. To this

aim, the back streaming ions energy distribution function (obtained by the 1D calculation, see next section) was used. TRIM.SP program allowed us to determine the sputtering yields. The mean yield was computed as follows:

$$\langle \boldsymbol{Y} \rangle = \alpha \int \boldsymbol{f}(\boldsymbol{E}, \mathrm{H}^+) \boldsymbol{Y}(\boldsymbol{E}) \mathrm{d}\boldsymbol{E} + \beta \int 2\boldsymbol{f}(\boldsymbol{E}, \mathrm{H}_2{}^+) \boldsymbol{Y}(\boldsymbol{E}/2) \mathrm{d}\boldsymbol{E}$$

In this relation, $\langle \boldsymbol{Y} \rangle$ is the mean yield, $\boldsymbol{f}(\boldsymbol{E}, \mathrm{H}^+)$ and $\boldsymbol{f}(\boldsymbol{E}, \mathrm{H}_2{}^+)$ are the ion energy distribution functions of H^+ and $\mathrm{H}_2{}^+$ respectively, $\boldsymbol{Y}(\boldsymbol{E})$ and $\boldsymbol{Y}(\boldsymbol{E}/2)$ the yields at the corresponding energy E for H^+ and E/2 for $\mathrm{H}_2{}^+$ (this ion being neutralized and dissociated in two H

Figure 68: Cross sections for negative ions simple and double stripping, ionization of background neutrals by hot H and hot H ionization.

with half of the energy each). Alpha and beta are closure parameters. Figure 67 shows the sputtering yields of copper, chromium and molybdenum (RBS showed the deposition of small molybdenum layer on both copper and chromium) for incident H atoms. Knowing the mean yield and using the erosion depth, the mean back streaming ion flux is:

- 2.5×10^{15} cm^{-2}s^{-1} for the copper

- 7.6×10^{14} cm^{-2}s^{-1} for the chromium.

The mean extracted negative ion current density being of 16.1 mA/cm^2, we find for the back streaming ion fraction 2.5% and 0.8% for the copper and chromium, respectively. The difference observed between the copper and the chromium is still an open question. It could be due to the fact that copper reacts with cesium and water when the source is opened, leading to a chemically induced erosion, and thus to a further decrease of the copper thickness.

Concerning the probe located on the sidewall, no evidence of erosion was found indicating that the copper source is not on the sidewalls.

The results obtained during the first campaign are in good agreement with those obtained during the second campaign.

4.2.2   Simple Calculus for the Back Streaming Ion Fraction

We will in this section develop the calculus to determine the back streaming ion fraction.

Let us first describe the extraction / acceleration zone. The negative ions are created (at rest) on the plasma grid (PG) and then accelerated to the extraction grid (EG). Typically the voltage between PG and EG is 7.5 kV. Following extraction grid is the grounded grid (GG). Voltage between EG and GG is 12.5 kV. So finally, negative ions are accelerated up to 20 kV between PG and GG. In order to determine the back streaming ions rate, we first need to determine which species are able to generate cations. The extraction of
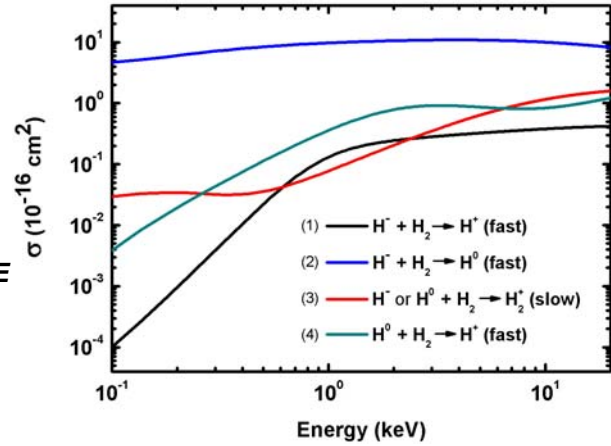
negative ions inevitably leads to the simultaneous extraction of electrons from the ion source. These electrons are magnetically deflected onto the extraction grid to avoid their acceleration to full energy. These electrons can ionize background neutrals; however the ionization cross section is rather low.

Figure 68 shows the cross sections of the mechanisms leading to the generation of back streaming ions taken from Ref. [7]. These are:

1. Double stripping, leading to a fast H^+:
$$H^- + H_2 \rightarrow H^+ \text{ (fast)} + 2e$$

2. Simple stripping leading to the generation of a fast neutral:
$$H^- + H_2 \rightarrow H^0 \text{ (fast)} + e$$

3. Ionization of the background gas:
$$H^-, H^0 + H_2 \rightarrow H_2^+ \text{ (slow)} + e \ (+ e)$$

4. Ionization of a fast neutral:
$$H^0 \text{ (fast)} + H_2 \rightarrow H^+ \text{ (fast)} + e$$

The fast neutral from reaction (2) can in turn generate positive ions via reactions (3) and (4). The second possibility for the labeled (3) cross section is the ionization of a background gas neutral directly by a negative ion.

So finally we have two reactions which are single step processes (1 and H^- part of 3) and two other reactions which are two steps processes (4 and H^0 part of 3), occurring when (2) is realized.

The simple calculations which will be developed below are 1D, we assume that all the ions have an ideal rectilinear trajectory. Moreover, no interaction between ions or between ions the walls are taken into account.

Figure 69 represents the pressure and potential variations between the PG and GG for 0.4 Pa source pressure. During this campaign the discharge pressure varied between 0.4 and 0.6 Pa. Instead of taking the
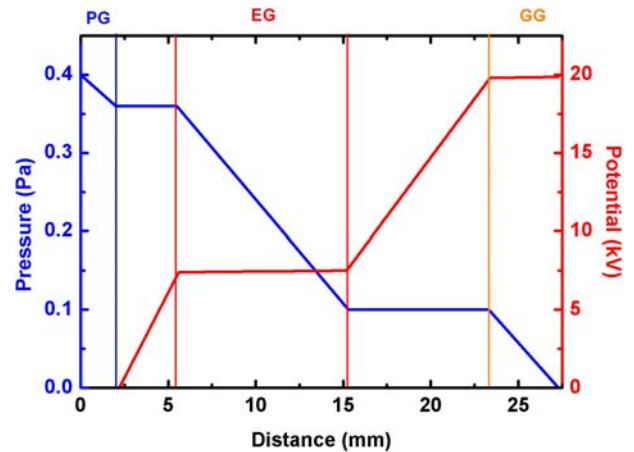

Figure 69: Pressure and potential variation along the extraction and acceleration zones
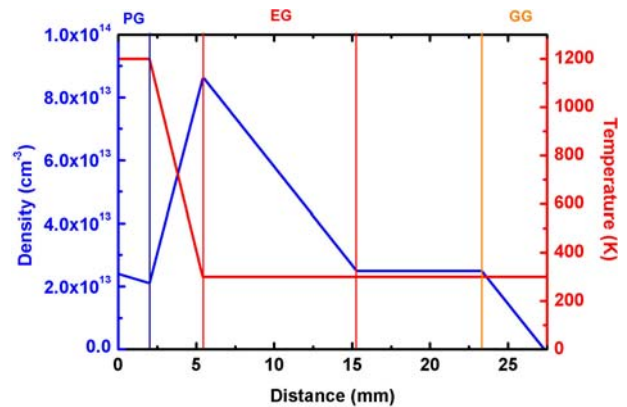

Figure 70: Density variation along the acceleration zone and potential profile obtained for a source pressure of 0.4 Pa (tank pressure of 10^{-3} Pa) and a gas temperature of 1200 K up to extraction grid, 300 K beyond.
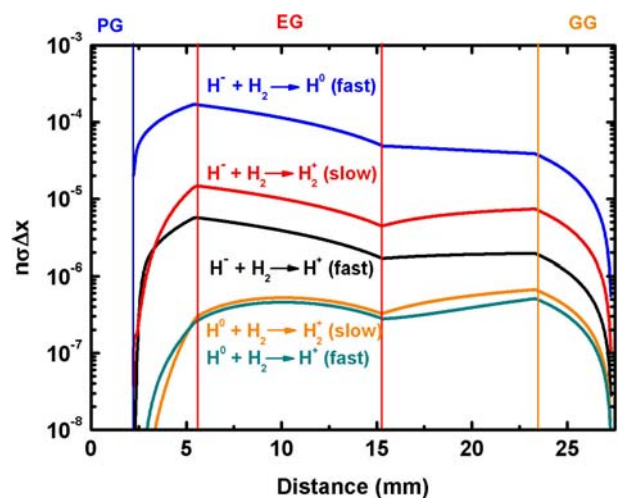

Figure 71: Simple stripping (in blue) and positive ion generation zones.

mean pressure value we will compute for 0.4 Pa (which will be detailed) and 0.6 Pa (results will be given) in order to obtain an order of magnitude of the back streaming ion fractions since the purpose of this study is not to have the most accurate simulation of the back streaming ions generation (see 8] for a detailed MC calculation).

An important aspect of this calculation is the density profile in the accelerator. Indeed, optical emission spectroscopy showed that the gas temperature was in the order of 1200 K within the plasma grid and extraction gap and 300 K beyond, assuming thermal dissipation.

Figure 70 shows the density variation and temperature profiles within the acceleration zone calculated for 0.4 Pa source pressure. The increase in density between PG and EG corresponds to the decrease of the background gas temperature.

Figure 71 represents the nσΔx product, with n being the background density, σ the cross sections and Δx the position steps. Despite being dimensionless, this produçt allows us to visualize the zones where simple stripping occurs (in blue) and also where the back streaming ions are generated. Red and black curves represent the back streaming ion generation by single step mechanism while the orange and the green curves represent the generation of back streaming ions in the case of a double step mechanism.

Figure 72: Ion energy distribution function of the back streaming H^+ and H_2^+ ions
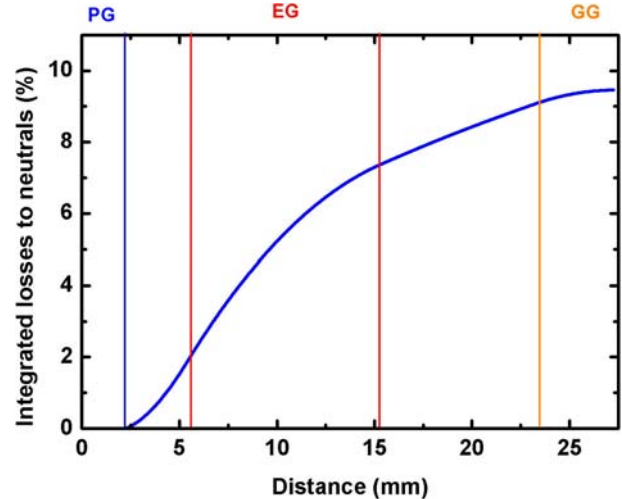
Figure 73: Losses to simple stripping

The proportion of positive ions coming from each zone and obtained by integrating the curves from figure 71 is summarized in table 2. It appears that most of the back streaming ions (more than 80%) between the EG and the GG. The ion energy distribution function (IEDF), which was used previously to determine the mean sputtering yield (see previous section), was obtained using figure 71. Figure 72 shows the ion energy distribution function obtained for the H^+ and H_2^+ ions. A proportion of 36%
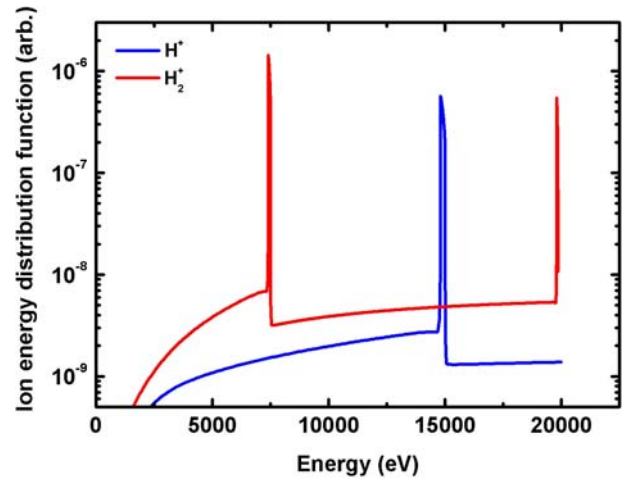
	PG ≤ x ≤ EG	EG	EG ≤ x ≤ GG
S. Strip.	20.1%	55.8%	24.1%
H^+	15.5%	53.1%	31.4%
H_2^+	10.3%	52.3%	37.4%

Table 2: Relative positive ion generation in the different zones of the extraction system
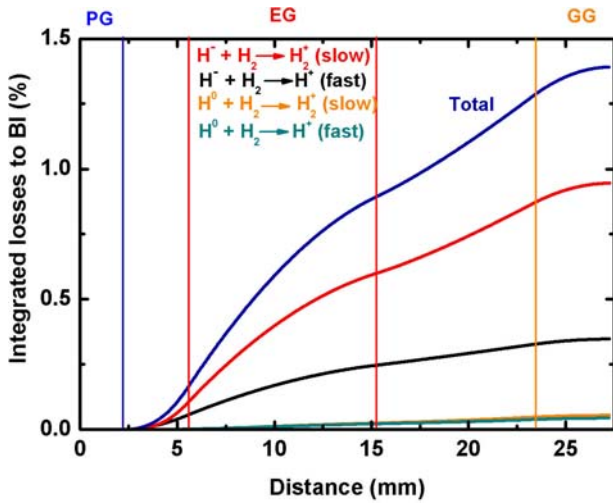
Figure 74: Contribution of the different mechanisms to the back streaming ion losses.

	Calc.	RBS Cu	RBS Cr
0.4 Pa	1.4%	2.5%	0.8%
0.6 Pa	2.1%	2.5%	0.8%

Table 3: Comparison between experiment and 1D simulation.

Figure 75: Total beam losses.

of H^+ and 64% of H_2^+ ions were found. The two peaks at 7.5 keV and 20 keV in the H_2^+ IEDF corresponds to the back streaming ions generated within the extraction grid and within the grounded grid. Indeed, in figure 69, we see that the potential is almost (but not completely) constant within these two grids. Since the H_2^+ ions originates from the ionization of a background neutral (300 K), these back streaming ions have the energy corresponding to the local potential at which they were created. Concerning the H+ ion distribution function, only one peak is located at 15 keV.

Indeed, H^+ ions are not generated from the background neutrals but from the incident negative ions or neutrals. Consequently they are not created at rest and thus have to be decelerated before being repelled by the potential. The 15 keV corresponds thus to the H^+ ions generated within the EG at 7.5 keV which are decelerated and repelled (2 x 7.5 kV). Figure 73 represents the losses to simple stripping while figure 74 shows the losses to positive ions for all the involved mechanisms. At 0.4 Pa, we find 9.5% losses of the negative ion beam to simple stripping and 1.4% losses to back streaming ions. The total beam loss is of 11%, as can be seen on figure 75.

Table 3 compares the results for the back streaming ion fraction obtained at 0.4 and 0.6 Pa to the RBS estimations.

Estimations of the first campaign calculations were of 2.4% (compared to 2.2-2.7% for RBS).

In any case, the computed back streaming ion fraction is in good agreement with the RBS estimations. None of the probes located on the sidewalls, during the first nor the second campaign showed any erosion evidence. This proves that the copper source (after having coated the Faraday shield with molybdenum, which was the main source of copper) is the cone.
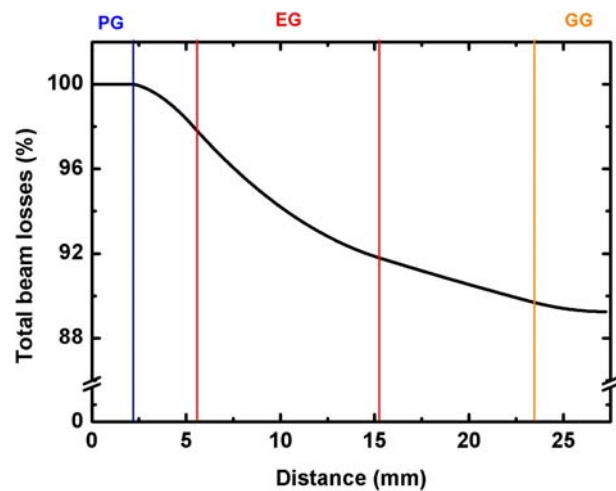
4.2.3   Conclusion

The main copper source was found to be the Faraday shield. However, after having it coated by molybdenum, spectroscopy showed still some smaller copper traces. This is what motivated those studies. In order to determine the possible sources, which were either the sidewalls, the cone at the exit of the driver or either both, sputter probes were installed at these two locations.

The first campaign showed a complete removal of the copper for the probe located on the cone, and thus the estimation of the back streaming ion fraction was the minimum value.

During the second campaign, most of the probes were damaged because of a bad heat conductivity (some of them melted). However on the one where analyze was still possible, the back streaming ion fraction was determined to be 0.8% for Cr and 2.5% for Cu.

A simple calculus was used in order to estimate the back streaming ion fraction. The results for 0.4 and 0.6 Pa are 1.4% and 2.1%. A good agreement is found between these results the RBS. For both campaigns, the probes located on the sidewalls of the vessel showed no evidence of sputtering, proving that the remaining copper source was the cone. Recently, the cone was coated with molybdenum, and since, no more copper is seen with spectroscopy, confirming the results of this study.

4.3 Long Pulses with Coated Source Walls

4.3.1   Experiments in Hydrogen

4.3.1.1   Low Pressure Operation

The digital valves in gas feed system were replaced by a flow controller. This enables a much finer setting of the source pressure and allows source operation below 0.3 Pa. With or without plasma, the pressure in the driver is always higher as in the source (see figure 76). The source pressure, which causes the stripping losses, is denoted in the following as the "filling pressure". After improved RF shielding of the pressure measurement it turned out, that during source operation the pressure in the driver as well as in the source decreases only slightly. This observation is consistent with the loss of particles by gas heating (neutral depletion).

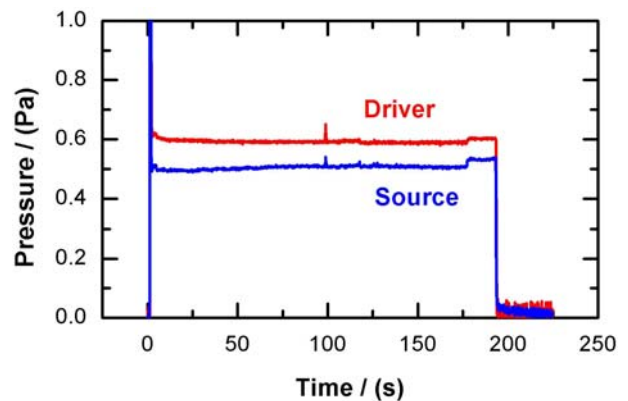Source operation below 0.37 Pa is not possible in the present design without cesium. If a suffi-

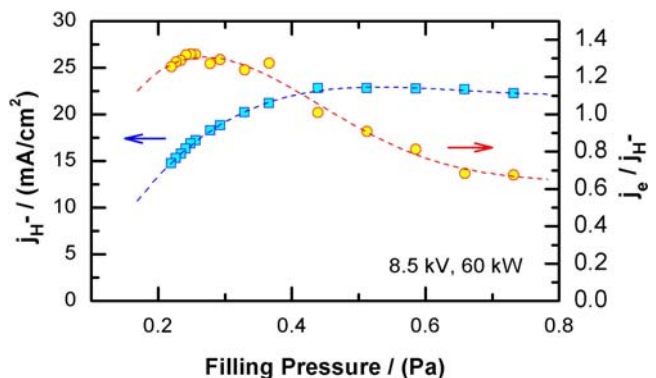*Figure 76: Pressure change in the driver and in the source during plasma operation.*

Figure 77: Negative ion and electron current density as a function of the source pressure at 60 kW.
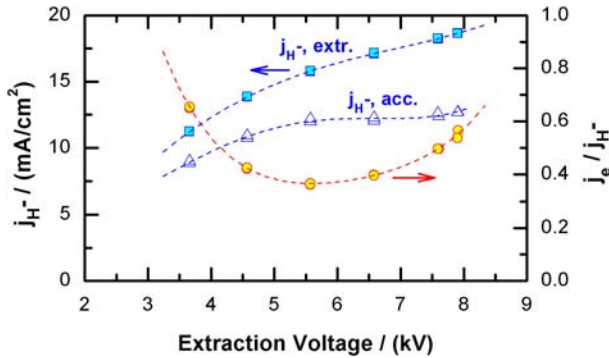
Figure 78: Extracted H- current density, calorimetric measured H- current density and electron fraction as a function of the extraction voltage.
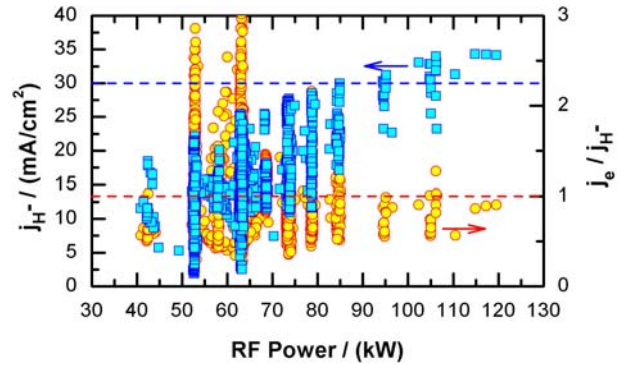

Figure 79: Extracted H- current density, and co-extracted electron fraction as a function of the RF power in all pulses with different other parameters. The dashed lines indicate the ITER requirements.

cient Cs inventory is in the source, the signals of H_α, H_β, Cs852 und the H- ion current are increasing in a similar timescale of about 50 s. After this time the pressure can be reduced down to 0.2 Pa without extinguishing the plasma. The evaporated Cs seems to support low pressure operation. In this region the H- ion current density decreases as a function of the pressure but the electron current decreases also (see figure 77).

4.3.1.2 Increase of Extraction Voltage

In the previous set-up the extraction voltage was limited by the voltage drop across the switching tetrodes to less than 9 kV, which is below the ITER parameter and which limited the achievable ion current. By reducing the voltage drop the parameter range of the extraction voltage could be extended to 10 kV. Figure 78 shows the dependence of the extracted and accelerated current densities as well the amount of co-extracted electrons in dependence on the extraction voltage.

The electron/ion ratio reaches a minimum at 6 – 7 kV and increases at higher voltage. The extracted ion current is also increasing, but the accelerated ion current on the calorimeter saturates. Therefore only extracted ion currents are rated in this report.

This dependence of the ion and electron currents on the extraction voltage is a consequence of the beam optics of this particular extraction system. It can be assumed that the decrease of the electron current at low voltage as well as the increase at high voltage is caused by an ion contribution. Unfortunately, the LAG system must be operated for high negative ion current density conditions in the underperveant range, as it was designed in the late 90's for an optimum perveance at 20 mA/cm² and 5.4 kV (see also the respective discussion for BATMAN in section 3.1.3.2 on page 22); the observed minimum of the amount of co-
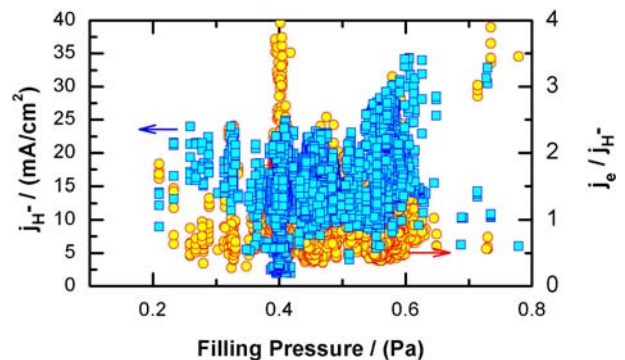

Figure 80: Pressure dependence of H- current density and electron fraction in all pulses with different other parameters
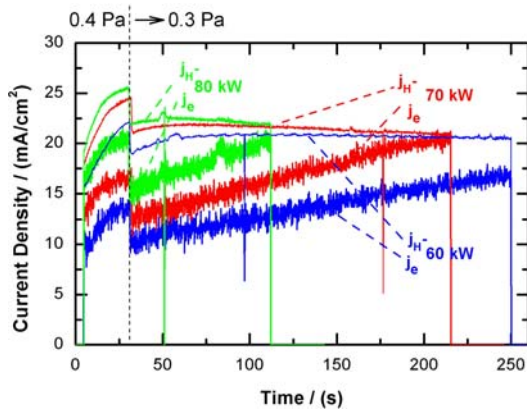
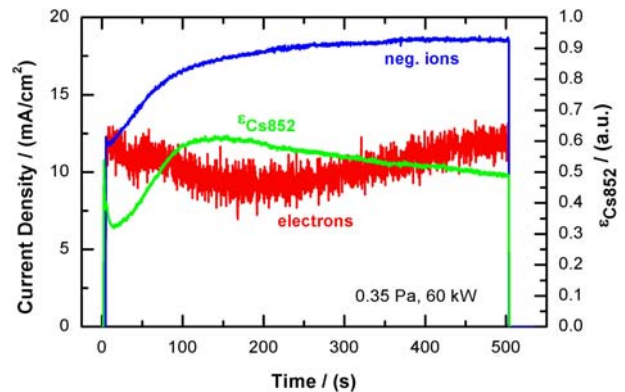Figure 81: Reduction of the source pressure at different RF power.

Figure 82: Typical time behavior of the currents and the cesium signal in a long pulse.

extracted electrons fits rather well in this range. Hence, with the given beam optics of the LAG system high H- current densities and low amounts of co-extracted electrons and hence the ITER requirements can not be achieved simultaneously. By an optimized extraction system, as it it the case for ELISE, allowing operation at the perveance optimum at high extraction voltage (8 - 9 kV) without increasing electron current improved long pulses at high power operation can be expected.

4.3.1.3   High Power Operation

High extracted ion current densities of up to 35 mA/cm^2 could be achieved by raising the RF power to up to 120 kW (see figure 79). But this was only possible, when the power was increased for some seconds within a long pulse with low power. Longer pulses with high power were prevented by the steadily increasing electron current (see also figure 81 below).

For achieving high currents it was necessary to operate at elevated pressure of at least 0.5 Pa (figure 80), with a weakened filter field and at high extraction voltage. Figure 79 and figure 80 summarize the results of the experimental campaign with hydrogen. The upper envelope of figure 79 represents the highest currents achieved under optimal conditions.

4.3.1.4   Long Pulses

Figure 81 shows an example of the decrease of the ion current after reduction of the pressure to 0.3 Pa and shows also the raising electron current. Because the increase of the electron current is steeper at high power the pulses have to be stopped earlier to protect the extraction grid from overload and therefore long pulses are only possible with lower RF power and medium extraction voltage.

The Cs signals in long pulses are never constant. A typical behavior is: As long as the Cs signal rises, the electron current is stable, as soon as the Cs signal flattens off or starts to decline, the electron current begins to increase (see figure 82). This behavior is perhaps caused by the temporal evolution of the bias plate temperature, which is not properly cooled. An indication for that is that the time constants of the temperature increase (from about 40 °C to more than 130 °C within some tens of seconds) are consistent with the time constants of the changes of the Cs emission and the electron current. Furthermore, CsFlow calcula-

tions (see section 7.4) indicate that the Cs coming from the bias plate plays an important role for keeping the plasma grid conditions good enough for negative hydrogen ion production. To enable stable long pulses one has therefore to make sure that enough cesium is on the plasma grid or on the bias plate. A realistic result for the extracted H- ion current density in pulses up to 500s with an electron/ion ratio below 1 is in the present set-up about 20 mA/cm^2.

As mentioned above (section 4.1.5), it was expected that the reduction of the extraction area and the changed polarity of the filter field increases the maximum achievable ion current density. However, the experiments so far do not yet give a clear answer whether this is the case.
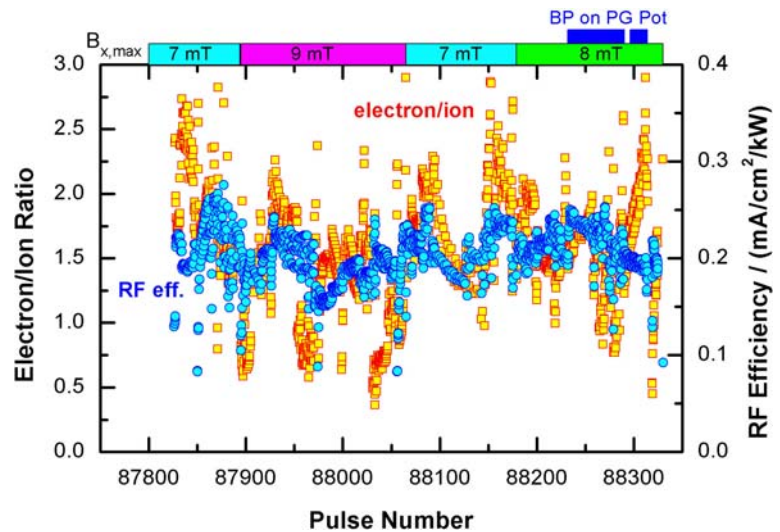
Figure 83: Source performance for the deuterium campaign for different magnetic filter field configurations, indicated by the maximum horizontal field strength at the plasma grid; for some pulses, the bias plate was connected with the plasma grid and commonly biased versus the source body.

4.3.2   Experiments in Deuterium

The experiments in deuterium were performed after the hydrogen campaign. The goal was to find the best filter field and the optimal conditioning procedure. Figure 83 shows on overview of all the experiments with different filter configurations. The problem are the high electron currents which can be suppressed only by strengthening the filter field by additional permanent magnets on each side and by biasing the plasma grid as shown in figure 84. In both cases the deuterium negative ion current density at the same power is also reduced and is lower compared to hydrogen operation. The best solution to strengthening the filter was to add on each side only one row of permanent magnets, which was the lowest row of the confinement magnets. The maximal deuterium ion current density, however, did not exceed 20 mA/cm^2, even at more than 100 kW (see figure 85).

In long pulses, as in hydrogen, but even more pronounced, the applicable RF power is restricted by the increasing electron current and therefore a current density of only 12-15 mA/cm^2 D$^-$ is achievable (see figure 86). Figure 87 shows one of the best long pulses in deuterium.
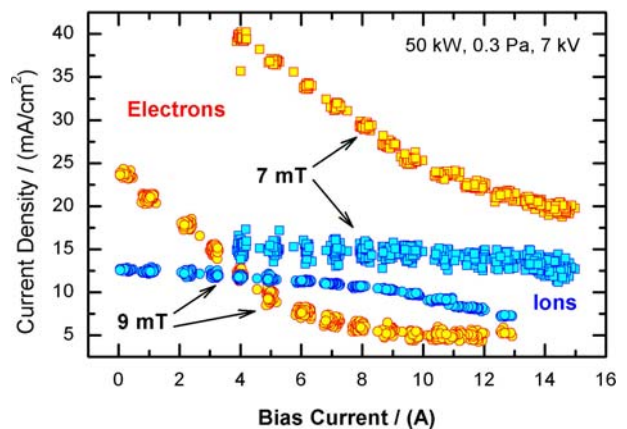
Figure 84: Reduction of the electron current in deuterium with standard filter (7 mT at PG) and strengthened by   three rows of permanent magnets (9 mT at PG)

The deuterium experiments were followed by another short hydrogen campaign with the same experimental setup. The source performance was not as good as it was before the deuterium operation. In particular the electron current was significantly higher and could not be reduced by the common conditioning procedures (optimization of cesium evaporation rate and pulse/interrupt time). The deuterium results may be affected by this degradation. Such long range changes of the source performance were observed several times in the past. A possible reason may be the poisoning of the Cs inventory by impurities other than Copper, because this time no sputtered copper was observed on the plasma grid. If the degradation happens, the source has to be removed and all inner surfaces have to be cleaned. This is planned before the next deuterium campaign.

4.4 Beam Homogeneity

4.4.1 Dependence of Divergence Profiles on the Magnetic Filter Field

For the experimental campaigns reported above, the magnetic filter field was created by magnets inside the source body with a horizontal magnetic filter field strength near the PG of 7 mT. The field strength could be changed by attaching magnets outside the source body, by choosing the polarity of the external magnets with respect to the filter field, the field near the PG could be increased or decreased by 1 mT or 2 mT, respectively. This method, however, has the drawback, that it also changes the 3D structure of the magnetic filter field. Hence, a flexible magnet frame was also constructed like that one in BATMAN and installed during the summer break (see section 4.5). The polarity of the standard field was reversed during the experiments changing the direction of the observed vertical plasma inhomogeneity across the PG. As the latter is most probably caused by a drift of the plasma, the field polarity is indicated in the following either with "Drift up" and "Drift down", according to the maximum of the plasma density.
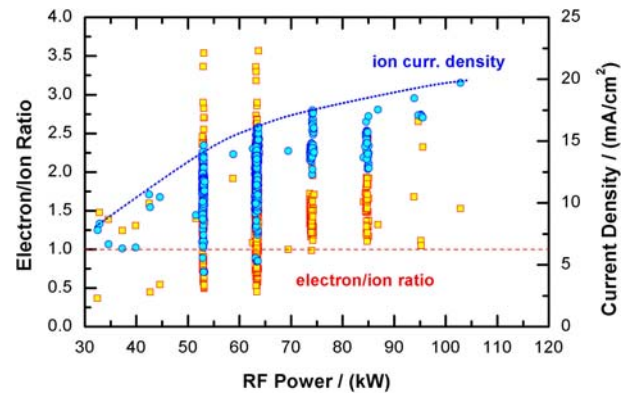

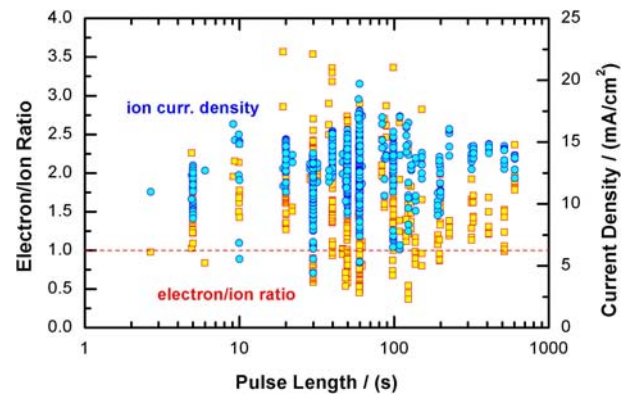Figure 85: Dependence of the source performance in deuterium on the RF power for all pulses

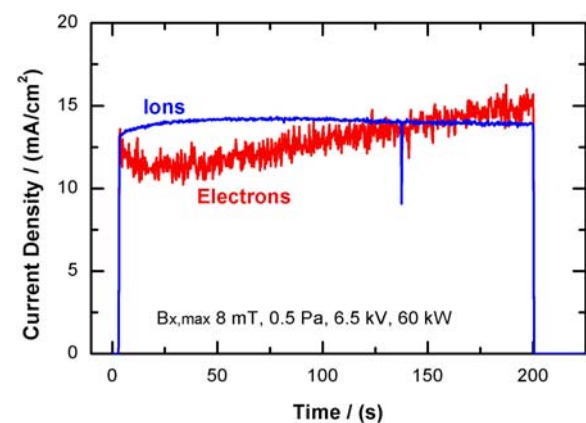Figure 86: Dependence of the source performance in deuterium on the pulse length for all pulses.

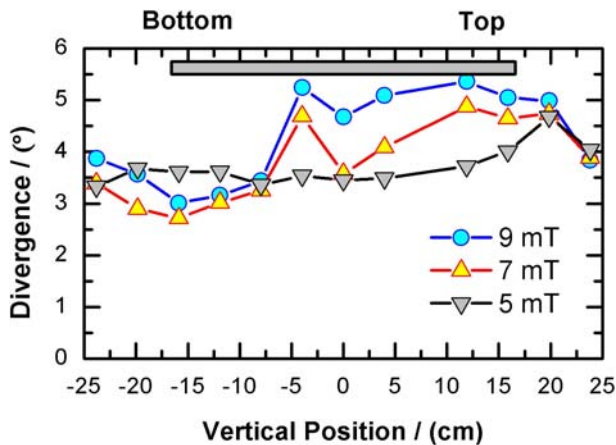Figure 87: 200 s pulse in deuterium with 60 kW and 0.5 Pa.

Figure 88: Vertical divergence profiles at MANITU for different filter field configurations for hydrogen pulses. The extraction area — indicated by the grey rectangle — is 204 cm^2, the plasma drift upwards. All pulses have similar normalized perveance of about 0.05.

Figure 88 shows the dependence of the vertical divergence profiles for hydrogen operation on the magnetic field configuration. These data were obtained for a large extraction area (204 cm^2) and with the polarity of the magnetic filter field so that the plasma drifts to the upper part of the PG.

It can be clearly seen that for the low magnetic filter field (5 mT) the divergence profile is more or less
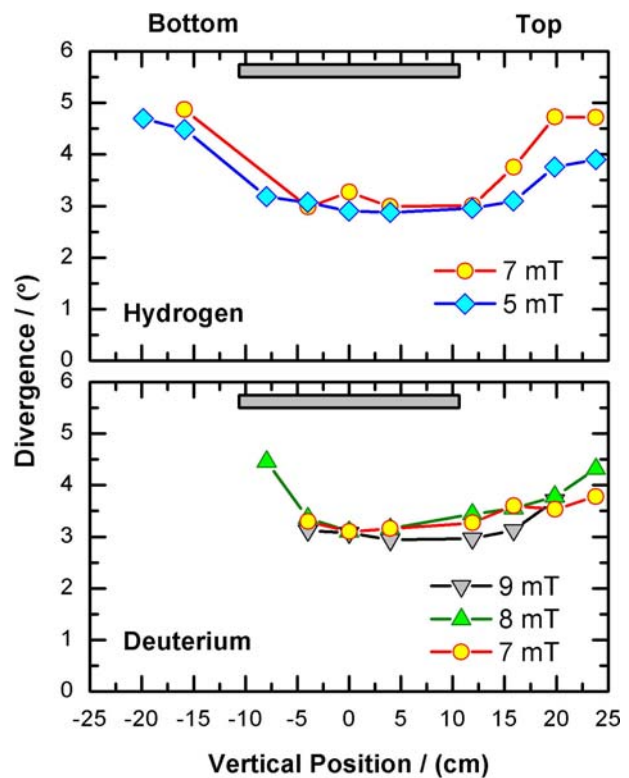

Figure 89: Vertical divergence profiles at MANITU for different filter field configurations for hydrogen (top) and deuterium pulses (bottom). The extraction area — indicated by the grey rectangle — is 132 cm^2, the plasma drift downwards. All pulses have similar normalized perveance of about 0.06.

symmetric and rather homogeneous. For the larger magnetic filter fields the divergence profile becomes more inhomogeneous: the divergence at the bottom part of the beam is lower than the divergence of the upper part of the beam. This indicates that the local current density in the upper part of the PG is lower than in the lower part. The 'dip' in the vertical profiles at the center of the beam for the stronger filter field cases is most probably caused by the overlap of the two partial beams emitted from the MANITU grid system due to the inclination of the two grid halves of the MANITU grid system. The detailed mechanism, however, is still not understood.

Due to these results, the magnetic field polarity was reversed for the next experimental campaign (drift down), as the Cs oven is also located at the upper part of the source. Hence an improved performance was expected. Additionally, the size of the extraction area was reduced to 132 cm^2 in order to minimize the area outside the driver projection.

Figure 89 shows the dependence of the vertical homogeneity on the magnetic field configuration for hydrogen and deuterium pulses with the smaller extraction area and a reversed magnetic filter field. For deuterium operation, only pulses with increased magnetic filter field strength have been performed. Operation in deuterium at 5 mT is not possible due to a non-sufficient suppression of the co-extracted electron fraction.
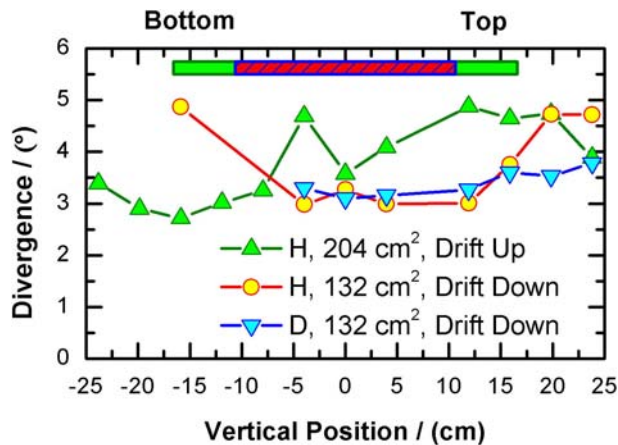
Figure 90. Dependence of the beamlet divergence for hydrogen and deuterium pulses for the standard magnetic filter field (7 mT) for the two different cases of plasma drift and extraction area.

In contrast to the results shown in figure 89, the divergence profiles for these experimental conditions do not show a dependence on the magnetic filter field, neither for hydrogen or deuterium. The homogeneity is also much better. As expected due to the field reversion, the beam is concentrated in the upper part of the PG; hence the majority of the negative ions are extracted again from the part of the PG opposite from the plasma drift direction.
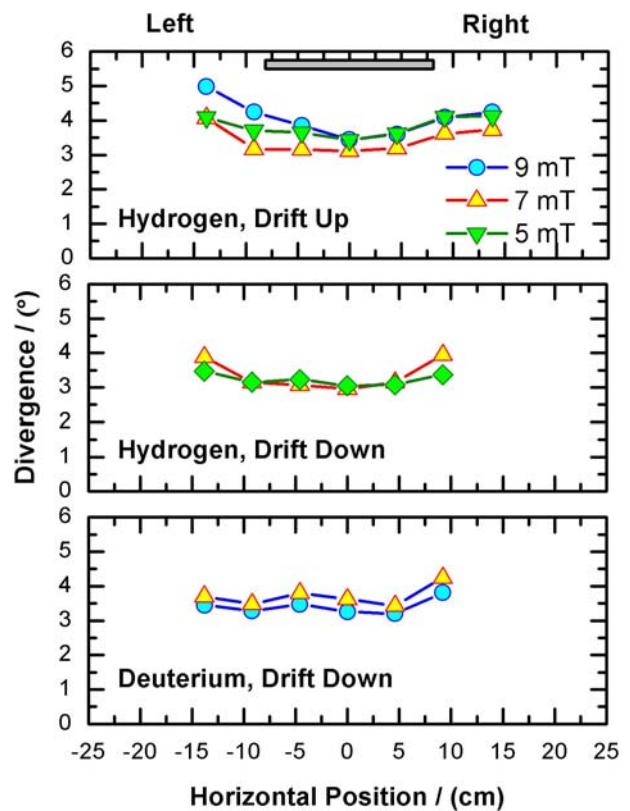

Figure 91. Dependence of the beamlet divergence for deuterium pulses on the normalized perveance for different LoS. Extraction area was 132 cm^2, drift downwards.

But the concentration of the beam at the "low plasma" region is much more pronounced in the case of the small extraction area and plasma drift downwards. This is indicated in figure 90, where a comparison of the three cases for the standard filter field configuration (7 mT) is shown. Even data of the LoS at -8 cm and -12 cm are missing for the "drift down, small extraction area" case, although these LoS are still within the projection of the extraction area. As discussed above, this indicates that the beam intensity within these LoS is too weak for H$_\alpha$ excitation above the noise level. The minimum divergence (about 3°) is more or less the same in all cases, but this is due to the fact that all pulses shown here have roughly the same normalized perveance P/P_0, P being the overall beam perveance (= I_{ex}/E_{ex}), and P_0 the perveance of a planar diode. The measured minimum divergence agrees also rather well with results of ion beam calculations and with results of the BATMAN test facility.

Figure 91 shows the horizontal divergence profiles for the different configurations. The profiles are more or less symmetric with a slight increase of the divergence at the beam edges.

The reason for the large discrepancy in the dependence of the vertical beam inhomogeneity on the magnetic filter field for the configurations shown is not clear. Unfortunately, due to technical and operation time limitations, data for corresponding cases — for example deuterium data or "drift down" data for the large

extraction area — are missing. In all cases, the source was well conditioned with cesium; the respective data (amount of co-extracted electrons and extracted current density) are shown in figure 92.

There are two main differences, which might affect the plasma dynamics in front of the PG and/or the negative hydrogen ion distribution at the meniscus: (1) In the case of the large extraction area (204 cm^2), some grid areas on top and on bottom of the PG are outside the projection of the driver; and (2) there is an intrinsic asymmetry of the MANITU source as the Cs oven is located on top of the source. Neither of these effects, however, is present at the large sources foreseen for ELISE and ITER.

Figure 93 shows the dependence of the beamlet divergences for several LoS for deuterium pulses on the normalized perveance. It shows that due to the particularities of the MANITU grid system (see section 4.3.1.2) operation is done mostly in the in the underperveant region. Hence, as it was discussed above, the divergence depends linearly on the perveance. But there is no strong dependence of the inhomogeneity of the divergence on the perveance; if at all, the inhomogeneity improves with increasing perveance. Furthermore, the beam is concentrated more and more in the center, indicated by the disappearance of the Doppler peak for the LoS at 20 cm.

Figure 92. Amount of co-extracted electrons (top) and extracted current density (bottom) for the pulses shown in the previous figures.

Figure 93. Dependence of the beamlet divergence for deuterium pulses on the normalized perveance for different LoS. Extraction area was 132 cm^2, drift downwards.

4.4.2 Beam Homogeneity vs. Plasma Homogeneity

Figure 94 shows a comparison of the beam inhomogeneity for the pulses shown in figure 88 and figure 89 with the plasma inhomogeneity. The respective inhomogeneities (plasma and beam) are given by the asymmetry factor that is defined by the deviation of the ratio of suitable parameters from unity. With that definition, a perfectly homogeneous beam or plasma has an asymmetry factor of zero. Positive values of the asymmetry factor indicate plasma/beam concentration at the upper part, negative values at the lower part of the source/beam line. For the plasma asymmetry, the LoS-integrated H$_\beta$ emission is evaluated in regions near the PG for the upper and lower parts of the source (see figure 62). The choice of suitable parameters for the beam, however, is not straightforward. In order to reduce numerical artifacts due to missing or large
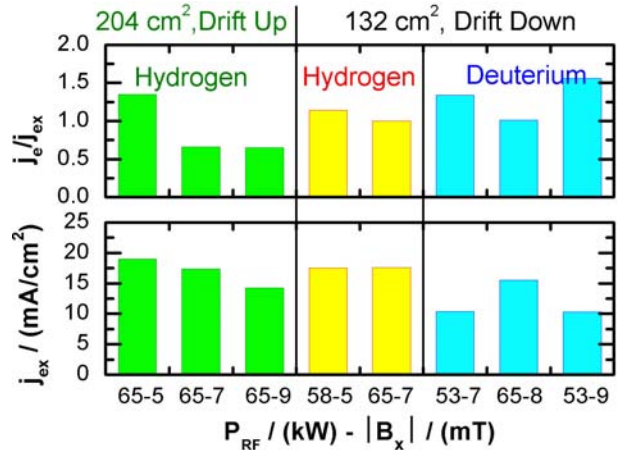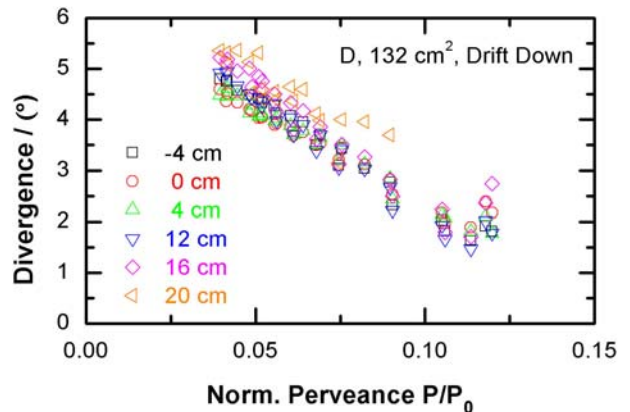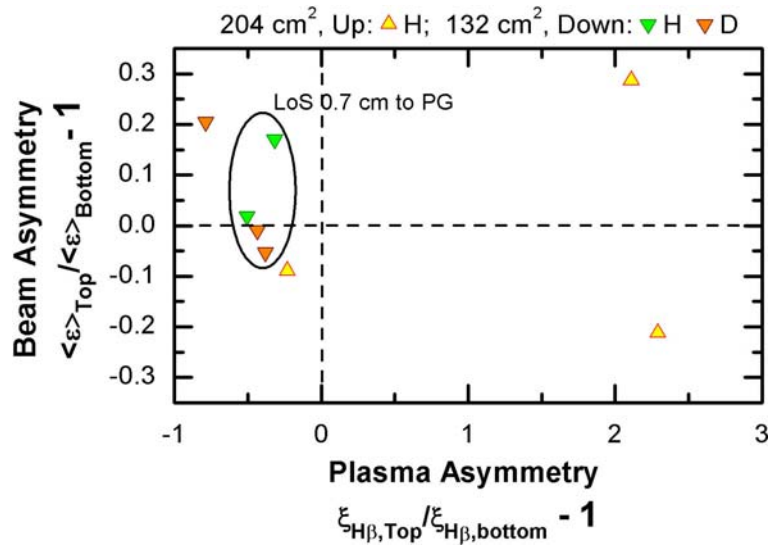
Figure 94: Comparison of beam and plasma asymmetry for the pulses shown in figure 88 and figure 89.

erroneous data, the average divergences of the upper and lower beam regions are evaluated, even if especially for the lower beam part of the small extraction area only a few data points are available.

Figure 94 indicates no clear correlation between plasma and beam asymmetry. It can be also seen that the plasma asymmetry cannot be correlated clearly with the assumed drift direction: the "204 cm^2, Up" data point with a plasma asymmetry of -0.3 corresponds to a filter field with 5 mT at the PG. This might be caused by the change of the 3D structure of the magnetic filter field due to the applied method of changing the magnetic field. Hence, for the upcoming campaigns, the internal magnets have been removed and a magnet frame was installed. This allows flexible changes of the filter field without change of the 3D structure.

The numerical problems in defining the beam asymmetry are highlighted for the hydrogen data with the small extraction area: although both profiles agree rather well, the calculated asymmetry factor differs by 20%. A final conclusion might only be possible after a relative calibration of the MANITU LoS so that also the Doppler peak intensities can be evaluated or eventually by measurements at the large ion sources at ELISE or SPIDER where more LoS near the PG for source OES are available. But, and this is an important result, the beam seems to be much more homogeneous than the plasma in a certain distance to the PG. This indicates that the negative hydrogen ion density distribution at the plasma meniscus is linked only weakly with the plasma parameters at a certain distance from the PG. It is in agreement with modeling results showing that the negative ions are mainly produced by — intrinsically symmetrically — impinging neutrals. Asymmetries can only be caused by Cs coverage of the PG with inhomogeneous conversion yields and by the positive ion distribution needed for space charge compensation and leading to negative hydrogen ion losses due to mutual neutralization.

4.4.3 Stripping Losses

No dependence of the stripping fraction from the magnetic field configuration is observed — it is also not expected. The most important dependence is on the source pressure: this is shown in figure 95 by a

comparison of vertical profiles of the stripping losses for two pulses with different source pressures. The profiles are very similar, the shapes themselves, however, are still a subject for further investigation.

Figure 96 shows the dependence of the average stripping losses on the source pressure. The well known linear dependence can be seen, which is also predicted by calculations. The measured stripping losses at MANITU, however, are much lower (factor 5) than model calculations with a simple analytical model predict. This model calculates the background gas density profile within accelerator and beam line by tak-

Figure 95. Vertical profile of stripping losses for hydrogen pulses with different source pressure. Extraction area was 132 cm^2, drift downwards.

ing into account just the conductance of the grid apertures as well as the source and beam line pressures. This model was benchmarked against a Monte Carlo model for the ITER NBI accelerator system [by S. Krylow et al.]; it agrees with that to within 20%. In both models a gas temperature of 1000 - 1500 K in the source and in the first gap (PG-EG) is assumed, but temperature accommodation takes place quickly within the extraction aperture.

The MANITU data, however, show a much lower stripping fraction than the results of this standard calculation. One possibility for the large discrepancy might be that not all of the stripped ions can leave the accelerator, as the ion trajectories at the place where stripping occurs might not point towards the aperture. In this case, however, the stripping fraction should depend strongly on the beam optics which is not the case. On the other hand, a larger gas temperature in the accelerator can much better reproduce the data (see figure 96), but the reason for this larger temperature is not clear up to now. No accommodation, i.e. no gas collisions in the extraction apertures, is rather unlikely, but perhaps also beam heating of the gas within the extraction aperture takes place as it was observed in the neutralizer of the JET NBI system. This

Figure 96. Dependence of the average stripping losses on the source pressure for two consecutive pulses at MANITU. The pressure was changed during the pulse. E_{ex} 8 kV, E_0 28.6 kV, tank pressure 1x10-5 mbar. Also shown are the calculated stripping fractions with a simple model for a source gas temperature of 1500 K, gas temperatures in the extraction aperture of 300 K and 1500 K, and a gas temperature of 1500 K in the whole accelerator.

might also to some extent explain the shape stripping loss profiles shown in figure 95: less beam power at the edges of the beam corresponds to lower gas temperature in the extraction apertures and thus to larger stripping fractions.
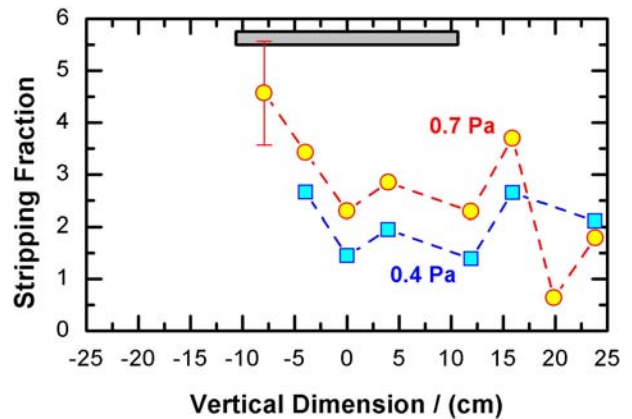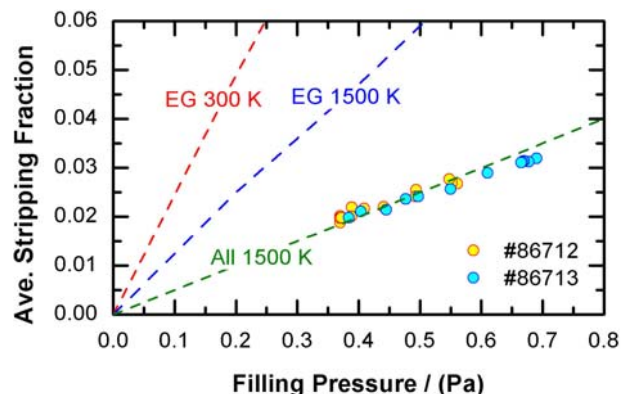
4.5 Asymmetric Beam Extraction with Different Direction of the Plasma Drift

4.5.1 Background

In the long pulse RF source the plasma drift caused by the magnetic filter field leads to different plasma parameters close to the top and bottom halves of the plasma. If the horizontal magnetic field was sufficiently strong, the plasma drifted in vertical direction resulting in different plasma densities on the two halves of the plasma grid. Probe measurement showed that the plasma at the side with low density consists mainly of negative ions with only a small electron fraction. It was observed by Doppler shift measurements that the divergence of the beam extracted from the top and bottom halves of the extraction system was also different for some filter field configurations (see section 4.1.4). In most cases the divergence on the side with lower plasma density was smaller. As the beam extraction is normally underperveant, the measured lower divergence would indicate that the H⁻ current density was closer to the perveance optimum and hence higher than on the other grid half.

For further source development it is important to find out whether the plasma density profile is asymmetric, do the two grid halves contribute differently to the total H⁻ current? Therefore, one half of the grid was masked and only half was used for the beam extraction. By changing the polarity of the filter field the direction of the plasma drift inverted.

The experiments were carried out in pulses of 100 s – 500 s length. An advantage of long pulses is that parameter scans can be performed within one pulse and in this way a minimum of change of the other parameters is achieved.

4.5.2 Extraction with the Top Grid Halve Only

In order to investigate the effect of the plasma density on the extracted currents, the bottom grid halve was covered and the direction of the drift was converted by changing the polarity of the magnets. The bottom half was masked by a water cooled copper plate (see figure 97). On the top half the part outside the projection of the driver was covered as in previous experiments and so the total extraction area was reduced to 65 cm^2.

The plasma homogeneity was measured by H$_\beta$ spectroscopy in two lines of sight (LOS) of 1 cm diameter in 2.5 cm distance from the plasma grid on both sides at the lower and uppermost positions (see figure 97). Because the cover of the bottom grid halve reaches 1 – 2 cm into the source, the plasma is also shifted into the source and hence on the bottom half the plasma density in the LOS of H$_\beta$ is expected to be lower compared to the top side even without drift.

Another reason for asymmetries of the source plasma

Figure 97. Partly covered plasma grid with the LOS of the Hß spectroscopy

76

is related to the position of the Cesium oven. Because it is mounted at the top of the source back plate the upper part of the plasma grid has a high deposition rate, which may cause differences in the plasma parameters, the H- production and the electron currents between top and bottom.

4.5.3   New Position of the Magnetic Filter Field

For the experiments it was necessary to change the polarity of the filter field without open-ing the source in order to avoid restarting the

Figure 98: Effect of the change of the filter field polarity on the source performance and symmetry.

conditioning procedure again. The internal filter magnets were removed and mounted outside the source on top of the diagnostic flange at a distance of 9 cm from the plasma grid with a similar flexible magnet frame like that for BATMAN, but without the possibility for moving the filter field across the source. The field strength can now be adjusted by the number of magnets and the polarity can be changed by turning the magnet pack. However, the maximum of the B field is now shifted further away from the plasma grid and the B field on the plasma grid is reduced to about 0.4 mT which is less than half the previous strength (see figure 4). The field integrated in the driver direction is considerably higher with the same number of magnets (see table 1). This set-up had been tested successfully in short pulses on the smaller test facility Batman. In the experiments described below only the configuration with 2x3 rows of magnets was used which has almost the same integrated B-field as the standard field.

Another reason for asymmetries of the source plasma is related to the position of the Cesium oven. Because it is mounted at the top of the source back plate the upper part of the plasma grid has a high deposition rate, which may cause differences in the plasma parame-ters, the H⁻ production and the electron currents between top and bottom.

4.5.4   Results

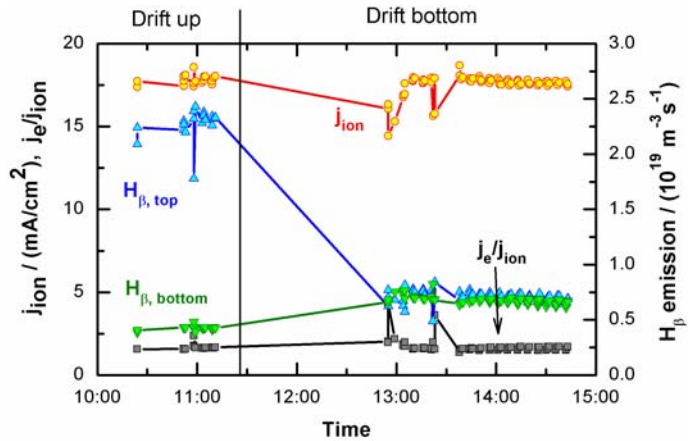The H_β signals showed that in case of the drift upwards the plasma density was indeed
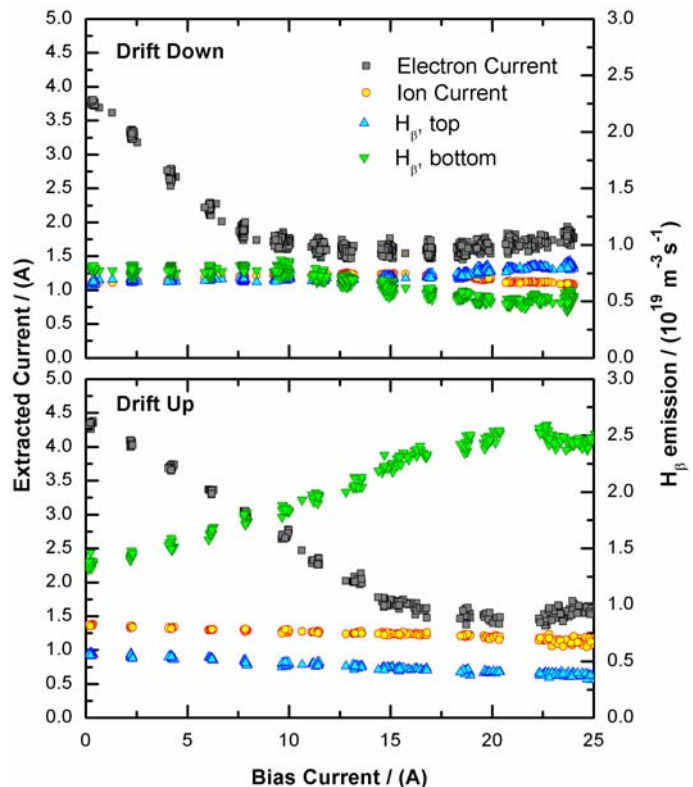

Figure 99: Extracted ion and electron current and top and bottom H_β signals measured at 50 kW RF power and 0.4 Pa. for different filter field polarity and plasma drifts.

much higher at the top than at the bottom position. When the polarity of the magnets was changed the measured value at the top decreased rapidly but the bottom signal did not increase in the same extend. This may be caused by the small distance between the bottom LOS and the cover of the bottom grid halve. Surprisingly no change of the ion and electron currents was observed (figure 98).

The dependence of the $H_ß$ intensities on the bias current was very similar for both drift directions; raising the bias current increased the $H_ß$ signal at the side, where the drift is directed to, and decreased it at the opposite side (see figure 99). This corresponds to an enhancement of the drift by a higher bias voltage.

Figure 100: Extracted ion and electron currents and as a function of the RF power at 0.4 Pa for drift up and drift down of the source plasma.

The ion current and the co-extracted electron current, however, are not very much affected by the direction of the drift. There was, in particular, no correlation between the currents of co-extracted electrons and the $H_ß$ intensities as a function of the bias current. With drift upwards a slightly higher bias current was necessary to suppress the electron current and the ion current was higher at low bias voltage.

When the bias current was adjusted such that the electron current was minimal, there was no significant change in the ion and electron currents observed when the polarity of the magnets was changed. The assumption that one grid halve would deliver a higher H^- current could not be confirmed by these experiments.

This was also valid at different power. The difference of the extracted currents as a function of the RF power for both polarities shown in figure 100 is not significant, when the bias current was optimized to suppress the electrons. The results are within the spread caused by different Cesium conditions on the plasma grid surface.

4.6 *Isotope Effects in Pumping Speed and Capacity of the Cryo Pumps*

The pumping speed and capacity of the MANITU cryo pumps for hydrogen and deuterium have been measured in July 2010 in collaboration with KIT as part of the F4E Grant F4E-2009-GRT-032.

The measurement have been performed by introducing gas with a high flow rate (80 mbar l/s) into the MANITU target tank until the pumping speed drops, i.e. until the pressure starts rapidly to increase.

Detailed data evaluation is presently under way by KIT. The raw results are shown in figure 101, which confirms the expectations:

o   The pumping speed is almost the same for hydrogen and deuterium.
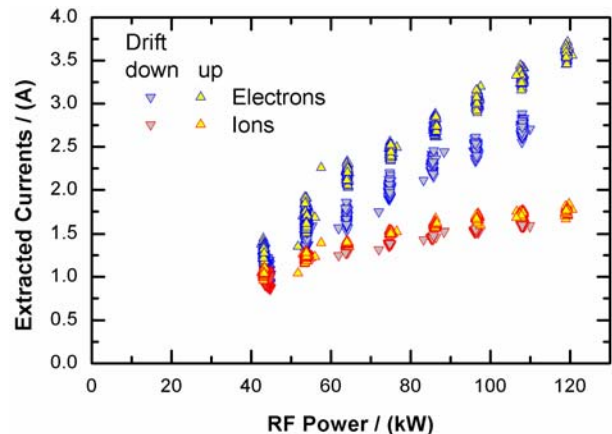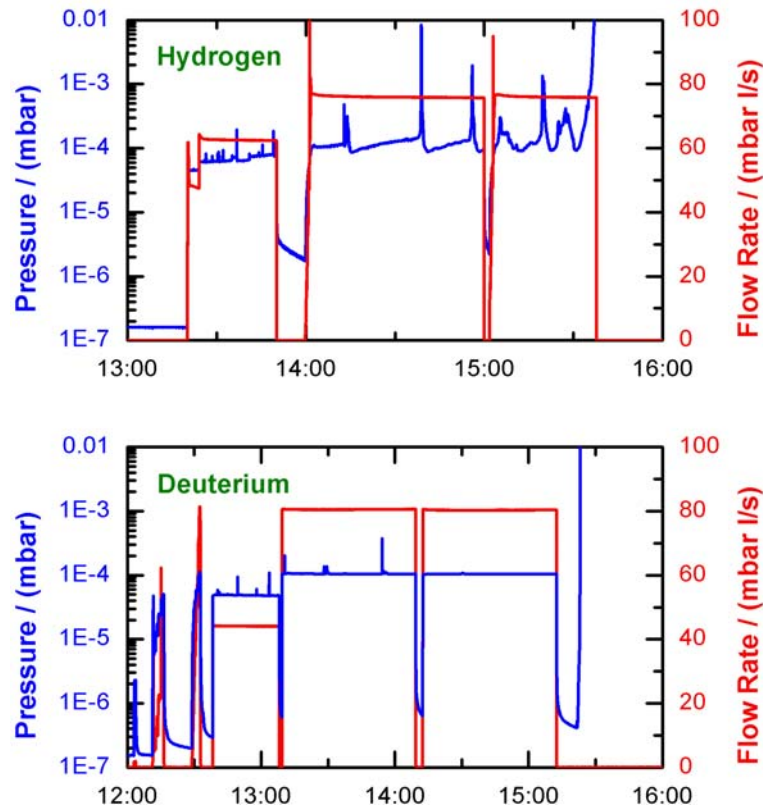
Figure 101: Pressure evolution in the MANITU target tank for hydrogen and deuterium.

o The pumping capacity for deuterium, however, is larger than for hydrogen. For deuterium, a loss of the pumping speed could not be observed; the increase of the pressure after the end of the gas inlet is due to the regeneration of the cryo pumps.

o Deuterium operation is much more stable than hydrogen operation; the frequent pressure spikes in the hydrogen case are presumably caused by gas redistribution processes within the cryo panels. This is more pronounced in hydrogen than in deuterium due to the larger mobility of hydrogen. The redistribution processes may also lead to the slow warming up of the panels, thus reducing the pumping speed. This can be seen in the slow increase of the pressure between the spikes.

4.7   Future Plans

Due to the shutdown of MANITU in April 2011, only limited time for experiments is available. Hence, the experiments will be concentrated on a few topics.

4.7.1   Filter field variations with asymmetric beam extraction

The water cooled cover of the bottom grid halve has been replaced by a thin Mo coated copper plate which is now directly fixed to the plasma grid in order to provide a good thermal conduction (see figure 102). Because this plate reaches only a few mm into the source the plasma symmetry is less affected as with the previously used plate. The cover is now on plasma grid potential. The experiments will be continued with different numbers of magnets in the external filter and changed polarities. It is of particular interest, if the di-

rection of the drift or the plasma density in front of the extraction area respectively affects the increase of the electron currents in long pulses.

4.7.2   Ni coating of the source backplate

After the back plate with the water leak has been repaired the long term test of the Nickel coating will be continued.

4.7.3   New position of the Cs oven

Raising the temperature of the Cs oven on the back plate increased the Cs852 line intensity, but had no impact on the electron and ion currents. The reason is that the evaporated Cesium is ionized and cannot reach the plasma grid.

In the next experimental campaign a second Cs oven will be mounted at the side on one of the feedthroughs of the diagnostic flange such that the nozzle is only 2.5 cm away from the extraction

Figure 102: New cover of the bottom grid halve.

plane. The assumption is that in this way much more of the Cs is not ionized and it will be possible to improve the Cs coverage of the plasma grid during long pulses.
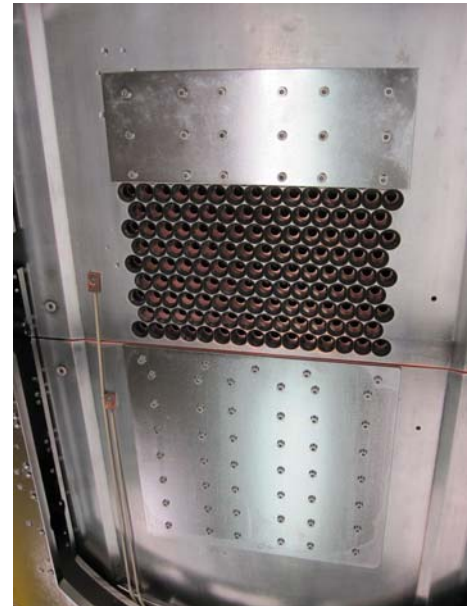
4.7.4   Deuterium Operation

The last experiments in Deuterium were started after a long Hydrogen campaign when the source performance started to degrade (see section 4.3.2). For a better comparison with Hydrogen the Deuterium operation will be continued after a complete cleaning of the source such that the Cs layer on the plasma grid is less poisoned by impurities.

5 Experiments at RADI (WBS 2.3)

The RADI test facility was re-commissioned after a year of break down due to the rebuild of the experimental hall for ELISE and — to a smaller extent — to a rebuild of the test facility. The latter includes the repair of the Faraday screens after they have been severely damaged in 2009 and the opening of the plasma grid in order to achieve the same grid conductance as for the ITER source.

The RF matching circuit has been improved so that now ignition is possible also at good matching without the necessity to change the capacitance of the serial capacitor during the pulse.

Also tests of various components and design choices for ELISE and the ITER ion source have been performed.

5.1 Faraday Screen Operation

During the course of the experiments in fall 2008 / winter 2009 the Faraday screens have been severely damaged by reasons that are not really known up to now. Figure 103 shows a photograph of the inner surfaces of the Faraday screen. The damage is much localized: two fingers are molten together, whereas the fingers nearby are almost unaffected.

These damages have been accompanied (and identified) by a large release of copper into the source, measured even with the overview spectrometer which is not very sensitive to copper and causing a re-covering of all source surfaces, also the dummy plasma grid, with copper.

Figure 103: RADI Faraday screen with damaged fingers. The inner surfaces were covered previously with Mo.

Up to now, no clear correlation of these severe Cu events with operational scenarios has been found, also because of the small number of these events, making statistics problematic. Furthermore, there is no explanation of the localized nature of the damage at the Faraday screens. It seems that the events occur for conditions with low pressure, high power, bad matching and increased Cu or impurity content. There are, however, a lot of pulses at these conditions with no damage or increased copper emission at all. Bad matching operation at high power occurs at RADI routinely, as due to still unknown reasons plasma ignition is only established for poor matching conditions ($\cos \varphi \leq \sim 0.5$). After ignition, the series capacitance is then changed by the control system to achieve better matching.

The level of damage depended also on the position of the screens: the Faraday screen of the upper pair was more damaged than the lower ones, as well as the Faraday screen 'near' to the series capacitance (C_2) where the RF voltage drop is larger.

In order to resolve the problem and to find the causes, the RF circuit of RADI was rebuild for 1 driver / 1 generator operation, as it is the case for BATMAN and MANITU, where such damages not occurred. The Faraday screens have been repaired, but have now a copper surface. The upper pair of drivers was chosen. The copper emission in the source, near the dummy plasma grid, can now be measured both with the in-sensitive overview spectrometer as well as — in one sight of line through one driver — with a high resolution Echelle spectrometer.

Also during this 1/1 operation, some (smaller) emissions of copper occurred (in total 4 pulses out of several hundreds); again these events are correlated with low pressure and bad matching operation at high power, but also with a certain copper content in the drivers.

The 1/1 operation showed also, that the drivers are influencing each other: the matching characteristics changed for each circuit, when both drivers run simul-taneously. This mutual influence could be prevented by introducing a copper plate between the drivers that shields the magnetic fields.

Figure 104: Line emission of atomic copper at 555 nm in dependence on the source filling pressure, normalized to the Hγ emission for one of the driv-ers at RADI (lower right), both for Hydrogen and Deuterium operation, with and without magnetic filter field. RF power was 2x80 kW.

Finally, another severe damage of one of the Faraday screens — the predamaged one — in 1/1 op-eration occurred; this indicates that the problems are not caused by the 2/1 operation, but most probably by (unknown) particularities of the RADI matching circuit, we switched back to 2/1 operation for all four drivers. In order to gain more insight in the processes leading to the damages, we deliberately imposed defects to 2 of the four Faraday screens: on the one hand one of the fingers of one Faraday screen was bent by about 1 cm into the plasma, on the other hand two fingers of another Faraday screen are weld together, as some kind of nuclei for further damages.

No damage, however, occurred so far up to now, also a large number of pulses have been performed (also the pulses for the experiments discussed in sections 5.3 and 0). Some copper could be measured (see for example figure 104), but only one small remarkable release of copper at the end of one pulse at 120 kW and 0.4 Pa filling pressure occurred. This happened again at the predamaged and repaired Faraday screen.

Figure 104 shows that the copper content in the driver plasma is relatively large and increases with decreasing pressure. There is some dependence on the magnetic field, but different for hydrogen and deute-rium. But anyway, this figures shows again the necessity for coating the Faraday screens (and other parts of the source) with high-Z materials.
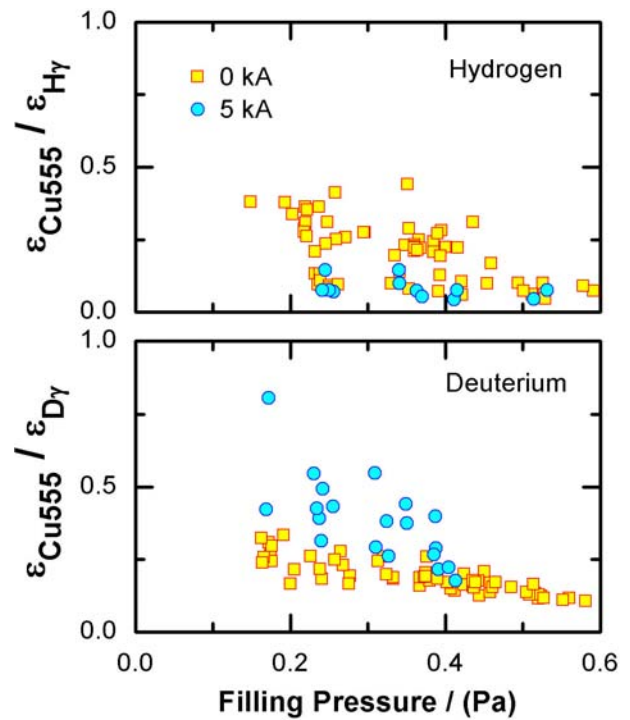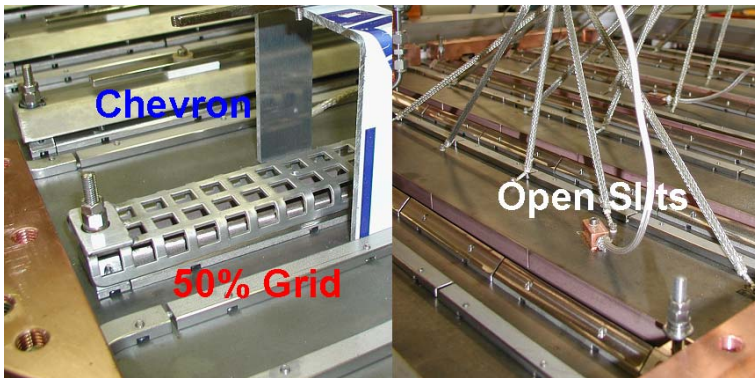
Figure 105: Views onto the dummy plasma grid from the down-stream side with the three different slits.
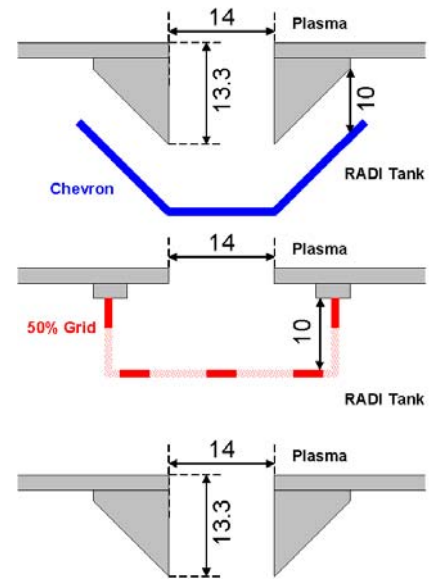

Figure 106: Sketches of the three different slit geometries. Top: Chevron. Middle: 50% Grid. Bottom: Open slits.

5.2 Dummy Grid Conductance

As the occurrence of the Faraday screen damage seemed to correlate somehow with low pressure operation, the conductance of the plasma dummy was re-checked. It turned out, that the conductance of the setup with the chevron, which was used since the start of the RADI operation, was rather small, so as the gas flow per driver, much less than for the ITER grid. This underestimation had several reasons:

- the conductance of the chevron geometry was calculated with too simple formulas;

- the flow measurement was erroneous due to a wrong calibration;

- the pressure measurements were partly erroneous due to a calibration fault of one Baratron (happened at the company), but also faults in the data acquisition system.

All the measurements have been re-checked and re-calibrated again, by letting in fixed amounts of gas with closed source valve, so that stationary conditions could be achieved. Furthermore, a sixth Baratron — additional to the four Baratrons for each driver and the source Baratron — was installed downstream of the dummy plasma grid for a thorough evaluation of the grid conductance. This was necessary as due to the limited pumping speed at RADI the downstream pressure is rather high and cannot be neglected.

The conductance of the dummy grid was increased in two steps: Figure 105 and figure 106 show photographs and sketches, respectively, of the three different 'slit' geometries that have been used. To re-
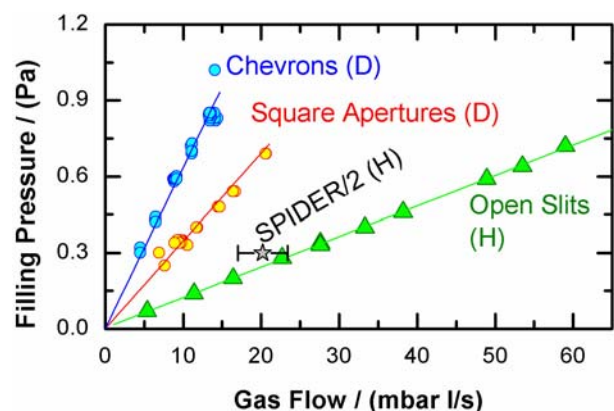

Figure 107: RADI filling pressure in dependence of the gas flow for the three different slit geometries. The star denotes the corresponding value for SPIDER, scaled with the grid size. (D) denotes deuterium operation, (H) hydrogen.

member, the RADI dummy grid has five rectangular, long slits with dimensions of 800x14 mm^2. The "50% Grid" version had a grid like structure installed for some limitation of the conductance, the "Open Slits" version has fully opened slits, but again with the guiding cones attached. The conductance of the "Open Slits" version was measured now with the recalibrated system to be around 12200 l/s in total for hydrogen, which agrees very well with calculations with the ITERVAK Monte Carlo model (12275 l/s), which have been performed by KIT Karlsruhe. This is slightly larger than the conductance of the SPIDER grid system[3] (about 8400 l/s), but due to the differences of the tank pressure similar gas flow is needed for a given filling pressure.

This is indicated in figure 107, showing the dependence of the filling pressure on the gas flow for the three different dummy grid geometries. It can be seen, that with the open slit geometry the SPIDER scenario is achieved: about 17 to 23 mbar l/s (scaled by 2 in order to account for the size ratio) for a filling pressure of 0.3 Pa, according to a flow rate of about 5 mbar l/s per driver. For comparison, the present flow rates of BATMAN (extraction area of 63 cm^2) and MANITU (extraction area of 200 cm^2) in hydrogen for a filling pressure of 0.3 Pa are 2.7 mbar l/s and 5.9 mbar l/s, respectively[4].

Some RF experiments with 2 drivers per generator have been done with the "50% grid" version, but also here some damage of the Faraday screens occurred. Hence, the low gas flow operation seems not to be the (sole?) reason for the damages.

5.3 Plasma Ignition at Good Matching

After some improvement of the RF system, plasma ignition is now possible also at good matching and high power. This is shown in figure 108; no change of the power (stepwise increase) or the parallel capacitance as it was done before was needed. Also the stability of the RF circuits was improved considerably: now it is possible to start the plasma after longer pauses (like at the next day) without a change of the capacitors, as it is the case for BATMAN and MANITU.

The improvement consisted of several measures — introducing a 1:2 transformer, improvement of the
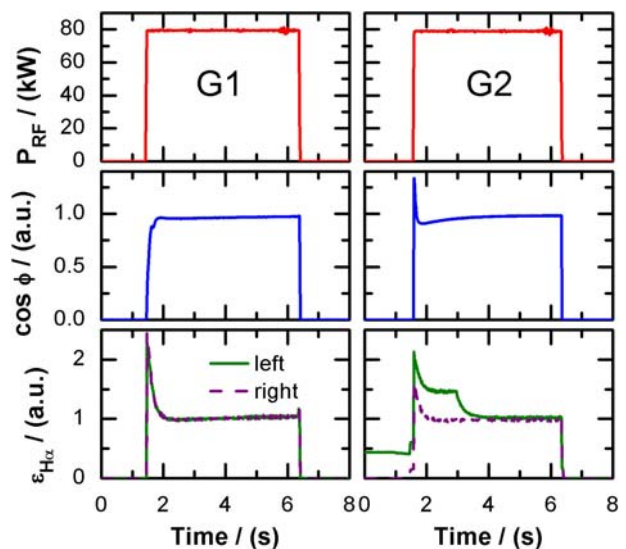

Figure 108: RADI pulse with plasma ignition at good matching (cos φ > 0.95) for both generators. Deuterium, 0.3 Pa filling pressure, no filter field. The Hα emission in the left driver of G2 is superimposed by emission from the starter filament, which is switched off at 3 s.

---

[3] S. DalBello, SPIDER Design Review Meeting, Padova, 02/07/2008. The gas flow for SPIDER depends on the tank pressure assumed. The total gas flow for the ITER source (8 drivers) is 36 mbar l/s for hydrogen, i.e. 4.5 mbar l/s per driver.

[4] The measured flow rates for BATMAN and MANITU do not scale with the extraction area, but they have to, as the aperture geometry is the same; the reason for the difference is still not clear. The tank pressure in both test facilities is much lower than the filling pressure and can be neglected.

mounting of the output transformer in the RF generator, replacement of both tunable parallel capacitors by fixed one — but it is still not clear, what individual component caused the improvement. But a thorough check of one of the tunable series capacitors showed that this had a limited voltage holding capability caused by a small vacuum leak. As it is not clear when the leak evolves, it might be possible that the problems with matching are caused by the malfunction of this particular capacitor. Consequently, the other tunable series capacitor will now also be checked.

5.4   Tests of ELISE Components and Design Choices

5.4.1   Driver Efficiency with PG Return Conductors Nearby

In order to reduce the magnetic filter field in the accelerator and to enhance the filter field in front of the plasma grid, it is foreseen for ELISE and SPIDER to run the PG current return conductors near the drivers. The experiments at BATMAN, however, indicated problems with plasma sustainment when the magnet frame was near the driver (see section 3.1.3). Hence dedicated experiments where performed at RADI with the PG current return conductors in the vicinity of the drivers, similar as it is foreseen in ELISE and SPIDER
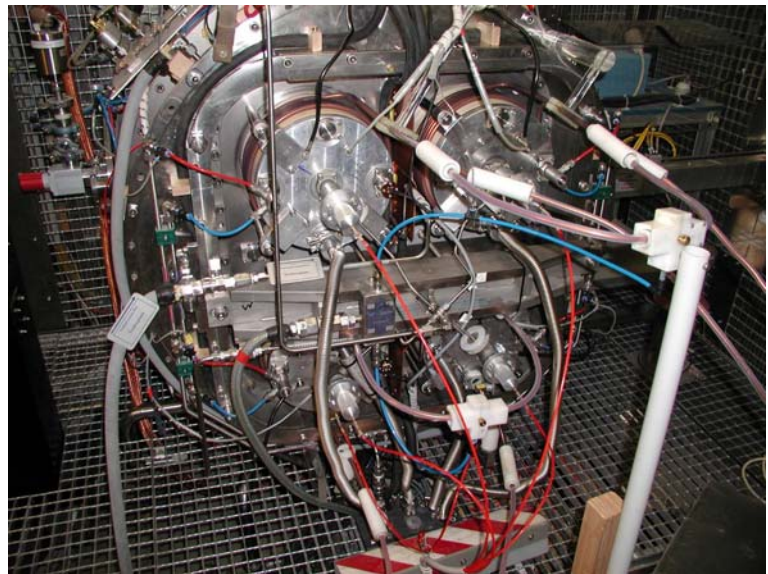

Figure 109: Picture of the RADI drivers with the PG current conductors (thick black cables).

(see figure 109). The respective filter fields are shown in figure 110, also compared with the BATMAN filter fields. The corresponding 2D field maps are shown in appendix 9.2.9.

The result of these experiments are shown in Figure 111: there is almost no difference in the driver efficiency (expressed here by the H_α light emission from a central axial line-of-sight through ach driver), both for hydrogen and for deuterium operation. Stable RF operation is possible down to a filling pressure around 0.2 Pa. If at all, slight differences can be seen for higher source filling pressures: there is a slight increase of the driver light emission with filter field. Of course the standard effect of the filter field can be seen on the plasma expansion in the source body: with filter
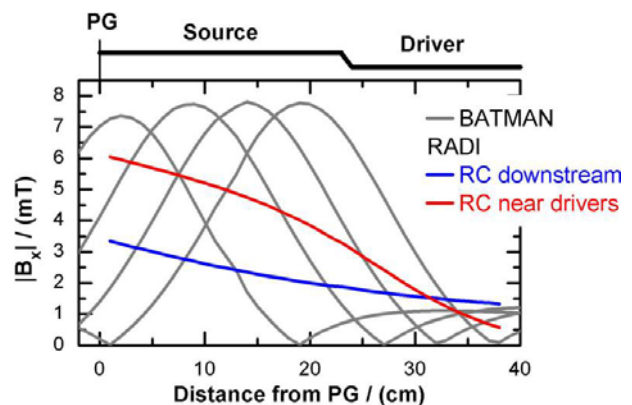

Figure 110:   Horizontal filter field component for RADI with different positions of the return conductors in comparison to the BATMAN case with different positions of the magnet frame (see also figure 4).
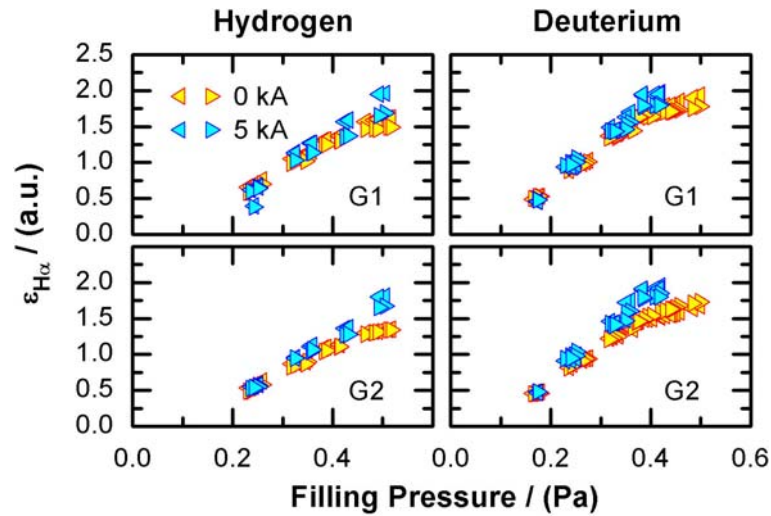
Figure 111: Driver efficiency at RADI (expressed by the central H_α light emission) with and w/o magnetic filter field for hydrogen and deuterium, respectively. 2x80 kW RF power.

field the plasma emission and the ion saturation currents at the dummy plasma grid are reduced by a factor of 2.

5.4.2　ELISE RF circuit

The ELISE RF circuit has two major differences to the SPIDER circuits:

- An RF transformer is mandatory as the RF generators are on ground potential. This transformer will consist of 3 legs with 40 low-μ Ferrites (μ = 1600) with a Curie temperature of 240° at each leg. The design is flexible for all combinations (1:3, 1:2, 1:1).

- In order to improve the flexibility and the maintenance of ELISE, the RF connection between the two drivers within one circuit is done outside the dome in air. Hence, this lengthy connection (80 cm instead of a few cm) affects the matching of the circuit due to the increased inductivity.

The lengthy driver connection was tested at RADI: there was as expected a slight change in matching, but no other problems occurred.

The full RF test of the ELISE transformer is still pending as the manufacturing of a prototype is ongoing. Meanwhile, HV tests have been successfully performed using just one leg; also a first crude measurement of the temperature increase of the foreseen ferrites has been made.

5.4.3　Source Video Camera

In the ion source for ELISE, a port at the corner is foreseen for video imaging of the expansion and extraction during a plasma pulse. Also the exit of all drivers can be seen.

As a test of the RF hardness, the software and the usefulness of such a system, a video camera was installed at RADI. The system is working well; no influence of the RF can be seen. Figure 112 demonstrates
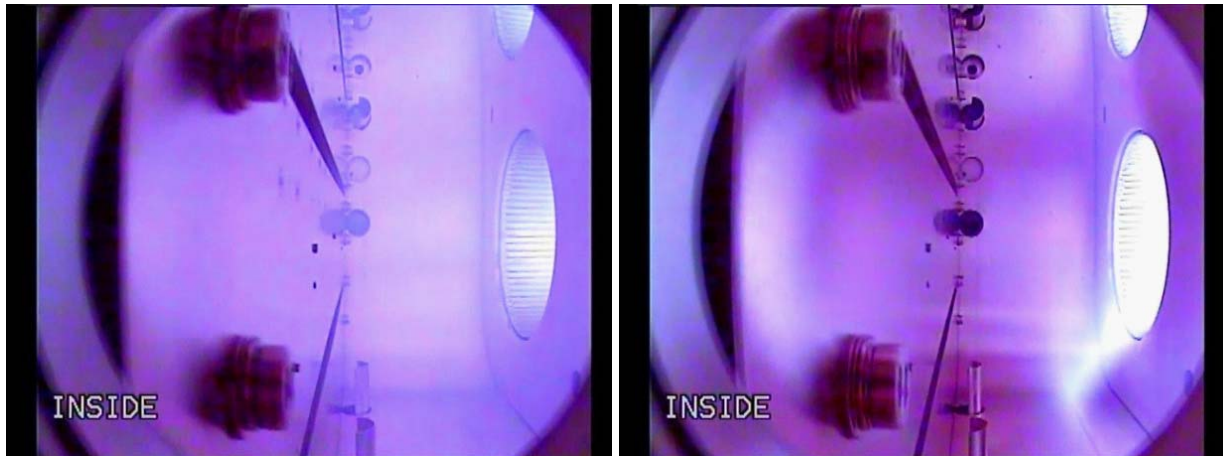
Figure 112: Video snapshot from RADI pulses. Camera position top left, vertical view. 4x40 kW, 0.3 Pa. Left: w/o magnetic filter field. Right: with magnetic filter field (5 kA PG current), return conductors near driver.

also its usefulness: it shows a snapshot of videos with and without magnetic filter field; clearly the influence of the magnetic filter field on the plasma distribution within the source can be seen.

5.5   Future Plans

Due to the operational problems mentioned above, not all of the foreseen tasks and experiment could be performed in the present contract. On the other hand, some new experiments and tests have been performed, which evolved from the present design and procurement activities of ELISE and SPIDER.

The RF measurements with RFX Padua will be performed in January 2011, as part of the F4E contract F4E-2009-GRT-032. Planned is a visit of 3 weeks. These measurements also include measurements at RADI w/o transformer, as it is foreseen in SPIDER / MITICA / ITER.

Still pending are:

- measurements of the plasma homogeneity with Cs

- tests of the ELISE transformer

- tests of the ELISE PG current bus bar

As the experimental time is rather limited until the final shutdown in April 2011, priority is laid on tests and experiments important for the design and operation of ELISE and SPIDER.

6   Diagnostic Development (WBS 3.0)

6.1   Laser Detachment at RADI

Laser photo detachment allows local measurements of the negative hydrogen ion density. The local character of the results is the main advantage of this technique over other diagnostics methods like cavity ring down spectroscopy or optical emission spectroscopy. The results of the latter methods are integrated over the used line of sight. Thus, laser photo detachment is of particular importance to determine the homogeneity of the negative ion density in large ion sources like RADI or ELISE.

The operational setup for the planned laser detachment measurements at RADI consists of a Nd:YAG laser with a maximum pulse energy of 300 mJ at a wavelength of 1064 nm (Innolas Spitlight 300). The laser light is guided by a waveguide into the plasma volume in which the negative ion density is to be measured. Since the used laser is a class 4 laser, the wave guide has to be encased and supervised by an interlock system. The electron saturation current at any point along the way of the laser beam through the plasma volume can be measured by a positively biased Langmuir probe. Due to the high laser energy, all negative hydrogen ions along its line of sight are detached, i.e. electron-atom pairs are created. Due to the much higher mobility of the additionally created electrons compared to negative ions, the saturation current measured by the probe increases shortly after the laser pulse and then shows a characteristic behavior over time, determined by the flux of different charged particles in and out the plasma volume penetrated by the laser beam. From the ratio of the electron saturation current before and directly after the laser pulse the negative hydrogen density can be determined.

At the test bed BATMAN the principle applicability of laser detachment measurements at the IPP negative ion source prototypes has been demonstrated previously within the scope of a PhD thesis. One major problem which was solved was the interference of the RF with the diagnostics by coupling into the measuring setup. Now, it was started to move the complete setup to RADI.

The installation of the laser detachment setup at RADI is divided into two parts: first, the laser system was moved from BATMAN to RADI. The installation of the encased waveguide system and the interlocks is nearly finished.

The second part of preparing the experimental setup is the commissioning of the Langmuir probe at RADI: the probe hardware was successfully installed and first tests were performed in hydrogen and deuterium plasmas, in each case with and without the magnetic filter field created by a current of I_{PG}=5 kA flowing
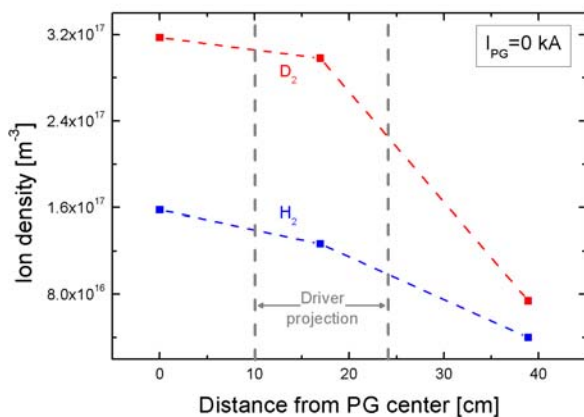
Figure 113: Profiles of the positive ion density in RADI measured for hydrogen and deuterium using the Langmuir probe system. The dashed lines are drawn to guide the eye.

through the dummy grid. The probe is aligned in horizontal direction and located at one of the vertical faces of the source body, in the center between the upper and the lower pair of drivers. Due to the limited length of the movable part of the probe, horizontal profiles of the plasma parameters can be taken from the wall to approximately the center of the ion source only. Figure 113 shows, as example, profiles of the electron density for hydrogen and deuterium. All four drivers were active during these pulses, with P_{RF}=40 kW each and the filling pressure was 0.4 Pa. The electron density is at maximum in the center of the source and decreases to lower values towards the walls. This result is caused by the overlap of the plasma generated in the four drivers:

Figure 114: Normalized EEDF measured in RADI without and with a magnetic filter field using the Langmuir probe system

in the center this overlap is large and at the walls it is small. Close to the walls the electron density is additionally decreased by losses of electrons to the surface. This confirms the hydrogen results reported in the final report of the EFDA task TW6-THHN-RFSD4. The electron density in deuterium is almost twice as large as in hydrogen. This result is in agreement with results of the optical emission spectroscopy, which observed much higher emissivities in deuterium than in hydrogen.

Figure 114 shows probe characteristics measured with and without the magnetic filter field in deuterium. The electron temperature is decreased drastically by the filter, from 6.5 eV to 1.0 eV. The latter value is comparable to the electron temperatures measured in the small test facilities BATMAN and MANITU close to the plasma grid. This finding affirms the applicability of the current generated magnetic filter for cooling the electrons.

With the conducted measurements the installation and the testing of the Langmuir probe system is finished. As next step the laser system will be put into operation and tested. The final goal then is the combined operation of laser and probe for laser detachment measurements.

6.2 OES & Cs Monitor MANITU

The work function of thin cesium layers on metal surfaces and thus the yield for surface production of negative hydrogen ions is strongly affected by even very small amounts of impurities like hydrogen, oxygen or copper. Due to the good thermal conductivity, all inner surfaces of the ion source prototypes consist of copper which can be released from the walls by sputtering.

A copper monitor based on a high resolution spectrometer is attached now as standard diagnostic tool at the long pulse test facility MANITU. During previous campaigns with a full copper source, a small but non-transient copper amount was detected in the ion source. This copper amount had a correlation with the temporal evolution of the extracted negative hydrogen ion and electron currents: long pulse operation of the
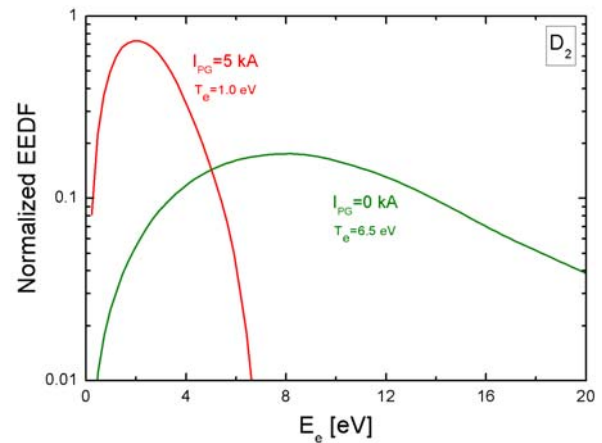
source was difficult since the currents were not stable; especially the current of co-extracted electrons typically showed a strong increase over the duration of the pulse.

In 2008 and 2009 the Faraday screen, the plasma grid and bias plate, the source and driver back plates and the cone around the driver exit were covered with a thin layer of molybdenum (see section 4.1.3). Compared to copper, for molybdenum the yield for sputtering by hydrogen as well as for self sputtering is significantly lower. No molybdenum is detected by OES in the plasma and the copper amount is now strongly reduced to a barely detectable amount. The extracted negative ion and electron currents are much

Figure 115: Correlation of the cesium signal with the temperature increase of the cesium oven during a pulse. Corresponding extracted negative ion and electron current densities are also shown.

more stable over time than before. Stable and reproducible pulses over several hundreds of seconds are possible now (see also section 4.3).

An additional improvement of the source stability and performance (increase of the ion current, further stabilization or even suppression of the electron current) is expected by a cesium monitor that measures the cesium amount in the source volume. The final goal was that, via a feed back control, the temperature of the cesium oven can be controlled and adjusted to optimize the cesium amount on the walls and thus the performance of the ion source.

A first step in the development of a cesium monitor is learning how to influence the source performance by means of regulating the cesium influx. A dedicated experimental campaign was conducted to investigate the relationship of cesium oven temperature, cesium radiation in front of the plasma grid and the source efficiency.
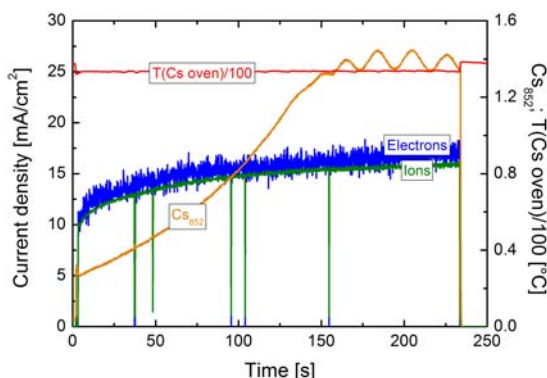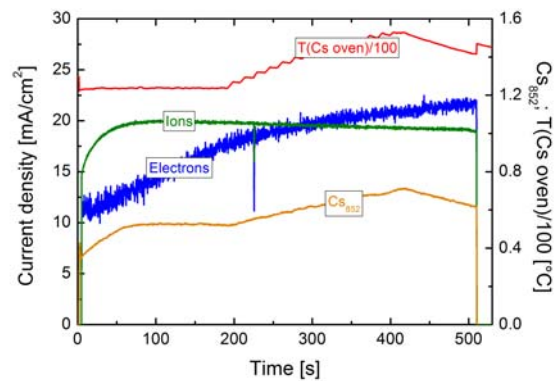

Figure 116: Cesium diode signal for a pulse with stable temperature of the cesium oven and the corresponding extracted negative ion and electron current densities.

A diode attached to a vertical line-of-sight parallel to the grid surface (distance from the PG: 0.7 cm) was chosen to measure the radiation of the cesium line at 852 nm which is proportional to the cesium density, the electron density and additionally depends on the electron temperature. Results of this measurement are not necessarily proportional to the status of the cesium conditioning: the cesium amount in the plasma volume is a superposition of cesium fluxes directly from the oven, from the PG surface and from the other surfaces of the ion source. Additionally, although 99 % of the cesium is ionized, only neutral cesium can be detected

(the intensity of the emission lines in the ion is too small). Thus, no conclusion is possible whether the cesium layer is thicker or thinner than the optimum layer using solely the information from OES. The source performance can be identified simply by the extracted negative ion and electron currents.

Figure 115 shows the cesium signal (in arbitrary units) of a pulse with a length of 500 seconds. After around 200 seconds the temperature of the cesium oven was stepwise increased from 124 °C to 153 °C. The measured cesium radiation directly follows the cesium oven temperature, reflecting an immediate influence on the cesium amount in the vicinity of the extraction apertures of the increased evaporation rate of the oven.
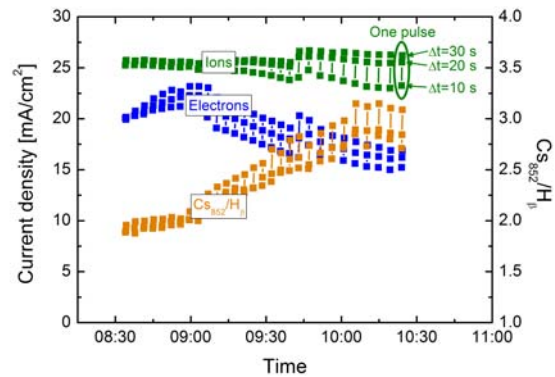

Figure 117: cesium signal for series of 29 pulses and the corresponding extracted negative ion and electron current density. For each signal three points per pulse are shown: ten seconds after the beginning of the pulse (Δt=10 s), at Δt=20 s and Δt=30 s.

Also shown are the extracted negative ion current density and the co-extracted electron current density. Both currents show the typical behavior of the ion source with molybdenum coated walls: while the ion current is perfectly stable after about 70 seconds, the electron current increases during the pulse. There is some indication that the slope of the increase decreases at around 200 seconds which may be caused by the increase of cesium at that time.

An in principle similar behavior of the ion source can be seen in figure 116: the same signals are shown as in figure 115 but for constant temperature of the cesium oven. The cesium signal strongly increases during the pulse due to heating up of source components; this is most probably the bias plate as it is in contrast to the source walls not temperature controlled. Even the observed strong increase of the cesium signal (by around a factor 5, which is huge) does not significantly influence the temporal evolution of the extracted currents. The oscillation of the Cs signal after around 150 seconds is not understood yet; it is not due to oscillations of the Cs oven temperature.

Figure 115 as well as figure 116 shows results of a well cesium conditioned source. It seems – at least up to now – that for this source condition it is not possible to systematically control the extracted currents during a pulse by regulating the cesium influx when the ion current is stable.

However, even for a well conditioned source, the fraction of co-extracted electrons as well as the temporal evolution of the negative hydrogen ion current in the first few tens of seconds of a pulse depends on the Cs conditions in the source. Figure 117 shows as an example the cesium signal as well as the extracted current densities of ions and electrons for a period of 29 almost identical pulses with a constant pause between them. The cesium signal is normalized to the H_β Balmer radiation (measured with a second diode) to eliminate – as far as possible – the influence of changes in the electron density. The cesium amount in the source volume was steadily increased during the examined period. The small jump in the ion and electron currents at 9:43 is caused by changing the bias voltage.

The extracted current densities of ions and electrons show the typical different behavior: while the electron current decreases with increasing cesium signal, the ion current has already reached some kind of maximum value. However, an increase in the cesium does not increase the ion current but the time dependence of the current during the single pulses: as can be seen in Figure 115 and Figure 116, during a pulse the extracted ion current starts at a relatively low value and needs some ten seconds to reach a stable value. This stable value at some tens of seconds is constant but the initial current density at the beginning of the pulse decreases with increasing cesium signal.

For a more detailed investigation of this effect, the dependence of this ion current increase during the first 40 seconds of the pulse (expressed as the difference of the ion current densities at 40 and 10 seconds) on the Cs signal is shown in figure 118. Results are shown for a large number of pulses during conditioning phases in hydrogen as well as in deuterium. The pulses are not the same as in figure 117.

It can be clearly seen, that the increase of the ion current density depends more or less linearly on the neutral cesium emission near the plasma grid. In deuterium operation this increase is much smaller than in hydrogen operation. The reason for this result (isotope effect, different source conditioning, or a change of Cs emission due to different plasma parameters) is still not known yet and part of the ongoing data evaluation. The few pulses which do not follow the linearity are pulses with events which change the conditioning of the ion source: extremely long pulses or extremely long breaks between two pulses. This, however, indicates also, that the Cs evaporation between the pulses has an influence on the source performance.

The initial ion current density of the first pulse after a long break (more than several minutes) is significantly lower than during normal operation. In contrast, the electron current density is very high, compared to the pulses before the break. A constant duty cycle with short breaks between the pulses is needed for a high, temporary stable ion and a low electron current density. Further investigations with a varied length of the break, to separate both introduced effects for the temporal evolution of the ion current density, are therefore under progress.

The described findings can be used for optimizing the operation of a well conditioned ion source: regulation of the cesium influx enables the operator to aim a compromise between low electron current and an ion current which is relatively stable and constant during the pulses.

As emphasized, all presented results have been obtained for a well conditioned source. Measurements made using Langmuir probes during the conditioning phase of the short pulse test facility BATMAN indicate that there is no correlation of the cesium signal with the extracted ion current densities for a volume production dominated source as well as for a very well conditioned
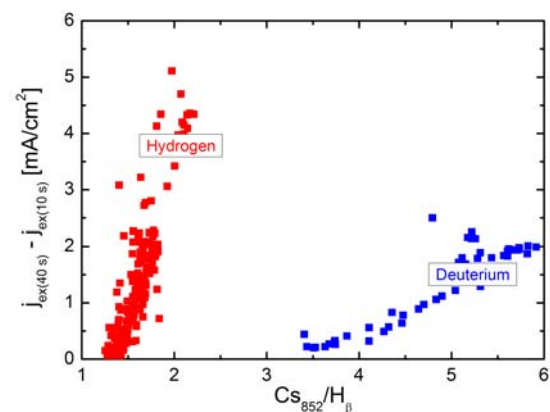

Figure 118: Increase on the extracted ion current during the first forty seconds of the pulse against the cesium signal (normalized to the Balmer line H_β) measured by OES.
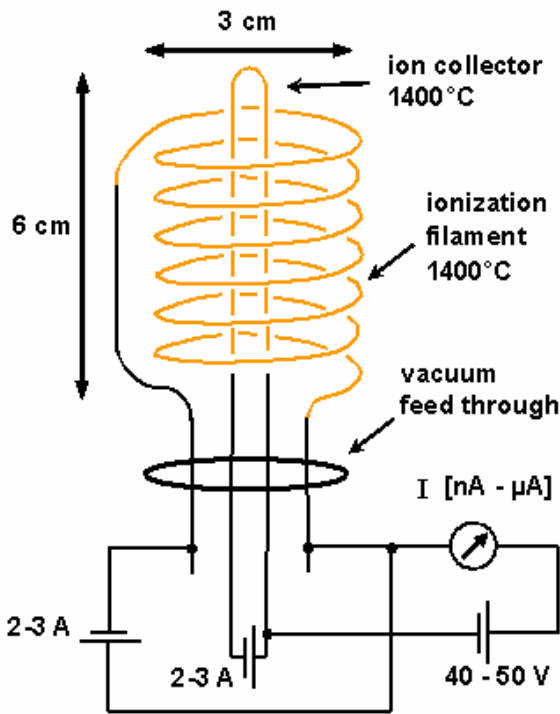
Figure 119: Schematic drawing of a Surface Ionization Detector (in use at university's lab).

source (the latter being in agreement with the present results). However, a correlation between cesium and both the ion and electron currents exists in the transition from pure volume production of negative ions to surface production. Obtaining optimum cesium conditions in this phase may be crucial for the optimizing the maximum ion current reached during the complete campaign. An ongoing experimental campaign of the cesium monitor focuses on this effect.

6.3 Surface Ion Detector

Stable and reproducible cesium evaporation is one of the main goals to obtain a homogenous and constant cesium layer on the plasma grid in the sources for negative hydrogen ions at the IPP. Therefore monitoring the cesium evaporation of the cesium ovens is indispensable and can be used to adjust the oven temperature by feed-back-control.

Diagnostics for cesium in the IPP sources (OES) have their lines of sight near the plasma grid to monitor cesium dynamics in front of the grid (see section 6.2) and are only useable during the plasma phase. For quantification of cesium during plasma and vacuum phases near the plasma grid laser absorption spectroscopy is going to be established (see section 6.4). But the amount of cesium in front of the grid is a consequence of adsorption, desorption and redistribution inside

the vacuum chamber of the expansion region between the driver and the plasma grid. To monitor the cesium evaporation directly at the cesium source, the cesium ovens, the applicability of a Surface Ionization Detector (SID) is being investigated. An option would be to mount the SID in front of the oven nozzle (therefore called oven SID) and to measure directly the cesium flux coming out of the oven. Thus the evaporation rate between pulses, i.e. in vacuum, can be controlled, which would moreover provide the opportunity to minimize cesium consumption. This potential of the oven SID is checked in laboratory experiments at the University of Augsburg, where many cesium diagnostics for the IPP sources are being developed (see laser
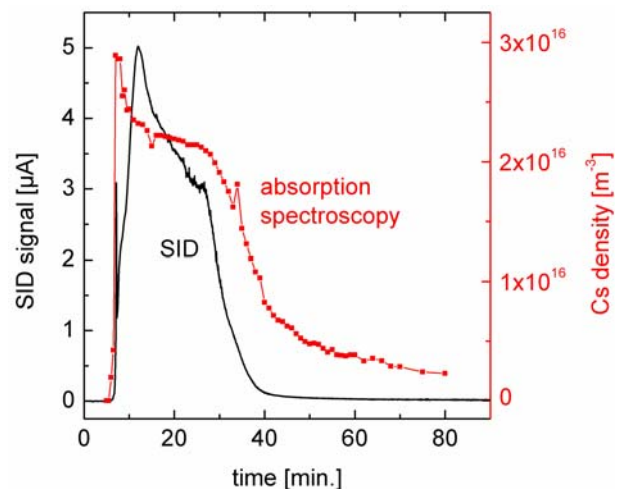

Figure 120: Comparison of methods to detect cesium from a cesium dispenser.

absorption). Also a local SID mounted inside the vacuum vessel is well-established at the university's lab.

A schematic drawing of a Surface Ionization Detector is shown in figure 119. The SID consists of two tungsten wires, where the so-called ionization filament is biased positive (40 to 50 V) against the so-called ion collector. Through each of them flows a heating current of some amperes (typical 2 to 3 A) so that they reach temperatures to about 1400 °C. Cesium contacting the ionization filament will be ionized — the work function of tungsten (4.6 eV) is higher than the ionization energy of cesium (3.9 eV) — and accelerated towards the ion collector. The current arising from the cesium ion hitting the second wire is measured (nA to µA) and should be proportional to the cesium flux on the first wire.

Such a device has been crosschecked against white light absorption spectroscopy (see figure 120) and has e.g. been used to investigate the evaporation of the IPP cesium ovens installed at the laboratory experiments at the University (see figure 121).

Figure 121: Cs evaporation rates of a cesium oven measured by the SID.

Figure 120 shows the typical evaporation of a $CsCrO_4$-dispenser from SAES measured by absorption spectroscopy and the SID. Both methods show quantitatively the same relative behavior; this demonstrates the usability of a SID to detect cesium (for absorption spectroscopy no correction factor for the line profile was applied). Figure 121 shows as an example measurements of the evaporation rate of a cesium oven used at IPP sources at different temperatures by the SID. Therefore, the SID signal was calibrated taking into account the geometry of the experimental setup and the evaporation characteristic of the oven nozzle [9].
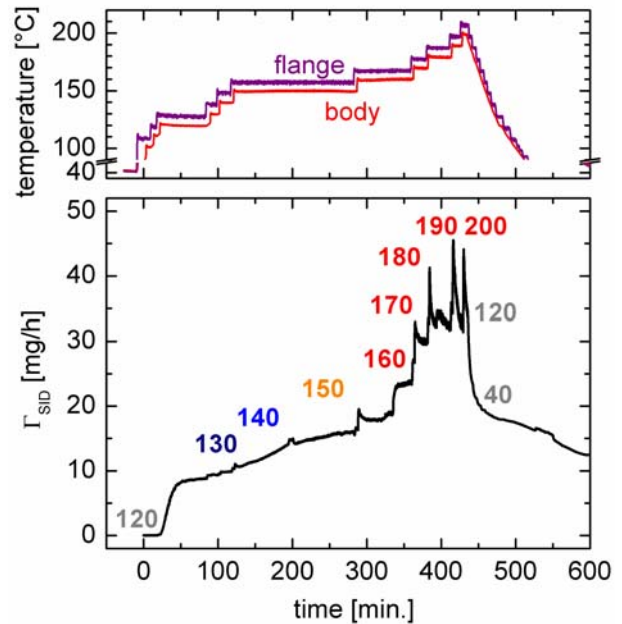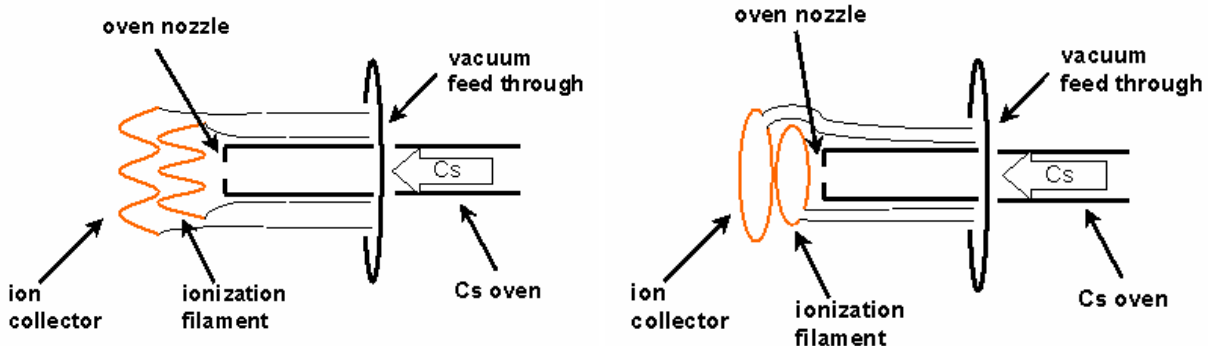
Figure 122: Sketches of different geometries for the oven SID.

Currently the oven SID is under investigation at the university's lab and is simultaneously compared to measurements with the established local SID. Several SID geometries, two of them shown in figure 122, are therefore being investigated.

For cesium evaporation $CsCrO_4$-dispensers from SAES mounted in the oven are used (same as in figure 120). These contain fewer amounts of cesium (10 mg) and thus provide the opportunity to vary the experimental setup during the campaign in contrast to using cesium ampoules with 1 g of cesium as in the IPP cesium ovens. Using cesium dispensers the amount of cesium evaporated can be adjusted by regulating the current flowing through the dispenser (typical 6 to 7 A for 10-mg-dispensers).
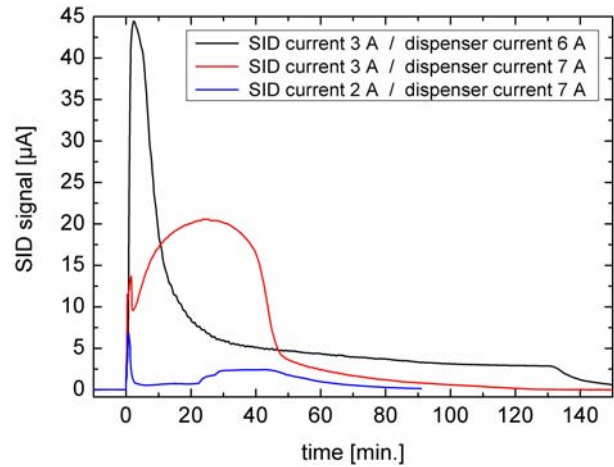

Figure 123: Signals from the investigated oven SID at different heating and evaporation currents.

Figure 123 shows three oven SID measurements for different evaporation rates and SID heating currents (the geometry of the oven SID is type I in figure 122). One can see a very diverse behavior of the oven SID between these three tests arising from increasing cesium coating of the tungsten wires because of the high cesium flux out of the oven. This coating results in non-reliable signals depending on adsorption and desorption rates on to or from the SID wires and has to be prevented. Known from experience, only the measurement with hotter SID wires (3 A SID heating current) and lower evaporation rate (6 A dispenser current) reproduces qualitatively the actual evaporation characteristic from a SAES cesium dispenser (figure 120).

These first tests showed the principle feasibility of cesium flux measurements, i.e. cesium evaporation rates, using the oven SID if the evaporation rate is low. Because of this constriction other geometries of the oven SID have been investigated, e.g. type II in figure 122, which promised fewer problems due to cesium coating of the tungsten wires. During a dedicated experimental campaign at laboratory experiments at the University of Augsburg it was proven that the type II SID geometry is capable of measuring the cesium flux from the oven also for high evaporation rates.
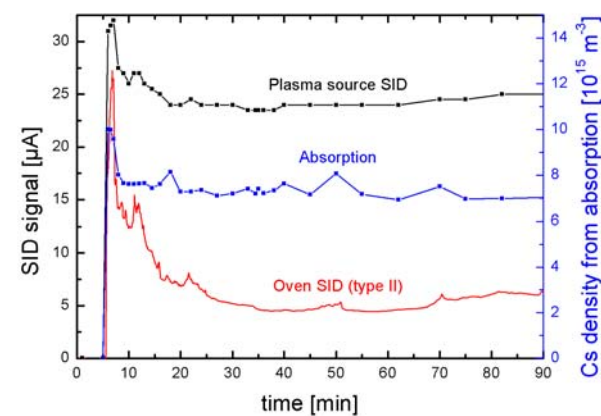
Figure 124 shows the SID signal taken with the type II geometry oven SID attached to a cesium oven equipped with a cesium dispenser. For comparison, the signal of the local SID (present in the volume of the plasma source) and the cesium density determines by absorption spectroscopy are shown. The temporal evolution of all three signals is in very good agreement.

Figure 124: Signals from the investigated oven SID (type II), compared with results of the SID in the plasma source and laser absorption.

It can bee seen that the signal of the type II SID shows a higher dynamics (more than 4 orders of magnitude) than the SID in the volume and the absorption. Compared to the absorption, the detection limit is much lower. Additionally, as described above, it is the only diagnostics which provides a local measurement of the cesium flux at the point where the cesium is released into the plasma. In general, the flux can be measured by surface ionization detectors with a high temporal resolution (up to 'in-situ', depending on the current measurement equipment). The higher temporal resolution of the type II SID results shown in figure 124 compared to the SID in the volume is due to technical reasons.

Until now only relative values for the evaporation rates can be determined. Due to the locality of the SID the signal shows a strong geometrical dependence and so absolute calibration of the SID current is difficult. An option would be to use the overall evaporated amount of cesium (10 mg) in comparison with the time-integrated SID signal to get quantitative evaporation rates. This calibration is then significant for the designated experimental arrangement and cannot be transferred to another experiment, e.g. the IPP sources. Therefore also simulations have to be made.

6.4 Development of a Simple Cs Absorption Diagnostic for Negative Hydrogen Ion Sources

This topic has been supported (procurement of hardware) also by an ITER R&D contract[5].

6.4.1 Background

The amount of Cesium in a negative hydrogen ion source is one of the most critical parameters in achieving stable and reliable currents of negative ions and electrons. The evaporation and redistribution of cesium can presently only be measured during plasma discharges by emission spectroscopy. A quantification of the overall amount of Cs, however, is almost not possible as more than 90% of the Cs is ionized. The emission rate of the single ionized cesium (Cs^+) is rather weak; hence, the neutral Cs line at 852 nm is accessible only.

In contrast to emission measurements the absorption technique offers access directly to the ground state density in the plasma and — even much more important — in the vacuum phase. In particular the latter may give valuable information of the actual evaporation rate of the oven (if switched on), desorption from the different surfaces being at different temperatures (source body and grid) and the redistribution with the interplay of both. The technique itself is non-invasive and based on fiber optics.

Experiments at MANITU indicate that the Cs distribution during the vacuum phase may determine the performance of the source. Hence, the combination of both OES and absorption would be very desirable to get more insight in the Cs dynamics in the source, especially during the vacuum phase, and in a next step for its control.

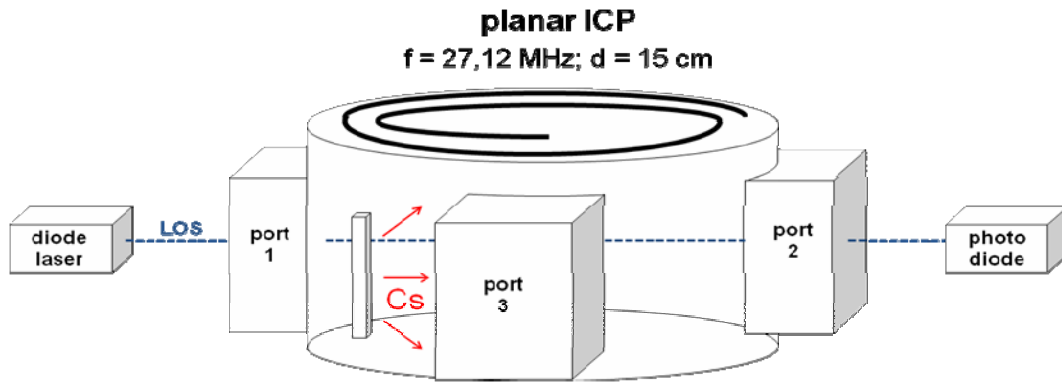[5] Contract number ITER/CT/09/4100000772

Figure 125: Experimental setup of the diode laser absorption system at a compact lab experiment.

Basic experiments at a small lab experiment at the University Augsburg showed than the method itself works as well in the vacuum and in the plasma phase for parameters (Cs densities, pressure, …) that are relevant for negative hydrogen ion sources (see the IPP EFDA report TW6-THHN-NBD1-FR.pdf).

The present experimental setup is rather advanced: it is based on the usage of a highly stabilized white light absorption method with lenses for the optics and a spectrometer for detection of the signal. For the application at negative hydrogen ion sources a much simpler system is suggested by using just a diode laser for the Cs 852 nm line (mode stabilized to avoid mode beating and thus increased noise level), a fiber connected to the laser with the source, and a detector based on a diode with an interference filter.

In the first step the simple setup was installed at the lab experiment at the University of Augsburg where it has been counterchecked with the present advanced setup regarding feasibility and reliability. For that, dedicated experiments were done on the sensitivity of the system both in vacuum and plasma operation. Furthermore, the new diagnostic has been calibrated against measurements of the Cs density by using OES (plasma phase) and a Langmuir-Taylor-Detector (vacuum phase).

In the next step the equipment will be transferred and tested at BATMAN, also in preparation for its usage as a standard diagnostics at ELISE.

6.4.2   Experimental Setup

First testing of the diode laser absorption system was done at a compact lab experiment (planar ICP, f = 27.12 MHz, d = 15cm) at the University of Augsburg (figure 125). The absorption setup is rather simple: a tunable diode laser (tuning of the wavelength is done by variation of the diode laser current) is used as the light source and a photo diode as the detector. The

Parameter	Value
Tunable range	851 nm – 853 nm
Maximum current	200 mA
Output power	> 140 mW @ 852.0 nm
Current tuning	1.33 GHz per 1 mA
Temperature tuning	20.0 GHz per 1 °C

Table 4: Technical data of the diode laser

technical data of the laser is summarized in table 4. The signal of the photo diode is amplified and readout by a PC, which also controls the tuning of the wavelength.

Fiber optics will is used between the experiment and the diode laser / photo diode, which allow a simple access to the ion sources. Cesium vapor is generated by Ohmic heating out of cesium-chromate-dispensers that can be handled easily (cesium is bonded in the chromates, so they can be handled at room conditions). The dispenser is aligned to the line of sight of the absorption / emission spectroscopy. The measurements are carried out in the vacuum

Figure 126: Comparison of the diode laser absorption to the white light absorption and theoretical absorption spectrum.

phase (Background pressure $p = 1 \times 10^{-5}$ mbar) as well as in the hydrogen plasma phase ($p = 10$ Pa, $P_{max} = 320$ W) with similar plasma parameters as in the ion sources close to the grid.

Other diagnostics are available for comparison and calibration to the diode laser absorption spectroscopy: The Optical Emission spectroscopy (OES), a Langmuir Taylor Detector (LTD, mounted in the bottom plate) and the white light absorption spectroscopy (the latter cannot be used at the same time as the laser setup due to its large optic).

6.4.3   Commissioning at University of Augsburg

Figure 126 shows an absorption spectrum of the Cs-852 nm-line taken with white light and with laser absorption as well as the predicted absorption for a Doppler broadening corresponding to 1000 K. The line is split into six hyperfine lines, but only two peaks can be resolved because of the Doppler broadening. In comparison to the white light absorption spectroscopy, the laser system shows no additional broadening due to the apparatus profile of the spectrometer and thus a much improved signal to noise ratio which improves the detection limit by one order of magnitude (laser absorption: $n_{Cs} > 10^{14}$ m^{-3}, white light absorption: $n_{Cs} > 10^{15}$ m^{-3}).
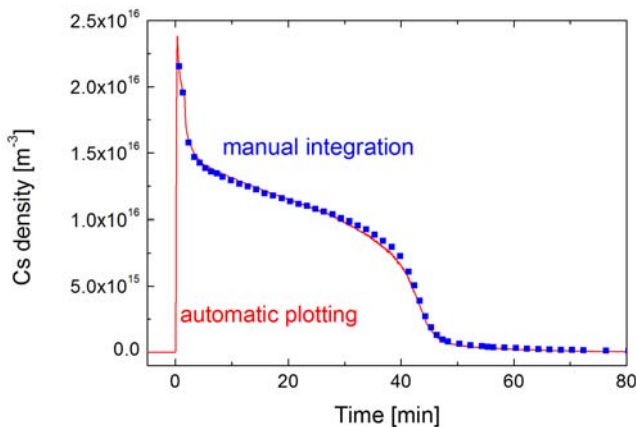
Also the speed of the laser absorption setup is much faster than the white light absorption: with the laser system 25 spectra per second can be recorded in comparison to 2 spectra per minute of the white light absorption. Automatic integration of the absorption peaks lead to an easier handling of the

Figure 127: Different integration methods.

laser absorption system, since there is no time-consuming manual integration necessary. This method offers the possibility of an online signal, which can be monitored in the same way as the other diagnostics of the ion sources. Figure 127 shows the difference of the automatic plotting to a manual integration. Since the diode laser is not exact stable, the manual integration lead to more accurate results. But the automatic plotting should be more than sufficient for most operation scenarios.
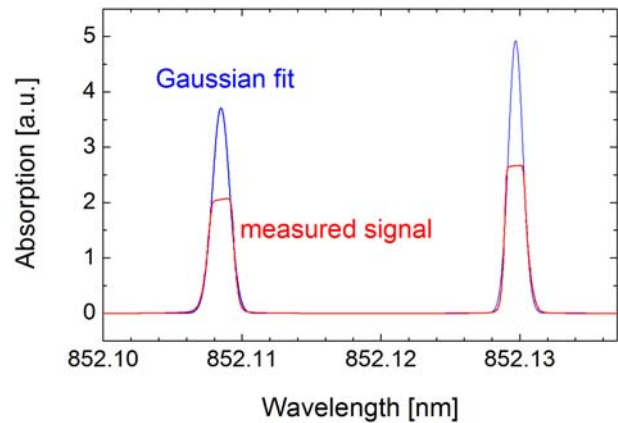
Two problems arose, which both result in an underestimation of the densities. On the one hand the absorption signal is being saturated by high absorp-

Figure 128: Saturation of the absorption peaks can be corrected by Gaussian fits on the edges.

tion (high cesium densities and / or long absorption length) as shown in figure 128. In order to obtain the correct Cs-density a Gaussian fit on the edges of the absorption peaks must be performed. A correction factor can be calculated out of the ratio between the area of the Gaussian fit and the area of the measured signal (see figure 128). Because of the much larger absorption length in the ion sources it is expected, that this effect is very important in the operation at BATMAN.

The other effect is due to the high spectral intensity of the diode laser, which depopulates the ground state of the transition along the line of sight. The fact that the absorption spectroscopy measures the density in the ground state results in a too low detected Cs-density. To reduce the optical pumping into the upper state, the intensity of the diode laser can be reduced by using neutral density filters (see figure 129). But by damping the laser intensity the signal to noise ratio decreases. A higher amplification of the photodiode signal must be used that reduces the speed of the system because of the lower bandwidth of the amplifier at high amplification values. Thus, damping of the signal is only possible to a certain value. Correction of this effect is possible if a factor for correction (which depends on the laser intensity and on the cesium density) is known.

For that reason, the effect of the depopulation of the ground state has determined by using a commercially available cesium absorption cell (Figure 130). Heating of the cell (up to about 80°C) and cooling of a small point of the surface (cold spot) to a definite temperature, results in a well controlled vapor pressure. The cold spot control was achieved by an in-house development. The cesium density can be calculated out of the vapor pressure by knowing the gas temperature (temperature of the
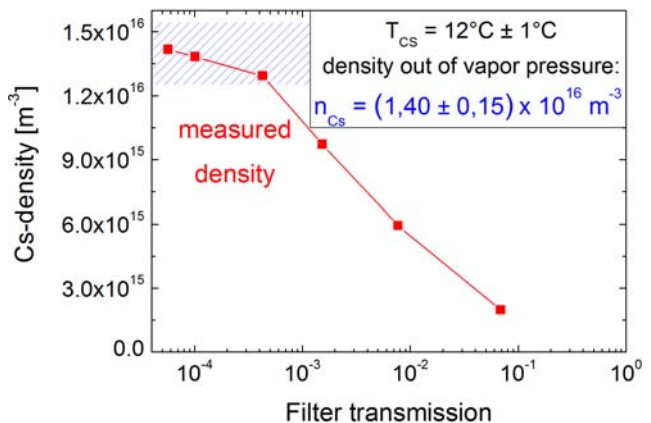

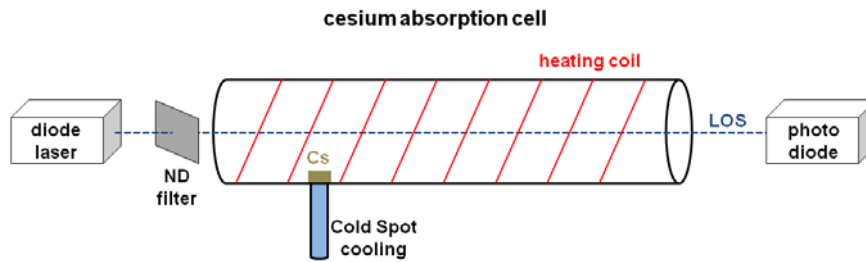*Figure 129: Depopulation of the ground state lead to a lower measured cesium-density.*

Figure 130: A definite Cesium density can be generated with a Cesium absorption cell.

cell). Then the measured Cs-density can be compared with the actual density for different laser intensities (different ND-filters) and for different vapor pressures (different cold spot temperatures). To compare these results to the actual experiment, the different absorption lengths must be considered. The same absorption is being accomplished, if the shorter length of the cell is being compensated with a higher Cs-density.

After understanding the difficulties of the laser absorption system it became possible to compare the results to results from other diagnostic techniques. In the plasma phase, Optical Emission Spectroscopy can be used. Figure 131 shows a good relative agreement among the two techniques, if the laser absorption signal is corrected for saturation and depopulation. The difference of the diagnostics can be explained by the fact, that the OES has a high uncertainty since knowledge of the plasma parameters n_e and T_e is needed. In particular the measurement of n_e is difficult at the moment, since it can be measured only at a comparable experiment with

Figure 131: Comparison of the laser absorption to the OES.

Figure 132: Comparison of the laser absorption signal with the signal from the Langmuir-Taylor-Detector.

a Langmuir probe. For the future it is planned to use a probe in the same experiment during the whole cesium measurement. This will lead to more certain results of the Optical Emission Spectroscopy. At the moment the laser absorption is the more confident diagnostic and so better for evaluation.

In the vacuum phase, the laser absorption can be compared to a Langmuir-Taylor-Detector (LTD or SID, see section 6.3). If the signal of the LTD/SID is scaled to fit (it can only measure relative cesium densi-
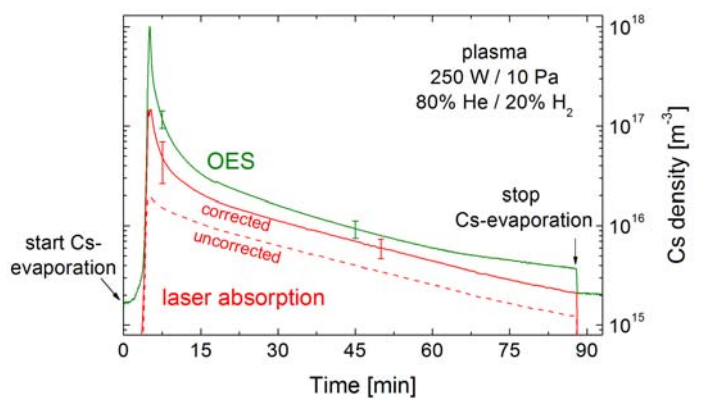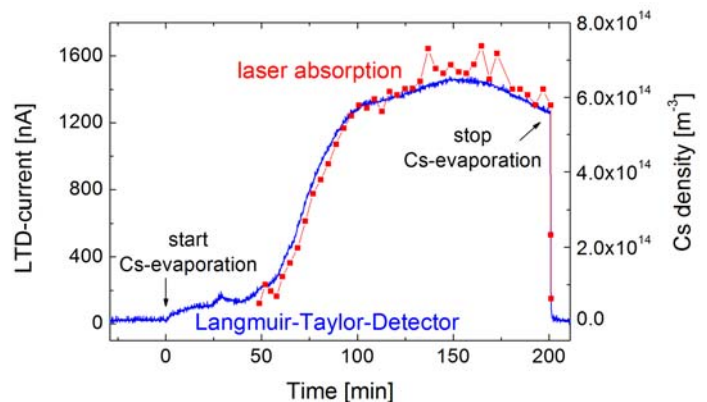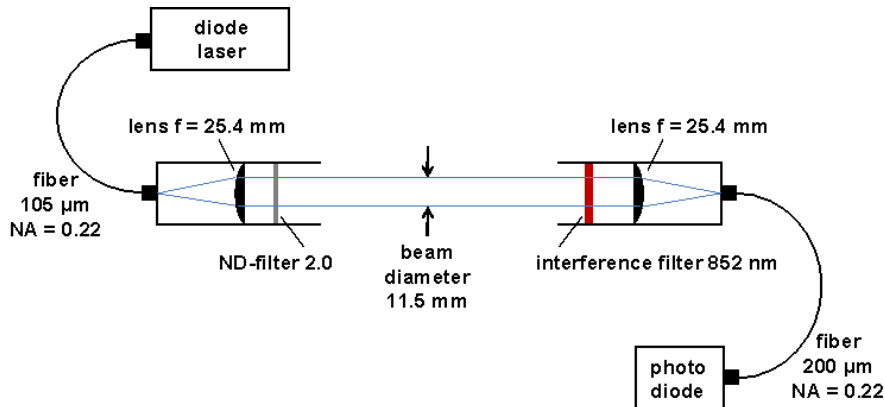
Figure 133: Setup of the Cs absorption diagnostics at the negative ion source test bed BATMAN.

ties), a good agreement is achieved. Because of the low cesium density during this measurement, a correction of the saturation was not necessary here. The measurements demonstrate also the high sensitivity and the improved detection limit of the system.

6.4.4   Operation at BATMAN

As next step, the laser absorption system was installed at the IPP ion source test bed BATMAN in order to measure evaporation and redistribution of cesium during both vacuum and plasma phase for the first time. Figure 133 shows the setup which is in principle similar to Figure 130 with the cesium absorption cell replaced by the plasma of the ion source. To prevent the detection of other lines instead of the Cs 852 nm-line, an interference filter is applied in front of the diode. The cesium laser absorption system is running routinely now at BATMAN using the automatic plotting routine described above. The results are written in the common database. Thus, directly after a pulse, the results of the absorption can be compared with the results of all other diagnostics available at the experiment.

A very surprising result is the temporal evolution of the measured neutral cesium density before, while and after a pulse, shown for one pulse in a well conditioned ion source in Figure 134. Additionally shown in this figure is the cesium signal measured by OES. Since the diode measures the emission of the Cs 852 line, it gives information on the cesium density during the pulse only. The temporal evolution of the neutral cesium density measured by the two techniques during the plasma pulse is almost identical.

In the vacuum phase before the pulse (labeled ① in the figure) a relatively low cesium level is detected by laser absorption. This low level stays constant over time. Solely cesium
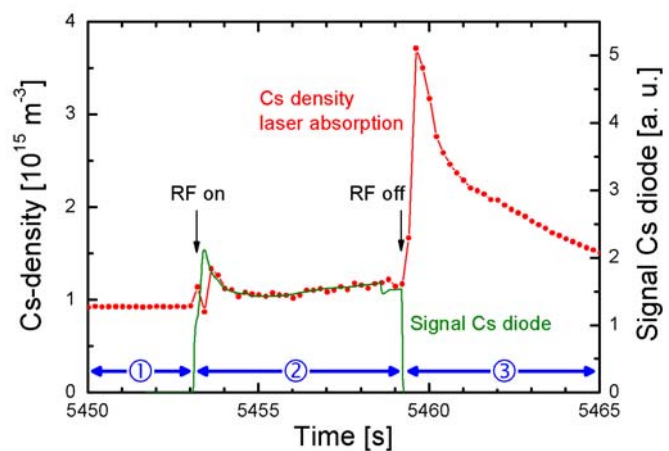

Figure 134: Cesium signals before, during and after a pulse at BATMAN measured with the laser absorption and the Cs diode.

atoms are present in the volume of the ion source. At the beginning of the plasma pulse (phase ②), a huge amount of neutral cesium is released immediately from cesium reservoirs at the walls. Thus, the total cesium density in the source volume strongly increases. Simultaneously, due to the existence of free electrons with a temperature in the eV range, the major part of the cesium in the source volume is immediately ionized. The neutral cesium forms only a small fraction of the total cesium density. As result of these two inverse effects, the cesium densities measured by the cesium absorption in the vacuum phase and during the plasma pulse are almost identical, followed by a slow decrease which lasts up to several seconds.

After the pulse (phase ③), the densities of neutral and ionized cesium are affected mainly be two processes: on the one hand, neutral cesium and cesium ions are lost by diffusion to the walls. On the other hand, cesium ions are recombined in the volume very quickly to neutral cesium atoms. As consequence of the latter effect, the neutral cesium density increases rapidly after the end of the plasma pulse.

While the length of the vacuum phase between the pulses is in the order of several minutes, much longer vacuum phases appear during operational breaks at night, weekend or holidays. During these longer vacuum phases the low measured cesium level slowly decreases. This effect is caused by impurities like oxygen or hydrogen which contaminate the cesium layers on the inner surfaces of the ion source. With on-going contamination, the sticking probability of the cesium atoms to the wall increases. The rate with which the atoms are exchanged between the inner walls of the ion source decreases and consequently also the cesium density in the volume.

Figure 135 shows the measured decrease of the cesium density after the end of source operation for two different wall temperatures. The cesium density decreases with a typical delay time of 10 minutes (wall temperature not controlled) or 28 minutes (wall temperature set to 45 °C, plasma grid temperature set to 150 °C, i.e. the same conditions as during source operation). This difference in the delay times is caused by the dependence of the sticking coefficient of cesium at a surface on the temperature of this surface. For higher surface temperatures the sticking probability is lower. Further investigations on the delay of the cesium signals after the end of operation will be performed. Goal is to learn how to improve the source performance by changing the source conditions during operational breaks.
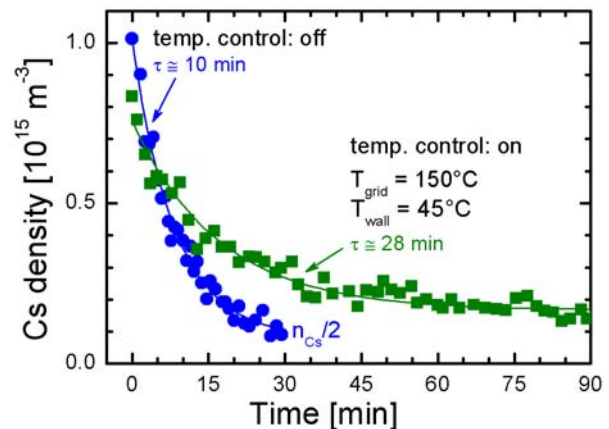

Figure 135: Decay of the cesium density after the end of source operation with and without temperature control of the walls.

Since the cesium absorption is working routinely now, the behavior of the cesium density before, during and after the pulses can be measured for a large number of pulses. This will be done, for example, during an experimental campaign starting with a cesium free ion source. After that, the equipment will be transferred to the long pulse test facility MANITU and after that to the large ion source RADI to monitor the Cs injection in large sources. In general, the measurements during the plasma phase can be used to better con-

trol the cesium injection into and the re-distribution inside the source. The investigations on delay of the cesium flux during the vacuum phase are an important step to obtain a better understanding of the processes responsible for the contamination of the cesium layers with impurities.
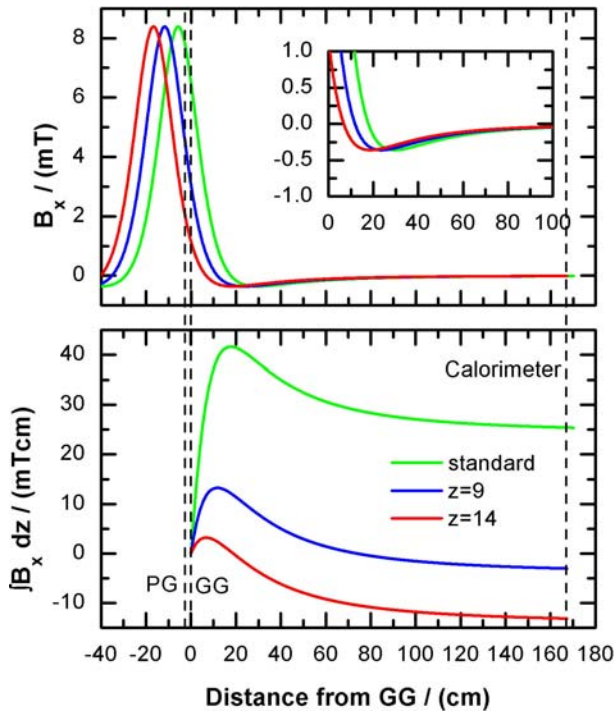
Figure 136: Horizontal magnetic field (top) and the corresponding ∫Bdz between grounded grid and calorimeter at BATMAN.
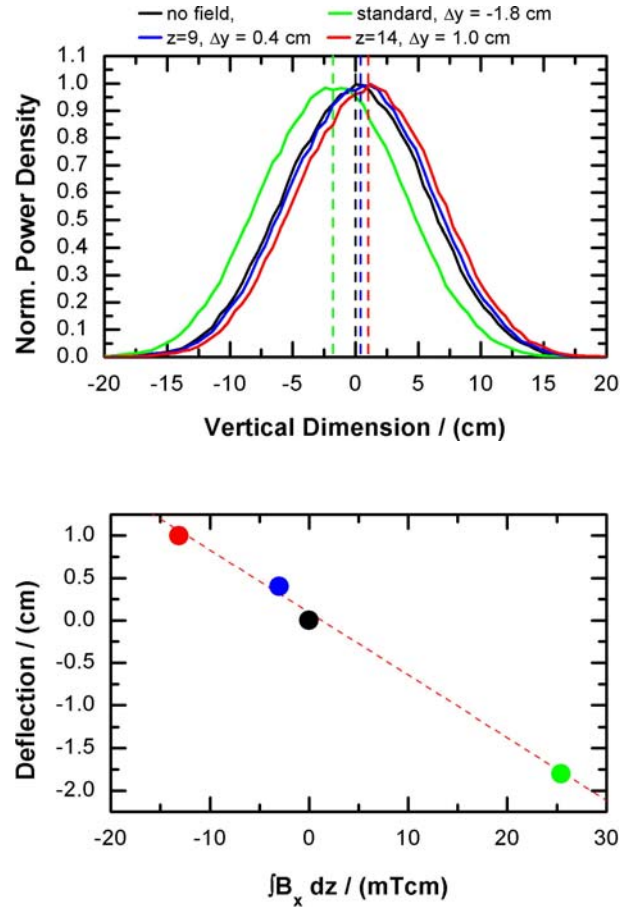

Figure 137: Normalized beam profile at the BATMAN calorimeter (top) and the dependence of the beam deflection on the ∫Bdz value (bottom) for a 20 kV hydrogen beam with 2° divergence for all beamlets.

7   Modeling (WBS 4.0)

7.1   Beam Transport (BBC-NI)

A new beam transport code, BBC-NI (Bavarian Beam Code for Negative Ions), has been developed in the last months. Presently, this Monte-Carlo code can calculate the beam transport between the grounded grid and some beamline components (i.e. the calorimeter) in magnetic and (external) electric fields for realistic grid and magnetic field geometries. The code has been benchmarked against the old IPP DENSB code, which is not able to calculate magnetic field effects due to principal reasons.

A first application of the code was the calculation of the vertical beam deflection at BATMAN for the various magnetic field configurations (see section 3.1), as the measurements of the beam position on the calorimeter showed some features that are not well understood (see figure 18). Figure 136 shows the horizontal magnetic field as well as the respective ∫Bdz value for the different magnetic field configurations. As it can be seen, the total ∫Bdz from the GG to the calorimeter does not reflect necessarily the magnetic field strength with the acceleration system due to the field reversal downstream.

Figure 137 shows the first results of the beam profile at the BATMAN calorimeter for a 20 kV beam with a (homogenous) divergence of 2° for all beamlets. For these first tests, it was assumed that beamlet-beamlet interaction could be neglected as well as no neutralization takes place. The position of the maxi-

mum of the beam at the calorimeter depends linearly on the total ∫Bdz value from grounded grid to the calorimeter. Hence, the deflection is larger for the "standard" field and the "BMAX, z=14" case. For the "BMAX, z=9" case, the deflection is almost zero, as the total ∫Bdz is almost zero. This was also observed in the experiment (see figure 18), but the amount of the deflection is much less than observed, cm's instead of several cm's.

The code development will be continued as part of a PhD thesis. Next steps are the implementation of the ion transport between the plasma grid and the grounded grid; here the contribution to the ∫Bdz value should not be neglected despite the short distance, but the voltages are lower, and the fields are larger, so that a larger deflection might result.

The final goal of the code development is the reconstruction of the ELISE beam properties from beamline diagnostics like Doppler spectroscopy and calorimetry. For that reason, a routine for the calculation of the Balmer light emission along a given line of sight will be implemented.

7.2 Boundary Layer (BACON)

Particle-in-cell (PIC) codes calculate profiles of the electrostatic potential and particle densities in plasmas in a self-consistent manner. These codes track a large number of charged macro particles. The calculation domain is divided into small cells (to avoid oscillations, the size of each cell needs to be comparable to the Debye length) and time is divided into time steps (which need to be comparable to the inverse plasma frequency). Due to the large number of macro particles, grid cells and time steps, PIC codes need a large amount of RAM and CPU time and are mostly applied for small domains only (close to the plasma sheath at the walls or the tip of a Langmuir probe). Often also a reduced number of spatial dimensions is used.

The complex interplay between the magnetic filter field, bias voltage, source geometry, cesium dynamics and the other plasma parameters (electron density, electron temperature) in the IPP negative ion sources is not fully understood yet, albeit being essential for optimizing the production of negative ions on the PG surface and their transport towards the extraction apertures. Thus, the PIC code Bacon developed at the IPP has been applied to investigate the transport and cooling of electrons in the magnetic filter field. These calculations are performed in a linear 1d3v domain (one
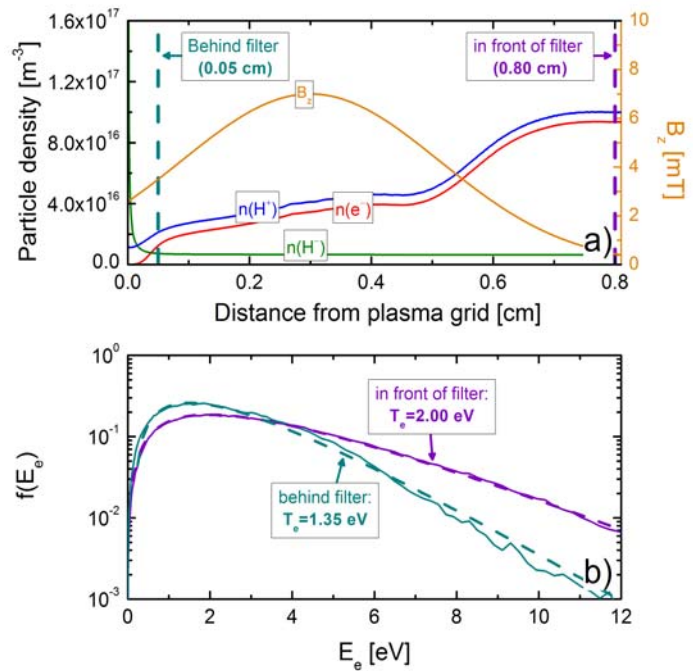

Figure 138: Influence of the magnetic filter field on the densities of charged particles (top) and on the energy distribution function of the electrons (bottom).

spatial dimension, three velocity dimensions) for the real plasma parameters of the IPP ion sources. This approach is in contrast to other available codes which often use reduced parameters to speed up the code.

Bacon considers Coulomb collisions as well as several elastic and inelastic collision reactions. To achieve the maximum possible speed, the null collision method is used for the calculation of elastic and inelastic collisions. This method introduces an additional collision process – the so-called null collision – to obtain a total collision probability which is constant over the whole computational domain. When the collision module is invoked (once per simulated time step) this constant total
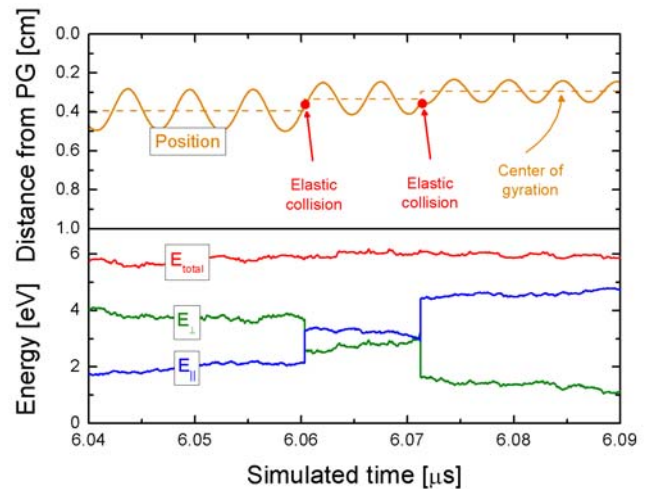

Figure 139: Simulated trajectory of a magnetized electron (upper part). Energies of the electron movement parallel and perpendicular to the magnetic field lines and total kinetic energy (lower part).

collision probability is used to completely exclude a certain number of macro particles from the calculation of the occurred collisions.

Figure 138 shows calculated particle density profiles close to the plasma grid surface with taking into account a magnetic field. The absolute value and the shape of the magnetic field strength correspond to the filter field of the IPP ion sources while the spatial dimension is significantly smaller. The densities of electrons and protons strongly decrease at the onset of the filter field. Compared to this rapid initial decrease of the particle densities, the further decrease during the transport through the filter is much shallower. Further investigations based on different lengths (and shapes) of the magnetic filter field will be performed in future.

Figure 138 shows also the calculated electron energy distribution function (EEDF) before and after the transport through the filter: a significant cooling effect takes place (from initially 2.0 eV to around 1.35 eV on the downstream side of the magnetic filter close to the plasma grid surface). Additionally, in this region a slight deviation of the distribution function from a Maxwell EEDF is observed.

To enable investigations on the relative relevance of the different collision processes for the transport of charged particles across the field, a re-implementation of the Monte-Carlo (MC) module responsible for treatment of elastic and inelastic collisions was necessary: while in the previous version of this module all considered reactions have been defined directly in the source code, the improved version supports external input files. Thus, now it is much easier to activate or de-activate single reaction processes. The improved version of the MC module has been implemented and extensively tested against the previous version. It was shown that both versions of the MC module yield identical results

Using the new MC module, the relevance for the electron transport across the field of the following three collision types was investigated: Coulomb collisions, elastic and inelastic collisions. By the very frequent Coulomb collisions the magnetized electrons are displaced by a small distance only. Thus, Coulomb collisions can cause a slow and steady transport of the electrons across the field. In contrast, elastic and

inelastic collisions cause rapid changes in the electrons direction of flight. Each of these sudden changes kicks the electrons from one field line to an close-by field line by displacing the centre of gyration.

A result of calculations with different collision processes activated and de-activated in the PIC code is that the electron transport across the field in the IPP ion sources is mainly caused by elastic collisions. Figure 139 shows the position and energy of one magnetized electron simulated by the PIC code. The influence of two elastic collisions on the flight direction and the center of gyration can be seen in the upper part of the figure.

Figure 140: Comparison of the three magnetic fields with equal field integral ∫Bdz used as input for Bacon.

In the lower part of the figure the total kinetic energy of the electron as well as the energies of the movement of the electron parallel and perpendicular to the magnetic field lines are shown. It can be seen that the total kinetic energy of the electron is unaffected, pointing up the inelastic character of the two collisions.

As next step, the transport of electrons across filter fields with different shapes was investigated. Three different shapes of the magnetic fields have been used for the calculations and are shown in figure 140: two different Gaussian shapes and a logistic shape. The field integral ∫Bdz of all these three magnetic field was chosen to be identical and equal to the field integral in the ion source prototypes. Figure 141 shows the calculated profiles of the electron density and electrostatic potential for all three magnetic fields. The potential profile is identical for the three different fields. The electron density decreases rapidly at the onset of the magnetic field. Although the position of this decrease is different, the electron density inside the filter close to the plasma grid surface is comparable for all three fields. These results indicate that the functionality of the filter is determined mainly by the integral of the magnetic field strength.

The new MC module can also be used to easily implement new production channels into the simulation. One process potentially of importance for the development of the potential profiles close to the plasma grid is the production of photoelectrons by impact of energetic photons generated in the driver. These electrons form an additional negative space charge. The flux density of photons from the driver hitting the plasma grid
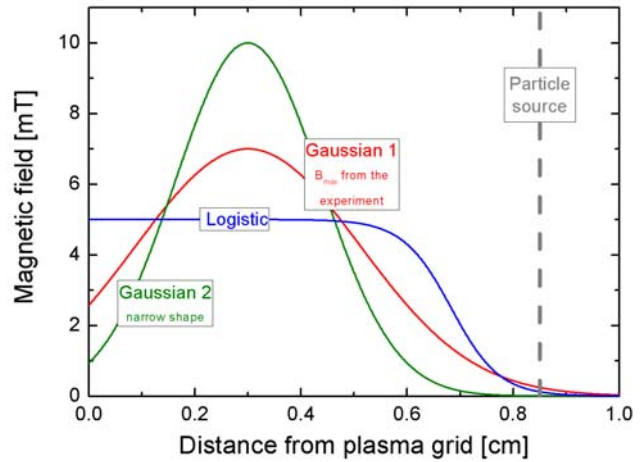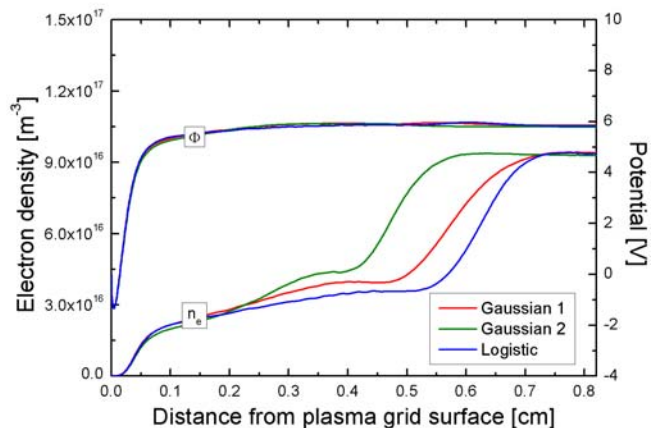

Figure 141: Profiles of potential and electron density calculated with Bacon for the three different magnetic fields.

was calculated by combining results of calculations with the Collisional Radiative model for molecular hydrogen based on the Yacora solver and a simple geometric estimation. Before applying the PIC code, a simple estimation was performed: by multiplying this flux with the quantum efficiency, it was shown that the flux of photo electrons from the grid surface is an order of magnitude smaller than the flux of surface produced negative ions. Next step will be to add the photo electron production into Bacon and investigate the influence of these electrons on the plasma and vice versa. Such calculations have been prepared by arranging the quantum efficiency for generation of photo electrons on cesiated surfaces.

7.3 Ion Transport in Boundary Layer (TRAJAN)

The 3D Monte Carlo transport code Trajan was developed to model the transport of negative hydrogen ions from their point of birth at the plasma grid surface to the extraction apertures. Trajan includes the complex large-scaled magnetic field topology and converter geometries in the IPP negative hydrogen ion source prototypes. Aim of the code is to investigate and optimize the interplay of magnetic field and extraction system geometry with the negative ion transport.

Trajan is capable of performing simulations of the complete converter system. The complex 3D magnetic and electric fields needed as input parameter have been computed by external codes. Destructive (electron stripping, mutual neutralization, collisional/associative detachment) and non-destructive (Coulomb and charge exchange) collisions of negative hydrogen ions with plasma particles are considered by means of Monte Carlo methods. The required densities and temperatures of the background particles (electrons, H, H_2, H^+, Cs^+) are taken from measurements with OES and the Langmuir probe.

Trajan can be applied to calculate profiles of the extraction probabilities over the area of the converter surface as well as the current density distribution over the extraction apertures. In figure 142 the extraction probabilities and current density distributions calculated for the LAG system are shown. The spatial resolution makes it possible to detect areas of intensified ion production on the converter and to resolve the current density distribution in individual beamlets. This is especially important for beam optics calculations, where the current density distribution can be used as an input parameter.
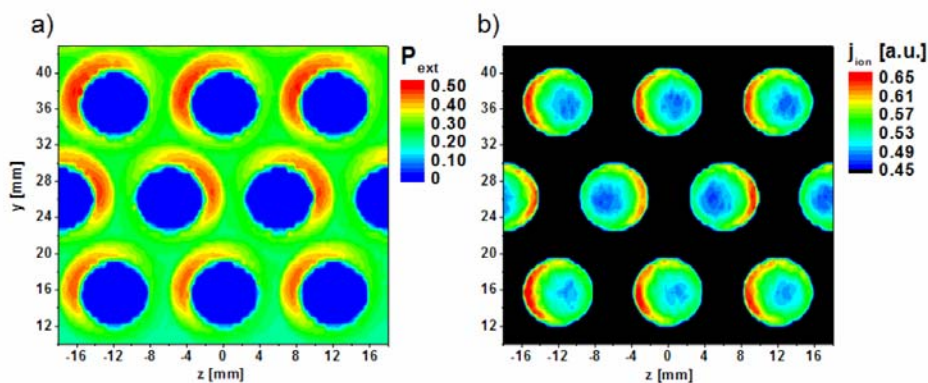

Figure 142: a) Profile of extraction probability and b) current density distribution calculated for the LAG system using the TrajAn code.

The negative hydrogen ion current extracted from negative ion sources is determined by the number of ions generated on the converter surface as well as on the efficiency of the negative ion transport towards the extraction system. While the latter can be calculated with Trajan, the coupling of both aspects is important for the understanding of the source physics and to optimize the performance and homogeneity of the delivered current density distribution.
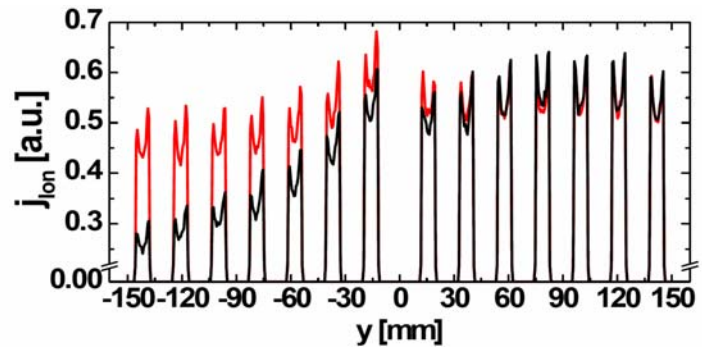

Figure 143: Vertical current density distribution for negative ion surface production being homogeneous (red) or proportional to the inhomogeneous flux of Cs towards the MANITU plasma grid during a short pulse (black).

Prerequisite for the described coupling is a model of the ion source surfaces. This model should calculate the negative ion production yield and consider the different possible wall materials, the amount of cesium deposited to the wall as well as the amount of the impurities (H, O, Cu …). The availability of such a surface model would enable the coupling of TrajAn to CsFlow (which calculates the cesium flux to and from the inner source surfaces; see section 7.4).

Since such surface models are not available, as a first step it was assumed that the negative ion production rate is determined solely by the flux of cesium onto the wall[6]; the latter was calculated by the CsFlow code. This simple model enabled the investigation of basic dependencies. A Result of first calculations of the vertical distribution of the extracted negative ion current density are shown in figure 143. The surface density of negative hydrogen ion production on the plasma grid surface was assumed to be homogeneous (red curve) or proportional to the profile of the cesium flux onto the surface. The latter was calculated by CsFlow3d for short pulse of the ion source. It can be seen that a homogeneous profile of negative ion surface production is directly correlated to a more or less homogeneous profile of the extracted current density. Inhomogeneities in the surface conditions of the plasma grid, on the other hand, will strongly affect the current density distribution at the plasma grid and hence the beam homogeneity (see also section 4.4
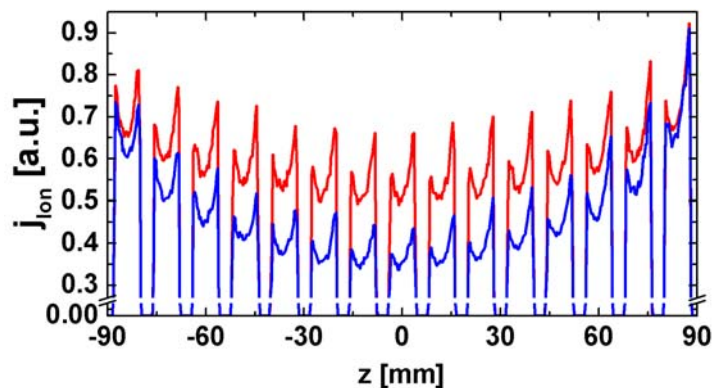

Figure 144: Horizontal current density distribution for negative ion surface production being homogeneous (red) or proportional to the inhomogeneous flux of Cs towards the MANITU plasma grid during a long pulse (blue).

Figure 144 is similar to figure 143 but

---

[6] This assumption is justified due to the fact that Cs layers in sources with pure vacuum conditions as it is in the IPP RF driven sources the surface work function of a Cs layer degrades with time due to chemical passivation; hence, fresh cesium is needed in order to keep the work function low.

shows a horizontal cut through the expansion system. Again, the negative ion production density is assumed to be homogeneous (red curve) or proportional to the profile of the cesium flux onto the surface (blue curve). In contrast to figure 143, the profile of the cesium flux into the grid was calculated for a long pulse of the ion source at the test bed MANITU. The main difference of the cesium fluxes calculated for short and long pulses is the influence of the bias plate. Since the bias plate is not actively cooled, it warms up during long pulses. As a consequence, after a certain time during the long pulse, additional sources for (neutral) cesium flux onto the plasma grid are opened on the bias plate surface. The bias plate surrounds the plasma grid and thus the calculated extracted negative ion density for the long pulse shows a much more pronounced dependency on the horizontal position. An actively cooled bias plate - as it is planned - is indispensable for the stable long pulse operation of future experiments like ELISE or Spider.

The present results emphasize the importance to develop an advanced method (i.e. an appropriate surface module) to couple CsFlow3d and Trajan.

7.4 Cs Distribution (CsFlow3D)

The 3D Monte Carlo transport code CsFlow3D was developed in order to model the distribution of atomic and ionic cesium during the vacuum and plasma-on phases of the RF-driven ion sources. The 3D geometry and magnetic field topology of the IPP negative hydrogen ion source prototype was implemented. Elastic collisions of Cs/Cs^+ with plasma and gas particles are considered by Monte Carlo methods. Furthermore, ionization by electron impact collisions of Cs and recombination of Cs^+ are considered.

Figure 145: Total cesium flux onto the plasma grid for cesium injection by the standard oven attached to the upper half of the back plate.

For obtaining relevant results from the model it is essential to use experimentally determined values of the plasma parameters as input for CsFlow3D. Similar to Trajan, particles densities and temperatures are taken from the OES and probe measurements. Additionally, an accurate model of the surface physics of cesium (i.e. adsorption and desorption probabilities) on the chamber walls (50 °C) and on the plasma grid (150°C) is highly important for the cesium transport modeling. Dedicated experiments with a quartz microbalance and a surface ionization detector were carried out in order to determine the sticking coefficient of cesium for different temperatures (see also section 6.3).

Special focus was laid on the dynamics of the ionic and atomic cesium fluxes (during short and long plasma pulses) onto the plasma grid (converter surface). This dynamics is influenced by several effects like
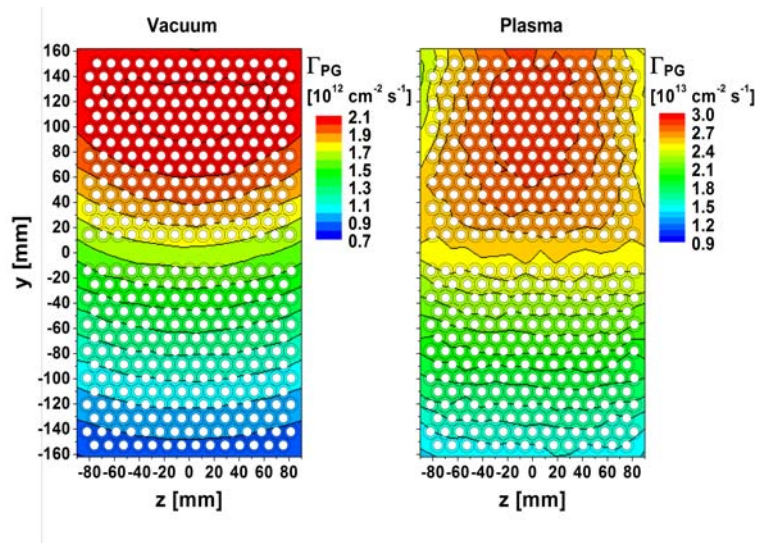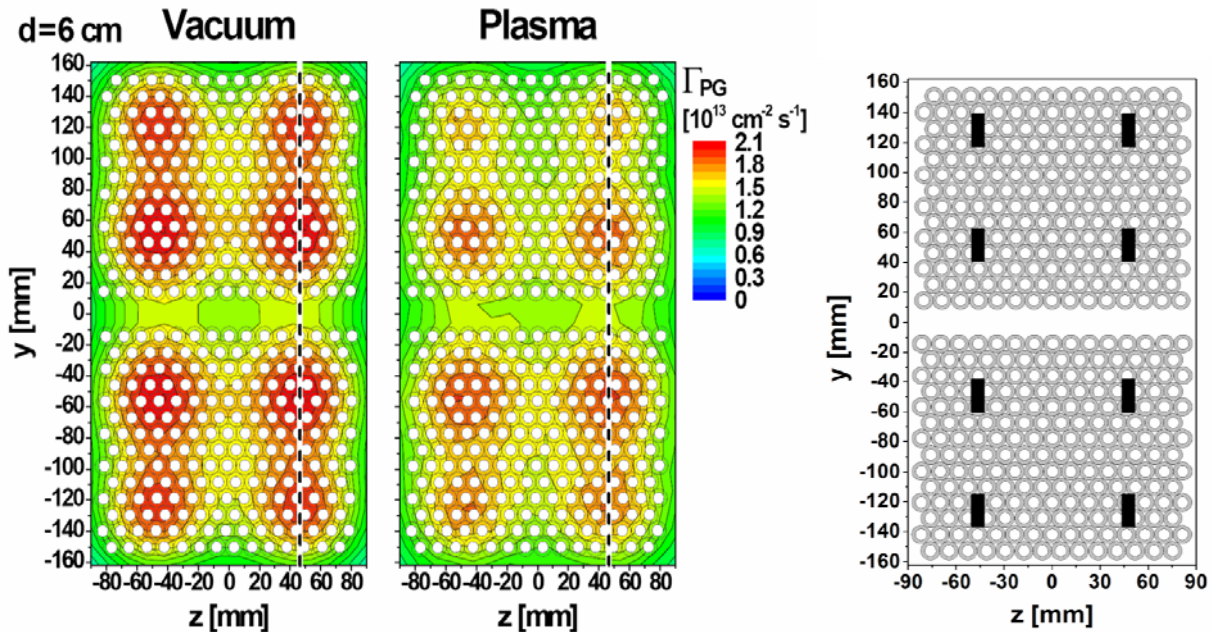
Figure 146: Total cesium flux onto the plasma grid for cesium injection by a dispenser array with optimized arrangement at a distance of 6 cm to the plasma grid during a vacuum and a plasma phase. The picture on the left shows the geometric arrangement for the simulation of the cesium injection by an array of 8 cesium dispenser (Type: SAES Getters) close to the plasma grid of MANITU.

the depletion of cesium reservoirs but also the temperature dynamics of components like the bias plate caused by the thermal load from the plasma particles. As indicated in section 7.3 the cesium flux profiles calculated by CsFlow3D can be used in a simple approach to model the dynamics of the negative ion production. The Trajan code can than be applied to calculate the extracted ion current. First results of such calculations are discussed in section 7.3.

Furthermore, CsFlow3D allows the investigation of the performance of new ways of cesium injection and the optimization of the geometry of the existing system.

In figure 145 the calculated cesium flux onto the plasma grid surface is shown for the standard configuration of the IPP test facilities: the cesium oven is attached to upper half of the back plate. Most cesium from the oven hits one of the side walls first; the cesium flux onto the plasma grid surface is then determined by adsorption and desorption of the cesium at the walls. Anyway, the flux profile of cesium reaching the plasma grid surface reflects the position of the oven, in both vacuum and plasma phases. Since this inhomogeneous cesium flux may be accompanied with an inhomogeneous negative hydrogen ion production, solutions to obtain a more homogeneous cesium flux onto the grid are desirable.

A different approach by cesium injection with a dispenser array (SAES Getters) in the proximity of the plasma grid was evaluated by a numerical simulation with CsFlow3D. Figure 146 shows the calculated cesium flux onto the plasma grid surface delivered by a dispenser array mounted in 6 cm distance to the plasma grid surface. Calculations have peen performed for the vacuum phase (between pulses) and the plasma phase (during the pulses). Although the flux profiles show inhomogeneities, they are much more

homogeneous than the profiles delivered by the conventional cesium evaporation oven in combination with re-distribution via the source walls. Most of the effect is, of course, due to the inhomogeneity of the Cs source at MANITU (oven just at the top of the source). The homogeneities of the calculated profiles can be improved further by optimizing the distance between the dispensers and the plasma grid. A strong counter-argument against the realization of such a dispenser array may be technical and physical issues, mainly caused by the influence of the dispensers on the plasma and vice versa (for example heating up of the dispensers in the plasma).

Of particular interest is the distribution of cesium in larger ion sources as ELISE or SPIDER. In contrast to the small IPP prototype sources, these ion sources will use more than one cesium oven. For ELISE, for example, two cesium ovens are foreseen. To enable the application of CsFlow3D to larger ion sources, first the geometry of the ion source needs to be implemented into the code. It was started to construct a model for the geometry of the ELISE ion source. Up to now, no results of this new model are available.

The presented calculations have proven that CsFlow3D is capable of basically investigating new techniques for injecting cesium into the ion sources. This capability of the code can be used for further investigations - for example - on possible new geometries of the cesium oven nozzle.

7.5   OES (YACORA)

To determine plasma parameters (electron density, electron temperature …) from line emissivities measured by OES, population models are necessary. Since electron densities (10^{17} m^{-3} close to the plasma grid – $5 \cdot 10^{18}$ m^{-3} in the driver) in the IPP negative hydrogen ion sources are too high for applying the corona model (which balances solely electron collision excitation from the ground state with radiative de-excitation), usage of collisional radiative (CR) models is mandatory. These models balance excitation and de-excitation processes for all states in the considered atom, molecule or ion. At IPP the flexible solver Yacora is used for the development of CR models. Up to now models for different atomic and molecular species exist; of particular interest for plasma diagnostics in the negative hydrogen ion sources are the models for H and H_2.
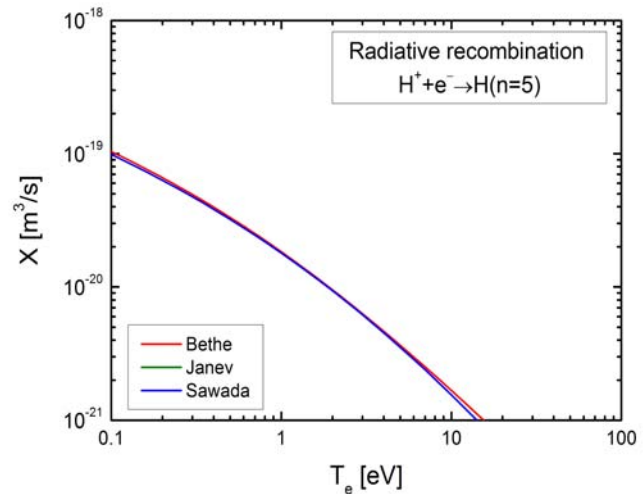

Figure 147: Comparison of rate coefficients taken from three different data sources for radiative recombination of H$^+$.

While the hot plasma in the driver is ionizing (i.e. excited states of the hydrogen atom or molecule are populated predominately by direct excitation from the ground state), parts of the cold plasma in the extraction region close to the plasma grid are recombining (i.e. population mainly by recombination processes).

The position of the boundary between the ionizing and recombining plasma regimes depends on external parameters like for example the position or direction of the magnetic filter field.

The accuracy of the results calculated by any model strongly depends on the accuracy of the used input data. CR models include a large set of processes, consequently a large data base consisting of reaction cross sections (or rate coefficients) and transition probabilities. The input data used by Yacora for direct excitation of the hydrogen atom has been verified and updated some time ago [10] while this work is not yet finished for the recombination of H^+ and dissociative recombination of H_2^+.
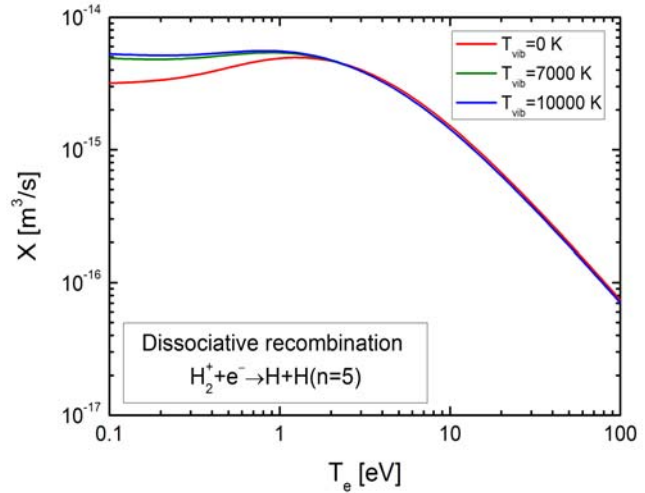
Figure 148: Comparison of rate coefficients for dissociative recombination of H_2^+ calculated for three different vibrational temperatures.

Thus, a critical review of the input data base for recombining plasmas used by Yacora was performed. Final goal is to ensure that the model yields accurate results in both ionizing and recombining hydrogen plasmas as well as in the transition between these two regimes.

The only relevant recombination process of H^+ in the extraction region of the IPP ion source prototypes is radiative recombination. Due to the low electron density, three body recombination plays no role. Three sets of input parameters are available for this process: rate coefficients taken from the CR model by Sawada [11] (implemented as standard to Yacora), more recent rate coefficients from the 2003 data compilation by Janev [12] and cross sections calculated by the Bethe approximation. To enable a comparison of these three data sets, the Bethe cross sections were averaged using a Maxwell EEDF to obtain rate coefficients.

The three available rate coefficients agree very well for all principal quantum numbers: while the Sawada and Janev data are virtually identical, the Bethe cross sections show small deviations (below 15 % for n=2 and decreasing with the principal quantum number) in the complete electron temperature range for low principal quantum numbers (n<5). This indicates that no exchange of the rate coefficients used by Yacora is necessary. The availability of the Bethe cross sections opens the additional possibility to perform Yacora calculations in the recombining plasma regime for non-Maxwell EEDF. Figure 147 shows the three available rate coefficients for the state with the principal quantum number n=5 (which is the upper state of the H_γ transition).

For dissociative recombination of H_2^+ the most recent available rate coefficients from [10] have been implemented in Yacora some time ago (where it replaced data taken from the Sawada CR model). These rate coefficients resolve both the different possible educts (vibrational excitation of H_2^+) and products (electronic excitation of H). To calculate the total dissociative recombination rate coefficient, a vibrational tem-
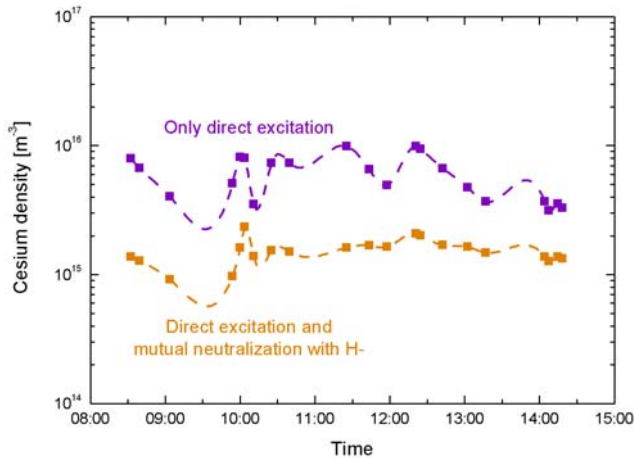
Figure 149: Progress of the cesium density during one day of operation in BATMAN. Purple symbols: evaluated by applying the simple Corona model to the Cs852 line emissivity. Orange symbols: Corona model extended by mutual neutralization of Cs^+ with H^-.

perature of T_{vib}=7000 K in the molecular ground state (measured in the IPP negative hydrogen ion sources by OES) was used to determine the vibrational distribution in H_2^+ (by applying the Franck Condon principle).

Now it was checked how strong the dependence of the total dissociative recombination rate coefficients on the vibrational temperature of H_2 is. A strong dependence would introduce another relevant parameter and thus complicate the evaluation of OES results. Rate coefficients for dissociative recombination of H_2^+ were calculated for the three vibrational temperatures T_{vib}=0 K, 7000 K and 10000 K. The results of these calculations (again for principal quantum number n=5 in the atom) are shown in figure 148: for low electron temperature (T_e<1 eV) the rate coefficient used by Yacora (T_{vib}=7000 K) deviates by a factor lower than two from the one for T_{vib}=0 K. For higher electron as well as vibrational temperatures the deviations are significantly smaller; the rate coefficients for T_{vib}=7000 K and T_{vib}=10000 K are almost perfectly lying on top of one another. This finding affirms that the implementation of the dissociative recombination rate coefficients in Yacora is correct and small deviations of the vibrational temperature from T_{vib}=7000 K needs not to be considered explicitly by the model.

Another important aspect in the diagnostics of the ionizing and recombining parts of the plasma is the cesium emission. The intensity of emission lines of cesium directly depends on the electron density and temperature but also on the cesium density. The cesium density, on the other hand, is correlated with the cesium flux from and onto the walls of the ion source. Thus, measuring cesium emission is an important tool for controlling the conditioning phase of the ion source prototypes. Different spectrometers and diodes, which mainly detect the intensity of the neutral cesium line at 852 nm, are attached to the IPP ion source prototypes. Up to now, for the interpretation of the line emissivity a simple Corona model is used, which balances excitation by electron collision with spontaneous emission. Such a model is valid for ionizing plasmas only. However, cesium radiation is detected also in plasma volumes which are known to be recombining. This finding suggests the existence of alternative excitation channels.

Final goal of the ongoing work is to create a model for population densities of the excited states of cesium in ionizing and recombining plasmas as well as in intermediate regions. As first step theoretical and experimental investigations on alternative excitation channels were performed. One candidate for such channels is the mutual neutralization of positive cesium ions with negative hydrogen ions. The neutral cesium atoms generated by this process are mainly excited to the level 6p which is the upper level of the resonant transition at 852 nm (6p→6s). The simple Corona model was extended by including the mutual neutralization process. Figure 149 shows the progress of the cesium density during one day of operation at BATMAN cal-
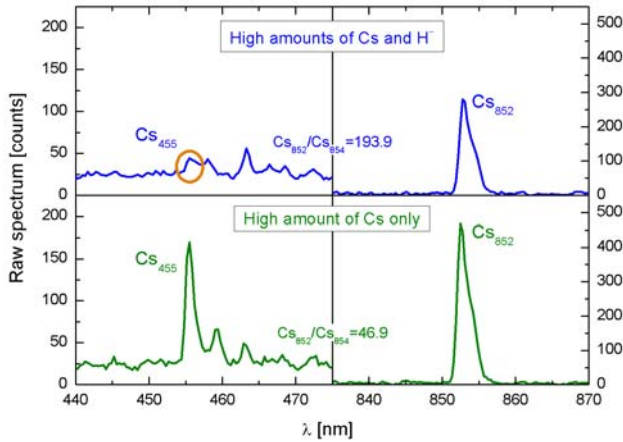
Figure 150: Emission lines of cesium measured in different plasma regimes. The large observed differences in the line ratio Cs852/Cs455 suggest the existence of alternative excitation channels besides the direct excitation from the ground state 6s.

culated using the plain and the extended Corona model. For the extended Corona model the negative hydrogen density as well as the ionization degree of cesium has to be known as input parameters and have been estimated based on previous results of spectroscopy and cavity ring-down measurements, respectively. The cesium densities calculated with the extended Corona model are significantly lower than the results of the original model and are in much better agreement with other diagnostics (laser absorption).

Additionally, spectroscopic measurements have been performed to investigate the influence of negative hydrogen ions on the cesium radiation. Figure 150 shows two spectra taken with the survey spectrometers at the BATMAN test facility. For both spectra lines of sight parallel to the plasma grid, in 0.7 cm distance and thus well inside the boundary layer, were used. The upper spectrum was taken in a well conditioned source with a high amount of cesium in the source volume. Additionally, a high current of negative ion current was extracted (I_{ex}=220 A/m^2). Thus, a high negative ion density is present in the boundary layer. While the cesium line at 852 nm can be seen, the emission line at 455 nm is almost beyond the noise level. The calibrated line ratio is 193.9. In contrast, the spectrum shown in the lower part of figure 150 has been taken in a source with high cesium amount but simultaneously a relatively low amount of negative hydrogen ions (I_{ex}=107 A/m^2). Reason for the low level of negative ions was a water leak (which was discovered at the end of the next operational day) which poisoned the cesium layer on the inner surfaces of the ion source. The ratio of the cesium emission line at 852 nm to the line at 455 nm is much smaller than in the first spectrum. The calibrated line ratio is 46.9, which is close to the theoretical value 54.5 for direct excitation by electron collision from the ground state. The external source parameters for both spectra are identical: 0.55 Pa filling pressure and 60 kW RF power. The observed difference of the line ratios emphasize the assumption that excitation channels like mutual neutralization of positive cesium ions with negative hydrogen ions may play an important role in the ion sources.

The theoretical investigations based on the extended Corona model as well as the experimental investigations based on spectroscopic results point up the necessity of the development of a Collisional Radiative model for cesium. This development will be started as a next step. Since the input data for such a model available in literature is extremely scarce, it is planned to calculate non-existing rate coefficient data by simple approximations like the Gyrzinski method.

8 References

1. M. Singh, B. de Esch, ISTF Design Review Meeting, Padua, October 2008

2. www.quickfield.com

3. R. Gutser et al., Transport of Negative hydrogen and deuterium Ions in RF-driven Ion Sources, Plasma Phys. Control. Fusion 51 (2009) 045005

4. P. Franzen et al., Performance of Multi-Aperture Grid Extraction Systems for an ITER-relevant RF Driven Negative Hydrogen Ion Source, submitted to Nuclear Fusion

5. U. Fantz et al., Plasma Phys. and Control. Fusion 49 (2007) B563

6. D. Wünderlich, R. Gutser and U. Fantz, Plasma Sources Sci. Technol. 18, 2009, 045031

7. T. Tabata and T. Shirai, *Atomic Data and Nuclear Data Tables, 76, 1 (2000)*

8. G. Fubiani, H. P. L. de Esch, A. Simonin and R. Hemsworth, *Phys. rev. ST AB, 11, 014202 (2008)*

9. U. Fantz et al., Rev. Sci. Instrum. 81, 02B102 (2010)

10. D. Wünderlich, S. Dietrich and U. Fantz, Journal of Quant. Spec. Rad. Transf. 110, 2009. 62

11. K. Sawada, T. Fujimoto, J. Appl. Phys. 78, 1995, 2913

12. R.K. Janev, D. Reiter, U. Samm, Report JÜL-4105, Forschungszentrum Jülich, 2003

9   Appendix:

9.1   Detailed Schedule
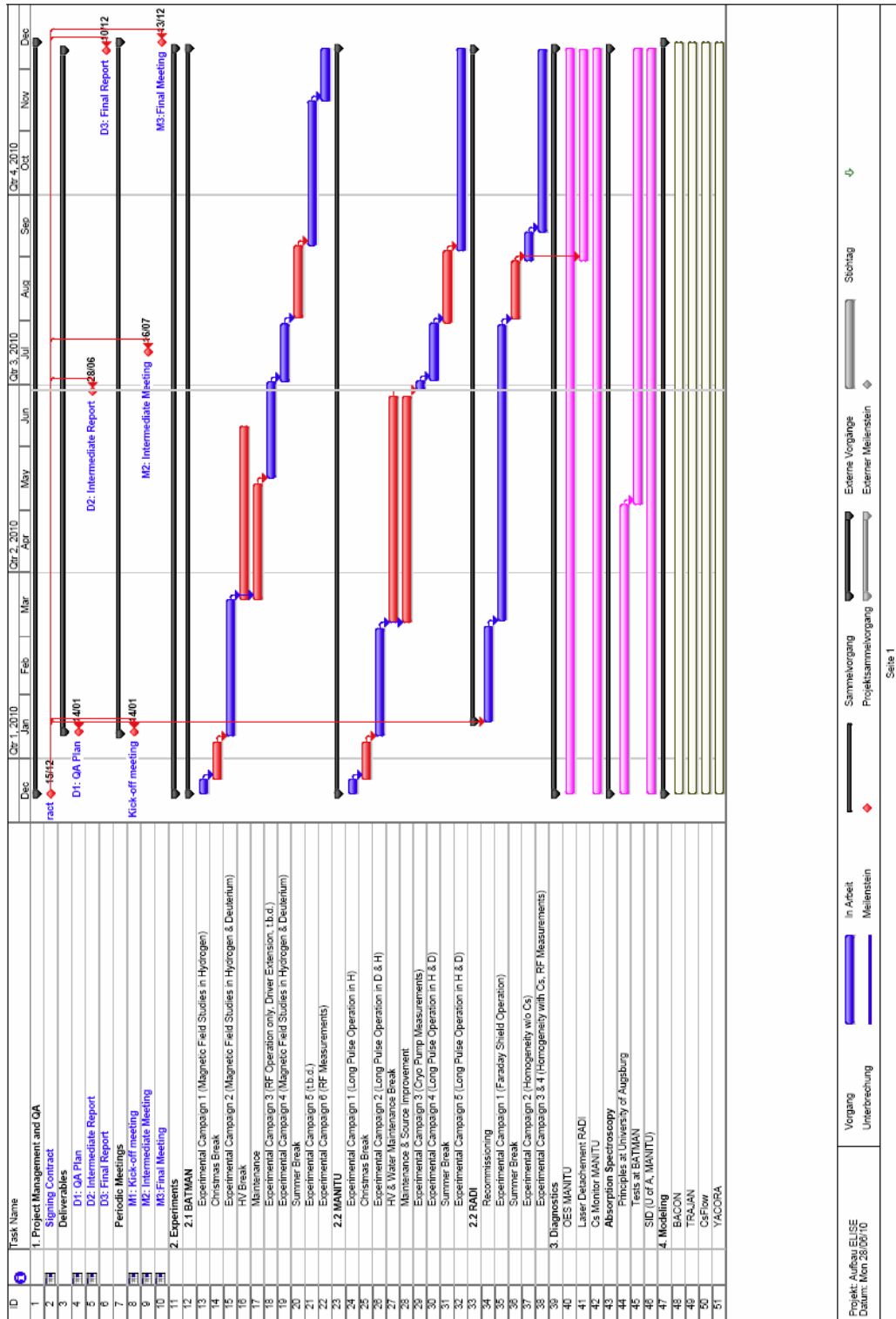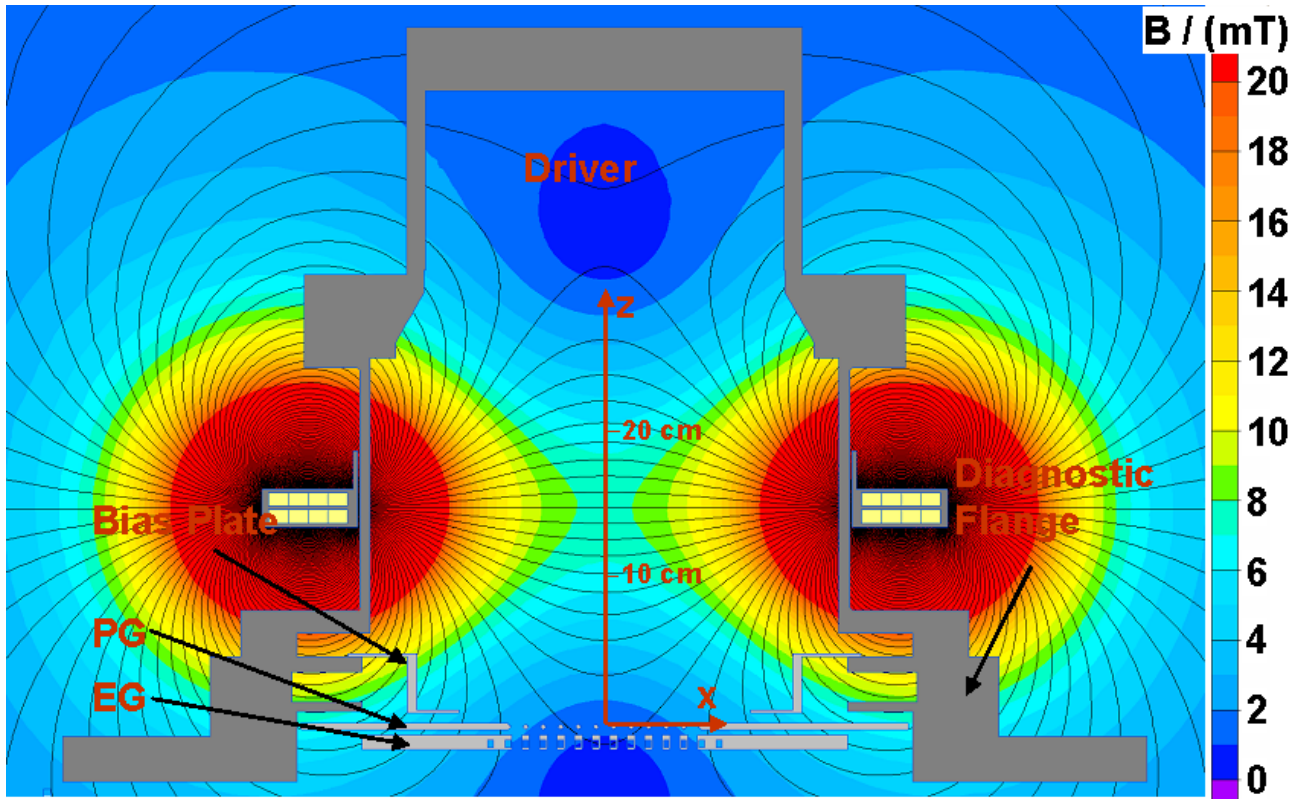
9.2 2D-Maps of Magnetic Fields
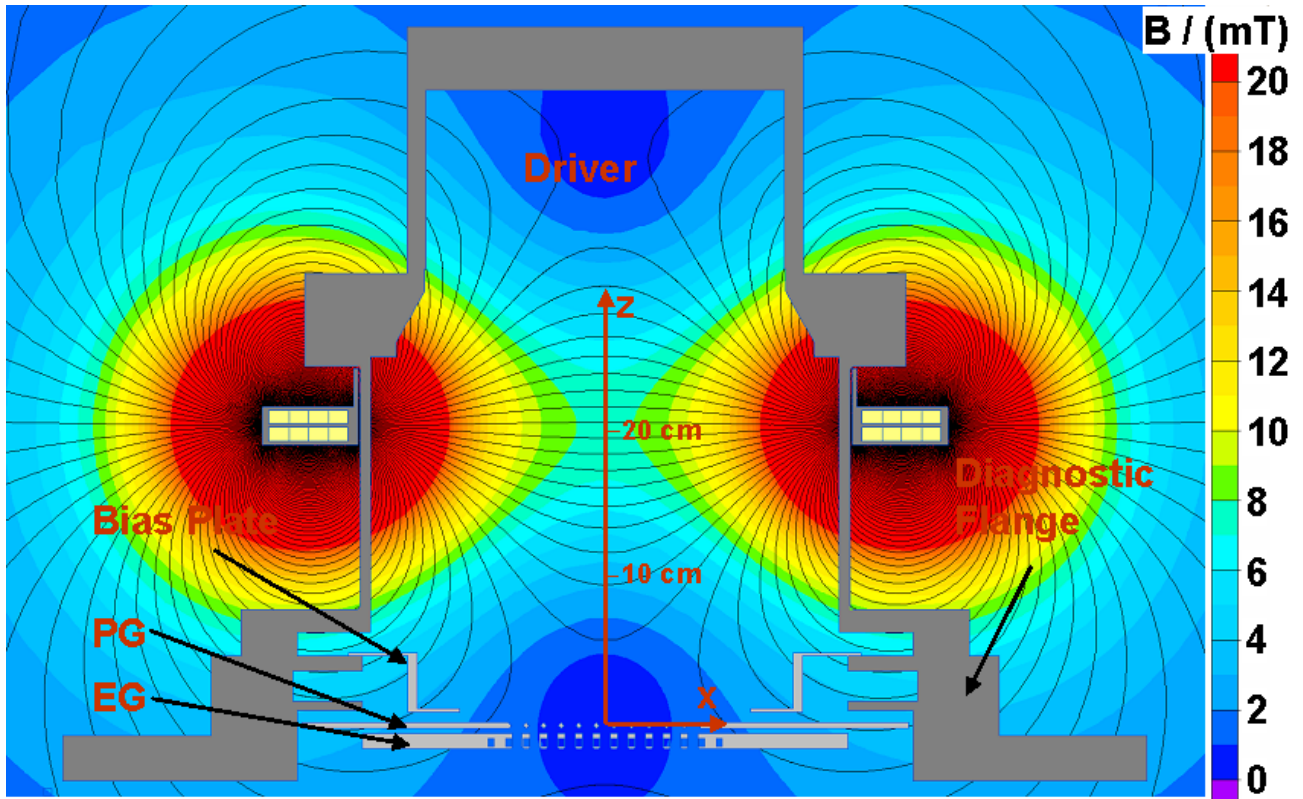
9.2.1 Standard Case
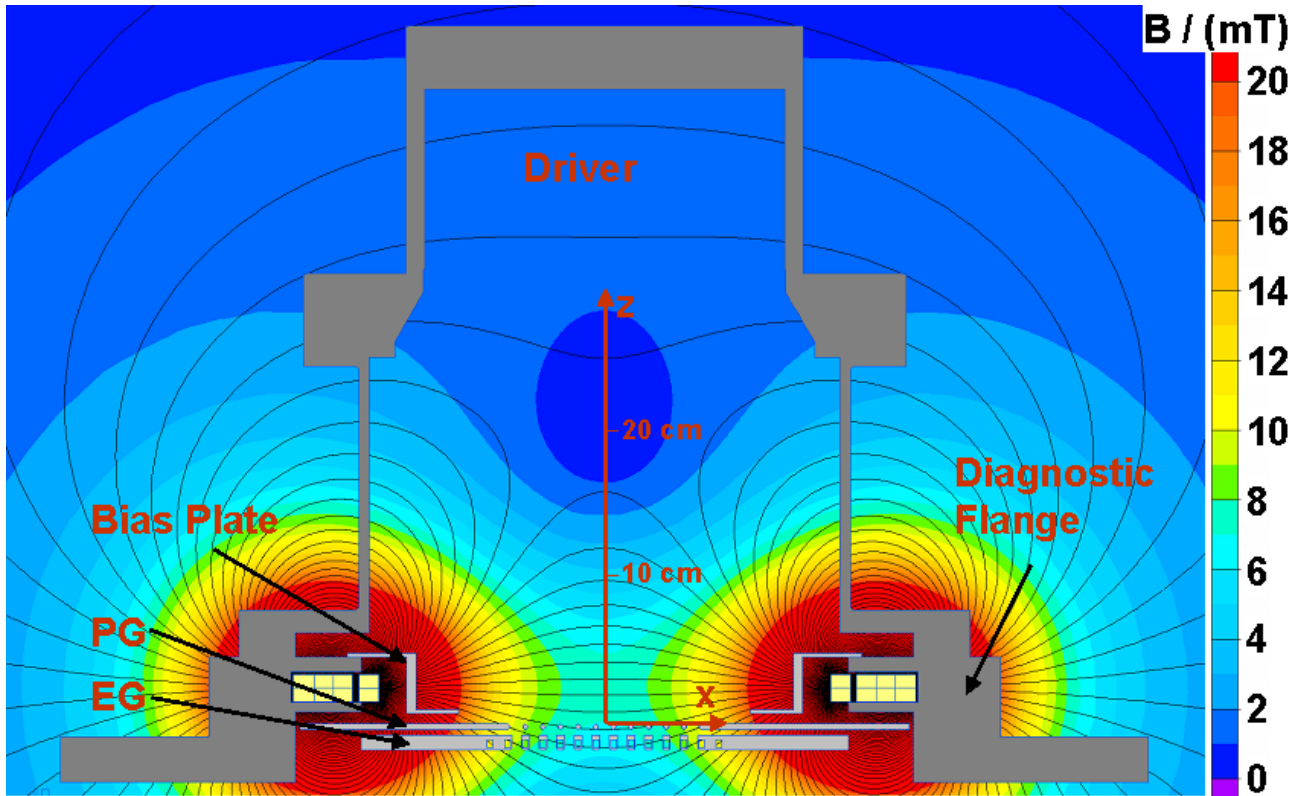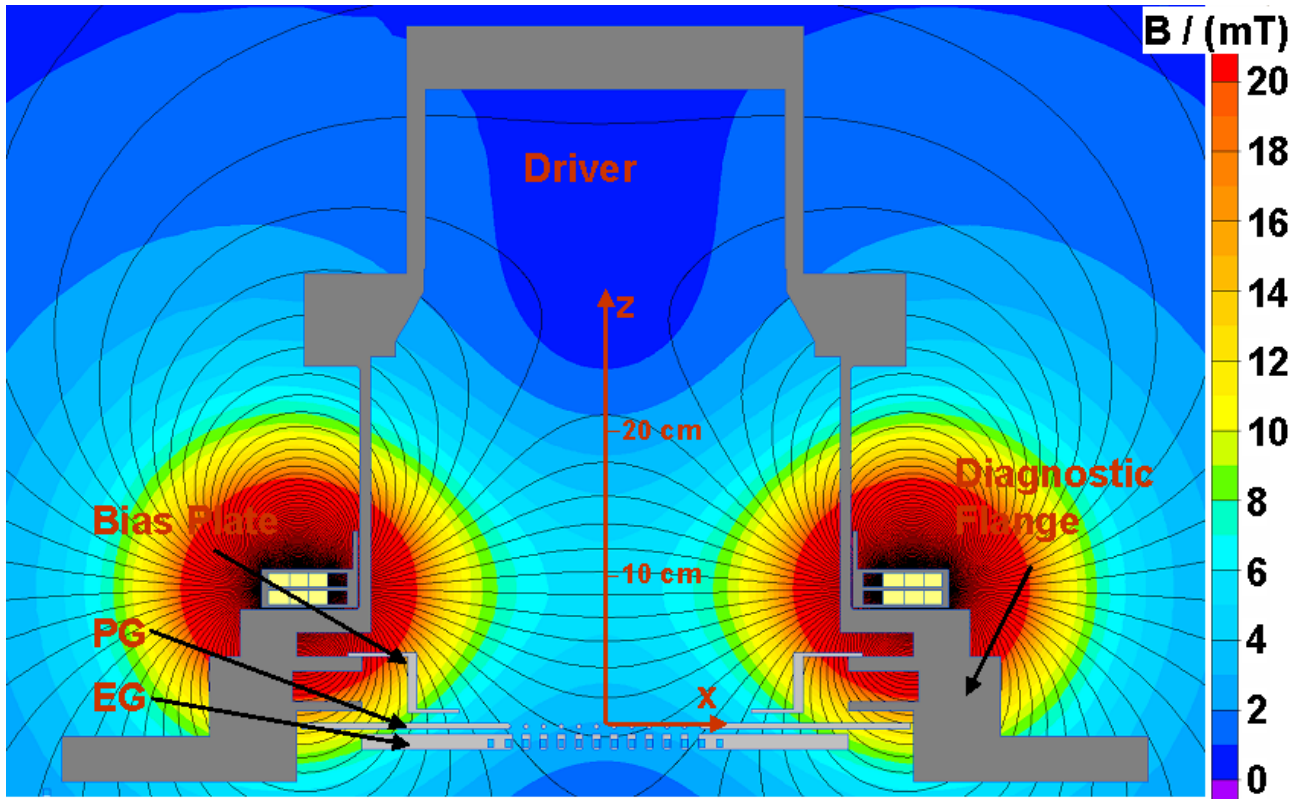
9.2.2 "BMAX, z=9" Case
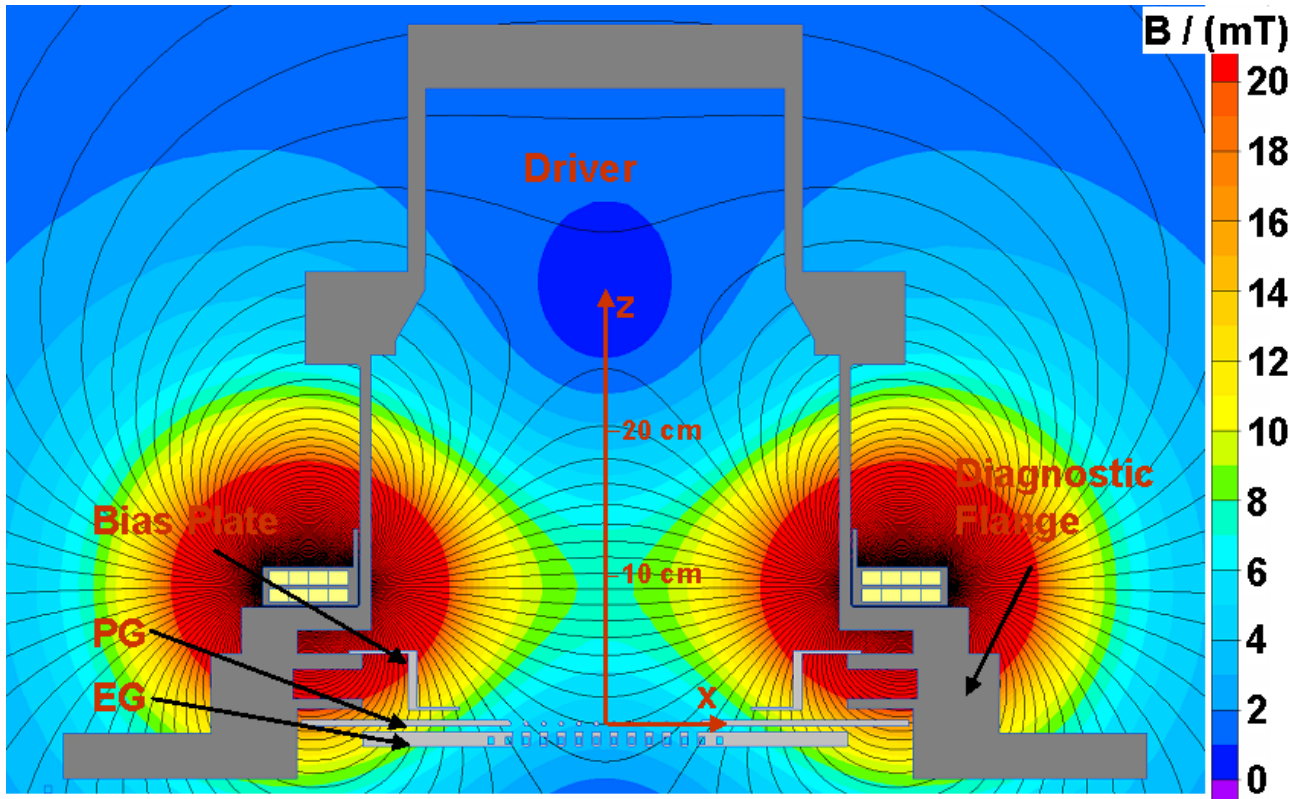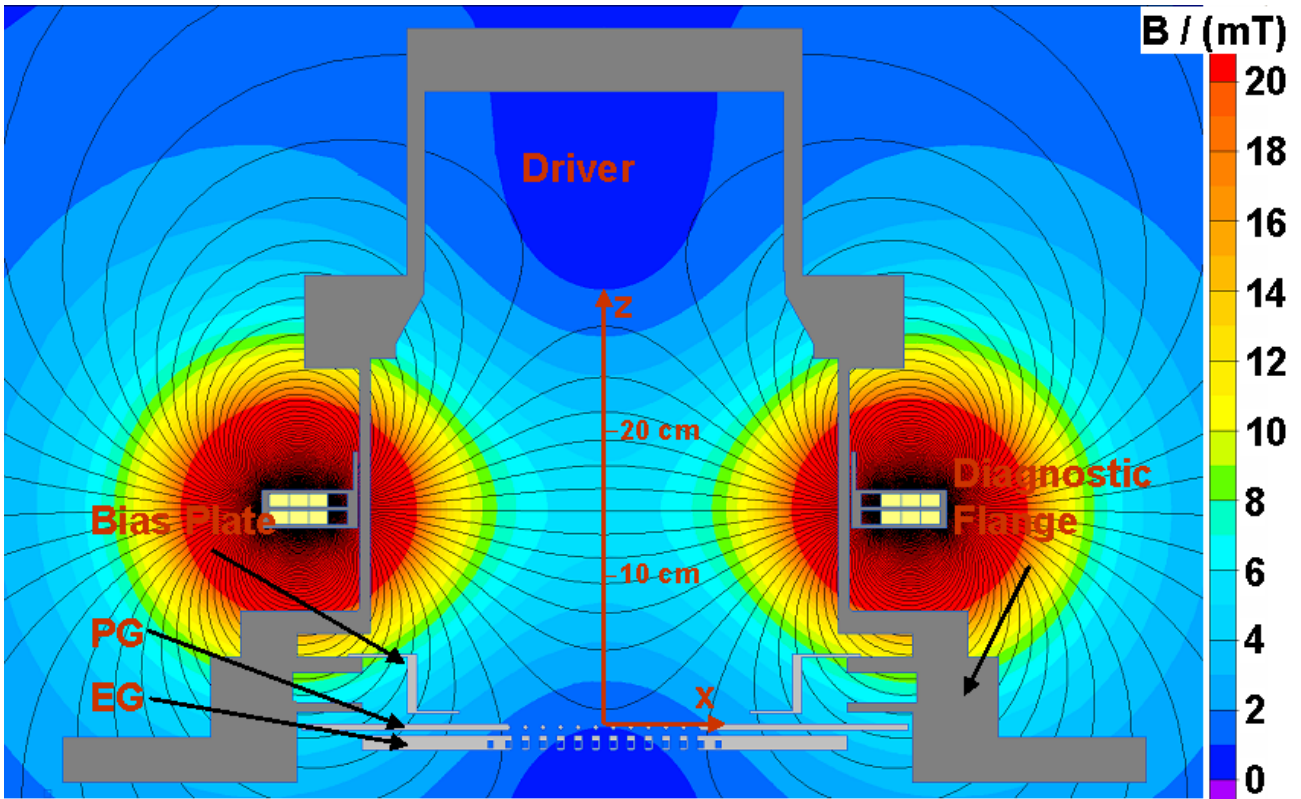
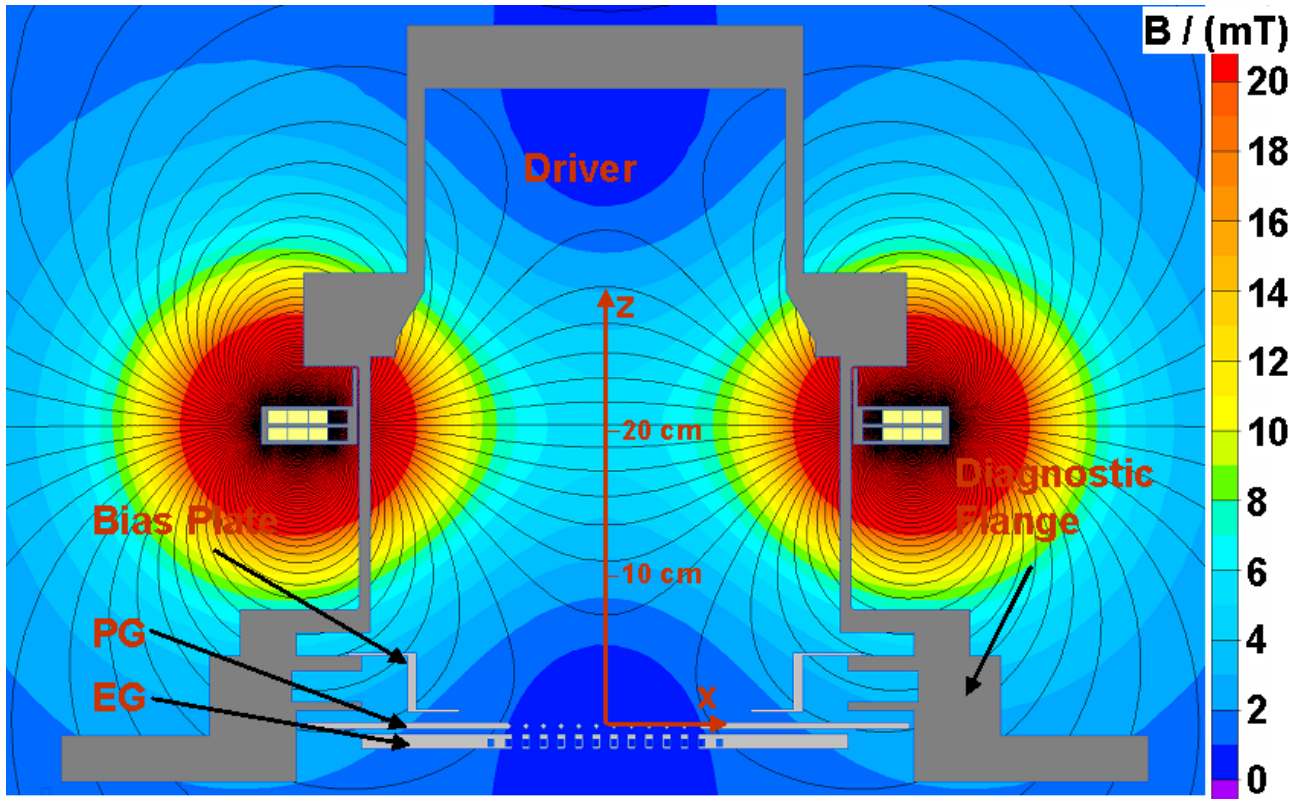### 9.2.3 "BMAX, z=14" Case

9.2.4 "BMAX, z=19" Case
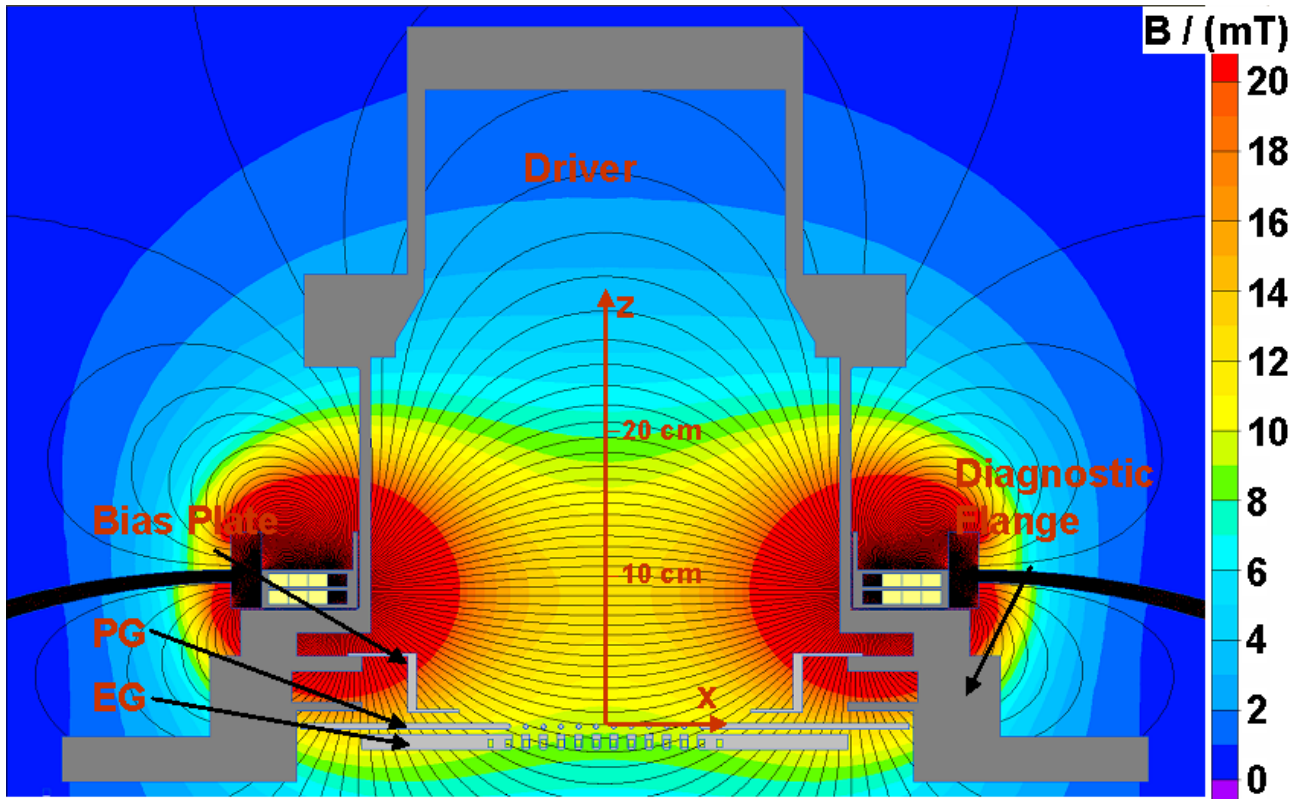
9.2.5 "BDL, z=9" Case
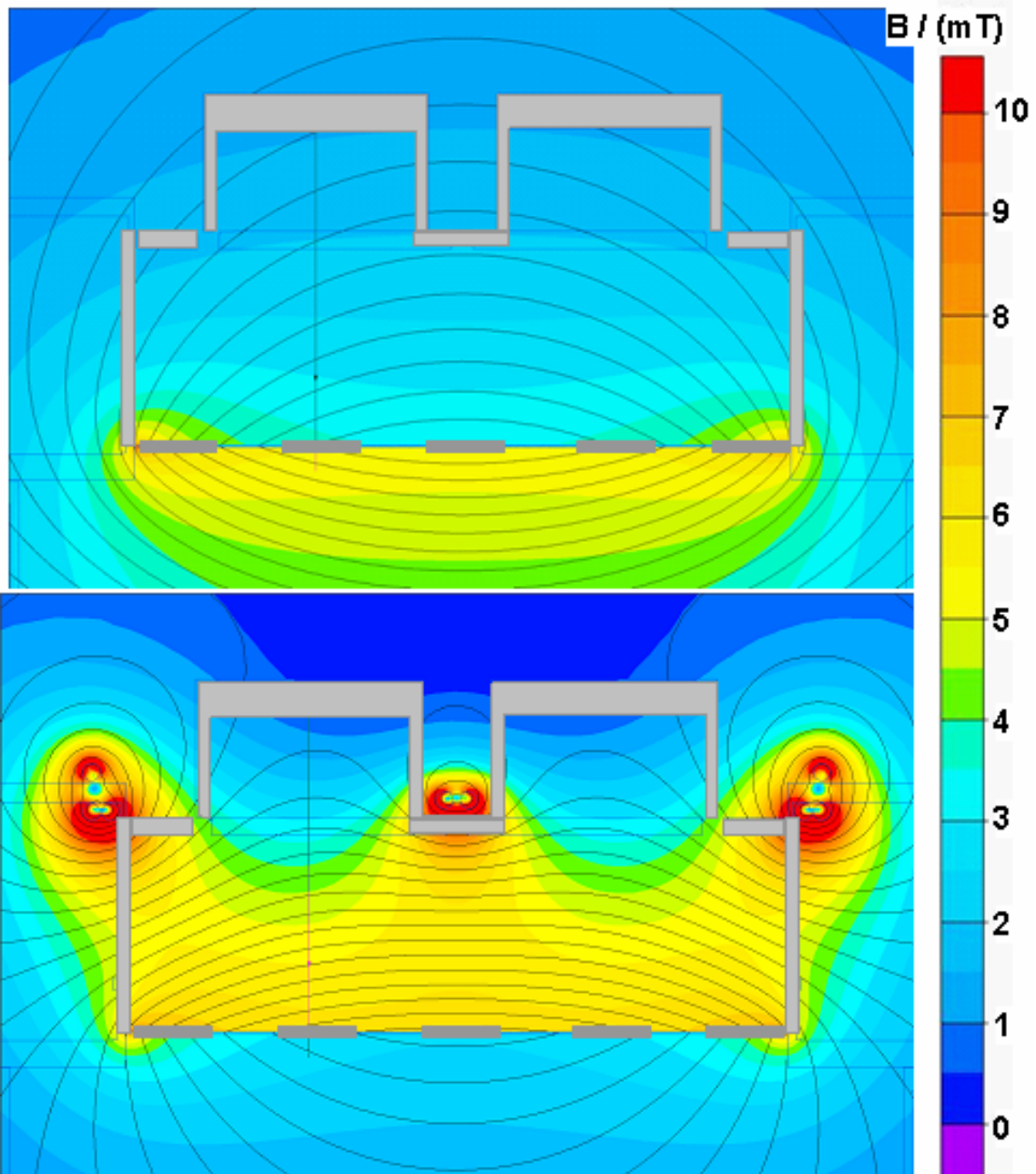
9.2.6 "BDL, z=14" Case

9.2.7 "BDL, z=19" Case

9.2.8 "BDL, z=9, closed Yoke" Case

9.2.9 Comparison RADI Fields w/o and with PG return conductors near driver

Top: RADI source with the PG return conductors far away downstream

Bottom: RADI source with the PG return conductors near the drivers